To the Graduate Council:

I am submitting herewith a dissertation written by Khaled S. Mriziq entitled "A High Shear-Rate Optical Rheometer for Complex Fluids." I have examined the final electronic copy of this dissertation for form and content and recommend that it be accepted in partial fulfillment of the requirements for the degree of Doctor of Philosophy, with a major in Physics.

Robert N. Compton, Major Professor

_____

We have read this dissertation
and recommend its acceptance:

Hank D. Cochran

_____

Thomas Callcott

_____

David J. Pegg

_____

Mark D. Dadmun

_____

Accepted for the Council:

Anne Mayhew

_____

Vice Provost and Dean of Graduate Studies

(Original signatures are on file with official student records.)

A HIGH SHEAR-RATE OPTICAL RHEOMETER FOR COMPLEX FLUIDS

A Dissertation
Presented for the
Doctor of Philosophy Degree
The University of Tennessee, Knoxville

Khaled Suleiman M. Mriziq
December 2003

Copyright © 2003 by Khaled S. M. Mriziq
All rights reserved

DEDICATION

This dissertation is dedicated to my parents, Suleiman M. Mriziq and Thurya E. Shurayqi for their love and support. The special dedication goes to my wife, Mona (Rabiah) Al-Omari for her support, encouragement, love giving me the strength to finish this research, and for my two lovely boys, Amer and Anmar.

"The bond that links your true family is not the one of blood,

but of respect and joy in each other's life" Richard Bach

Thank you Mona

ACKNOWLEDGEMENTS

First, I would like to express my deep appreciation to my major advisor Hank Cochran for his guidance, advice, help, freedom, ideal research environment, and endless support throughout the research. He has truly played an important role in each successful step during this research. I also owe many thanks to my Physics advisor Bob Compton for helpful guidance throughout my research. I would like to thank Mark Dadmun for many helpful discussions regarding my research as well as the members of my committee, Tom Callcott and David Pegg. I'm also very thankful to the advice and help I received from Jay Jellison, from him I had the opportunity to learn. Special thanks to James Dai.

During my research work, I had the opportunity to interact scientifically and socially with many people at the University of Tennessee and Oak Ridge National Laboratory. I have specially enjoyed the memories with my friend and officemate Carrie Gao. And to all people I have not mentioned their names, thank you. Last but not least, I thank every one who supported me during the difficult times I have been through during my research.

I would like to express my appreciation to the support from the US Department of Energy for their support to this research through Oak Ridge National Laboratory.

Finally, special thanks to my family, the completion of this work could not have been accomplished without the support of my parents and my wife Mona.

ABSTRACT

A parallel-plate optical rheometer in a magnetic-disc drive configuration has been designed and constructed of optically transparent materials and operating with a very small gap to obtain rheological and structural measurements at very high shear rates.

The friction force at the disk-slider interface has been measured as a function of sliding speed while the film thickness was monitored in situ using a capacitance technique. The shear rate is calculated from the film thickness and the sliding speed. A thin film can be applied on the disk, which allows very high-shear-rate measurements at low sliding speeds with negligible viscous heating.

Both disk and slider have been made of optically transparent material to allow optical measurements simultaneously with the rheological measurements. In the present mode the apparatus is set up for simultaneous rheometery and birefringence measurements on a thin film of polymer lubricant. Rheology and birefringence measurements were made on a perfluoropolyether lubricant over a range of strain rate from 10^3 s^{-1} to greater than 10^6 s^{-1} with different film thicknesses.

The rheological results of PFPE Fomblin® YR under steady-state shear conditions reveal a shear-thinning transition at shear rate about $10^4 s^{-1}$. The rheological results were in agreement with the flow-induced birefringence. The birefringence measurements where first time that results have been carried out at high shear rate.

CONTENTS

Chapter1 Introduction……1

1.1 The science of rheology……1

1.2 Fascinating polymer liquids……...1

1.2.1 Shear thinning and shear thickening……..……...2

1.2.2 Yield stress……..…….2

1.2.3 Rod-climbing…….……...4

1.2.4 Die swell…….…….....4

1.3 Rheometry……..…7

1.4 Motivation……..…7

Chapter 2 Theoretical background……11

2.1 Equations of fluid dynamics……..……11

2.1.1 Conservation of mass: Equation of continuity……11

2.1.2 Conservation of Momentum: Equation of motion……..13

2.1.3 Newtonian fluid……...……14

2.1.4 Steady simple shear flow……..……...16

2.1.5 Material functions in steady shear……..…….21

2.2 Optical phenomena……..……..21

2.2.1 Polarized light……..……22

2.2.2 The Jones Vectors and Stokes Vectors……..……..…23

2.2.3 Mueller Matrices and Jones Matrices……..……25

2.2.4 Anisotropic Retardation: Birefringence……..…….28

2.3 Experimental measurements……..…….…….....…..30

Chapter 3 Optical rheometer design concepts…………...…...33

.

3.1 Introduction…….……..33

3.2 Parallel plate rheometry……...…….37

3.2.1 Theory of the parallel-plate rotational rheometer……...…....37

3.2.2 Viscous heating……..……...……40

3.3 Capacitance……...……....45

3.4 Optical rheometry……...…….….47

3.4.1 Birefringence measurement ……..……...…….….47

3.4.2 Polarization modulation Technique……...……..…48

3.4.3 Photoelastic modulator (PEM) ……...……..48

3.4.4 Stokes vector description of polarimetry design……..…. ...53

3.4.5 Intensity for PSG PSA configuration……...…… .56

3.5 Concluding remarks……...…… 59

Chapter 4 Experimental setup……...…… …..60

4.1 Literature review……...…… ….60

4.1.1 High-shear-rate rheometry……...…… 60

4.1.2 Measurement of polymer birefringence……...…… …61

4.2 Rheometer……...……. ..62

4.2.1 Shearing disk...……. …62

4.2.2 Slider...…….…… …64

4.2.3 Slider arm...……..……..…64

4.2.4 Supporting system...……...……...64

4.3 Drive system...……66

4.4 Detection system...……66

4.4.1 Force measurements……...…….69

4.4.2 Rotational speed measurement……...…….69

4.4.3 Capacitance measurement……..69

4.5 Birefringence……..……70

4.5.1 Laser source……..……..…70

4.5.2 Linear polarizer……..……....70

4.5.3 Photoelastic modulator (PEM) ……..……..72

4.5.4 Analyzing polarizer……..……72

4.5.5 Stokes vector of the sample……..……....72

4.6 Electronics and control systems……..……...73

4.6.1 Rheometer control system……..……73

4.6.2 Birefringence control system: Waveform analysis……75

4.7 Test samples……...77

4.8 Sample preparation…….82

Chapter 5 Results and discussion…….83

5.1 Calibration……...83

5.1.1 Strain gauges……..…83

5.1.2 Speed calibration……....83

5.1.3 Capacitance calibration……..83

5.1.4 Birefringence calibration……....86

5.1.4.1 Determination of θ_b…….……..86

5.1.4.2 Determination of δ_o…….……88

5.1.4.3 Determination of A…….…....88

5.1.4.4 Determination of the normalization coefficients…..……88

5.1.4.5 Birefringence of quarter wave plate (QWP) ……..…....91

5.1.4.6 Windows effect…….…….....91

5.2 Rheometer results…….……...…….....93

5.2.1 Test measurements……..……...…….....93

5.2.1.1 Force measurements…….96

5.2.1.2 Capacitance measurements…….....96

5.2.1.3 Normal force measurements……..…….....96

5.2.1.4 Shear stress vs. capacitance……..…….....96

5.2.1.5 Viscosity measurements……...……101

5.2.1.6 Viscous heating…….……...…….101

5.2.2 Rheology of Fomblin YR…….…….……105

5.2.2.1 Shear stress vs. shear rate…….105

5.2.2.2 Viscosity of Fomblin YR……..108

5.2.2.3 Rheology of Fomblin YR: Discussion……..108

5.3 Birefringence of Fomblin YR…….……110

Chapter 6 Conclusions and future work……..…….……..116

6.1 Conclusions…….……..……..116

6.2 Future work…….……..…..117

Bibliography…….……120

Appendices…….……....125

Vita…….…….136

LIST OF TABLES

Table 2.1 Jones and Stokes vectors for various forms of polarized light……..26

Table 3.1 Typical shear rates for familiar materials processes……..34

Table 3.2 Common shear flow geometries…….35

Table 4.1. Properties of Fomblin YR…….....80

LIST OF FIGURES

Figure 1.1 Tube flow behavior: Newtonian behavior is shown on the left "N", the polymer behavior is shown on the right "P". The polymer flows out faster than the Newtonian fluid……3

Figure 1.2 Rod climbing experiment. The Newtonian "N" fluid shows a vortex; the polymer "P" solution climbs up the rod……..…….5

Figure 1.3 Shear stress and normal stresses…….5

Figure 1.4 Die swell: A stream of Newtonian fluid "N" shows no diameter increase upon flowing out of a tube, a polymeric "P" fluid shows an increase in diameter flowing out of the tube……...……..6

Figure 1.5 Viscosity behaviors for Newtonian and non-Newtonian fluids……..8

Figure 1.6 Viscosity versus shear rates for non-Newtonian fluid, experimental techniques are limited to moderate shear rate while realistic molecular simulations reach very high shear rate……...……9

Figure 2.1 Mass and momentum on control volume V……...12

Figure 2.2 Geometry for Newton's experiment……..15

Figure 2.3 Steady state shear flow……..17

Figure 2.4 Shear planes sliding over each other during steady state flow……..18

Figure 2.5 Velocity profile with respect to symmetry axis…….20

Figure 2.6 Transformation of light by polarizing optical element……..27

Figure 2.7 Anisotropic polarization due to chain orientation through applying stress……..31

Figure 3.1 Schematic of parallel-plate rheometer……...38

Figure 3.2 Hard disk drive system……..41

Figure 3.3 Schematic of flow between horizontal plates……43

Figure 3.4 Non-parallel and parallel plate……..…… 46

Figure 3.5 Axes of stresses and refractive indices in simple shear…….49

Figure 3.6 Photoelastic modulation (PEM)……..……..50

Figure 3.7 Polarization modulation technique……52

Figure 3.8 Polarimetry experiment design……..57

Figure 4.1 The disk and slider……63

Figure 4.2 Strain gauges structure and strain gauges arms…….....65

Figure 4.3 Schematic of disk-slider assembly……67

Figure 4.4 Drive and support system…….. 68

Figure 4.5 Optical system elements with orientation…….……71

Figure 4.6 Data control and collection for rheometer……...…..74

Figure 4.7 Data control and collection for birefringence……....78

Figure 4.8 Schematic illustration of the whole apparatus……..79

Figure 5.1 Output voltages of strain gauges versus applied force……..84

Figure 5.2 Speed calibrations……..... 85

Figure 5.3 Capacitance calibration curve……....87

Figure 5.4 The Bessel function calibration curve for the PEM……...89

Figure 5.5 Normalization of the output signals……..……90

Figure 5.6 Quarter wave plate retardation……...92

Figure 5.7 Soleil-Babinet compensator……...94

Figure 5.8 Output of channel 1 without and with Soleil-Babinet compensator……..95

Figure 5.9 Shear stress for one revolution, the film is Fomblin YR with thickness of 485 nm and sliding speed 50 mm/……97

Figure 5.10 Film thickness calculated from the capacitance…….98

Figure 5.11 Capacitance and film thickness for film of 485 nm thickness at sliding speed 50 mm/s……..99

Figure 5.12 Normal load output voltages for three rotations……..100

Figure 5.13 Shear stress and capacitance for a disk lubricated with 485 nm Fomblin YR and sliding speed 50 mm/s…….. 102

Figure 5.14 Viscosity of Fomblin YR film over one revolution……..103

Figure 5.15 Viscosity of Fomblin YR for different films……....104

Figure 5.16 Shear stress versus shear rate for different Fomblin YR films…….....106

Figure 5.17 Shear stress versus shear rate for different Fomblin YR films…….....107

Figure 5.18 Shear viscosity for different Fomblin YR films……...109

Figure 5.19 Shear rate dependence of the viscosity and the predicted shear thinning behavior of Fomblin YR (Data of references 21 and 24 as analyzed in reference 68)……111

Figure 5.20 Birefringence data with background for different Fomblin YR films….113

Figure 5.21 Birefringence data for Fomblin YR with background subtracted……...114

Figure 5.22 Shear viscosity and flow induced birefringence at high shear rate…....115

Figure B.1 Birefringence data for different Fomblin YR with shear rate……131

Figure B.2 Best fit line for birefringence data at moderate shear rates……133

Figure B.3 Best fit line for birefringence data at high shear rates……134

Figure B.4 Birefringence data after background reduction……135

CHAPTER 1
INTRODUCTION

1.1 The science of rheology

The word rheology comes from a Greek word $\rho\varepsilon\iota\nu$, which means to flow. The first time that word was used to describe flow was by Bingham who was fascinated by the unusual flow behavior of complex fluids such as polymeric liquids, biological systems, and other compounds. Rheology is the study of deformation of matter under the influence of imposed stress. Fluids respond to stress by flow; the flow of a fluid includes how the mass, momentum, and energy change with position and time.

Fluids respond to stress in different ways. Newton described the response in a simple relation between the rate of deformation and applied stress with a constant of proportionality called *viscosity*. Fluids that follow such a simple rule are called "Newtonian Fluids"; water is an example of such a fluid. However, the word rheology was invented to describe a different response, the response of fluids which do not obey such a simple relation between applied stress and rate of deformation and exhibit a non-linear response. Such fluids are described as "Non-Newtonian Fluids". Most synthetic polymeric materials exhibit some degree of non-Newtonian behavior. Between the extremes of elastic and fluid response lies a spectrum of combination of these basic types of material behavior. Plastic response is one wherein a material deforms like an elastic solid so long as the applied stress is below some limit called the yield stress. When the applied stress exceeds the yield stress, the material behaves as a fluid. Viscoelastic fluid resists deformation but at the same time resists a time rate of change of deformation. Thus it exhibits some combination of elastic and fluid response.

1.2 Fascinating polymer liquids

Newton wrote a simple relation defining the viscosity of a fluid, which measures the internal resistance to flow, as a proportionality constant between the shear stress and the velocity gradient. Newton's equation applies well in describing gases and liquids made of small molecules. However, Newton's equation fails to describe the flow of

liquid containing polymeric materials, which consists of large molecules. This section deals with some fascinating experiments [1,2] which describe such unusual behavior along with the expected behavior of Newtonian liquids when they are subject to flow.

1.2.1 Shear thinning and shear thickening

Figure 1.1 describes a simple experiment in which two fluids, Newtonian and polymeric, with the same viscosity first flow from tubes subject to gravity. The flow of the polymeric material out of the tube is faster than the Newtonian fluid. Classical hydrodynamics predicts that the volumetric flow, for a given pressure drop, is inversely proportional to the viscosity. Thus, the faster flow of the polymeric material can be related to a decrease in the viscosity with higher shear rate. The decrease in the viscosity with increasing the shear rate is referred to *shear thinning*. The fluid is called pseudoplastic.

A few liquids behave in an opposite way, they exhibit an increase in viscosity with increase in shear rate, and this behavior is referred to as *shear thickening*.

1.2.2 Yield stress

Some polymeric fluids show a complex rheological effect when subject to stress, these fluids will not flow unless that stress exceeds a certain critical value that is referred to as *yield stress*. Newtonian fluids always flow when subject to stress. A good example of this effect is something that can be easily observed in the kitchen. For example, honey is a Newtonian fluid [3], which flows under any stress. When a flat surface of honey is disturbed, the fluid surface will return to its original shape under the effect of the small force of gravity.

Mayonnaise, on the other hand, is a non-Newtonian fluid; when its flat surface is disturbed, it does not return to its original shape under gravity. Mayonnaise is a yield stress fluid; it will flow easily when a high stress is imposed, higher than that of gravity.

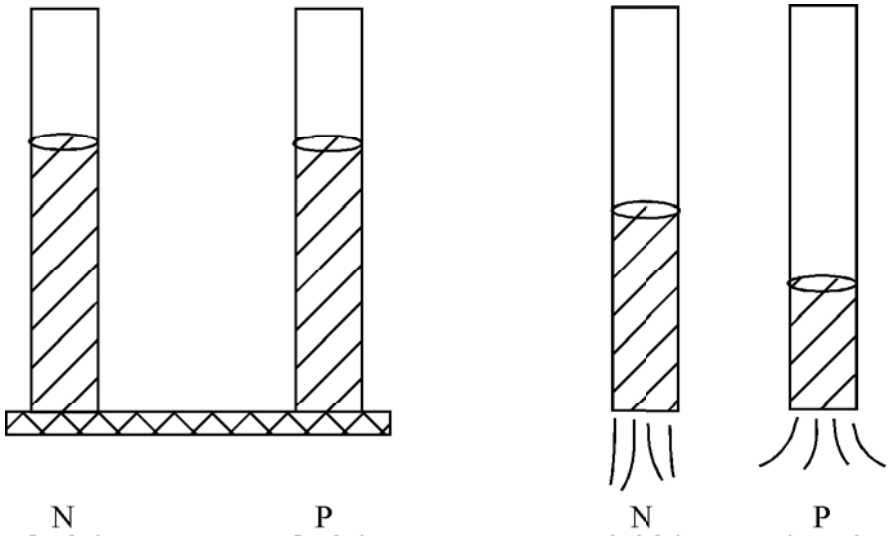


Figure 1.1 Tube flow behavior: Newtonian behavior is shown on the left “N”, the polymer behavior is shown on the right “P”. The polymer flows out faster than the Newtonian fluid.

1.2.3 Rod-climbing

In a simple experiment demonstrated in figure 1.2, a rod rotating at high speeds is inserted in beakers, one containing Newtonian fluid and the other polymeric fluid [1]. The Newtonian fluid near the rod is pushed outward by the centrifuge forces, and the surface near the rod is characterized by a dip in the liquid in that area.

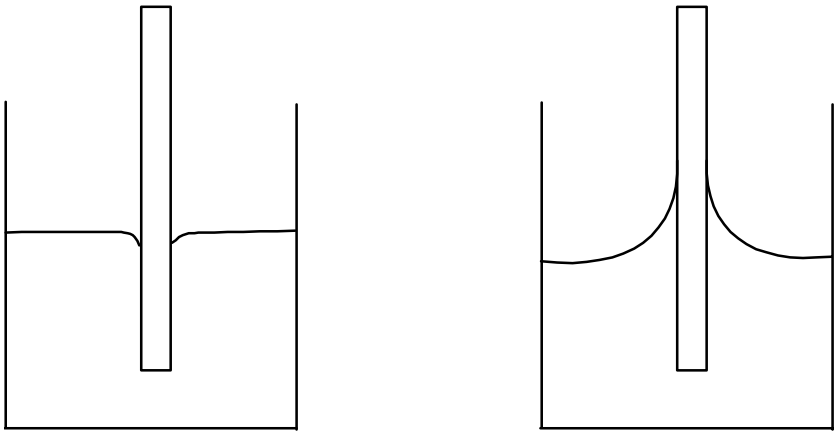
The polymeric fluid has very clearly contrasting effect. The fluid moves inward to the center and starts climbing up the rod. This effect is called the *Weissenberg effect*, as Weissenberg was the first one to explain it. This effect is due the presence of the normal stress differences in the polymeric case, while for the Newtonian fluid the normal stress difference is zero. Associated with shear stress in shear flow are stresses acting perpendicular to the normal surfaces formed by the coordinate axes as shown in figure 1.3. In classical fluid mechanics, these normal stresses, P_{ii}, are equal to the local pressure and hence normal stress differences, $P_{ii} - P_{jj}$, are zero. In case of polymeric fluids, these normal stress differences do not vanish.

1.2.4 Die swell

Polymeric processes sometimes require forcing a polymeric material to flow out of a tube called extruder into the air (figure 1.4). The polymer exhibits die swell, that is, as the fluid leaves the extruder, the diameter of the polymer stream becomes larger than the diameter of the die. This effect is caused by the relaxation of the polymer coils as the stress in a polymeric liquid reduces from the high flow-producing stress within the die to the low stresses associated with the extruder stream moving through ambient air. The Newtonian fluid does not show any increase in the diameter upon leaving a tube.

The above experiments illustrate the different behavior for polymeric fluids compared to Newtonian fluids. They are the phenomena that the ideal constitutive relation should describe [4]:

1. Shear thinning or thickening viscosity.
2. Time dependence.
3. Normal stresses differences different than zero.



N P

Figure 1.2 Rod climbing experiment. The Newtonian "N" fluid shows a vortex; the polymer "P" solution climbs up the rod

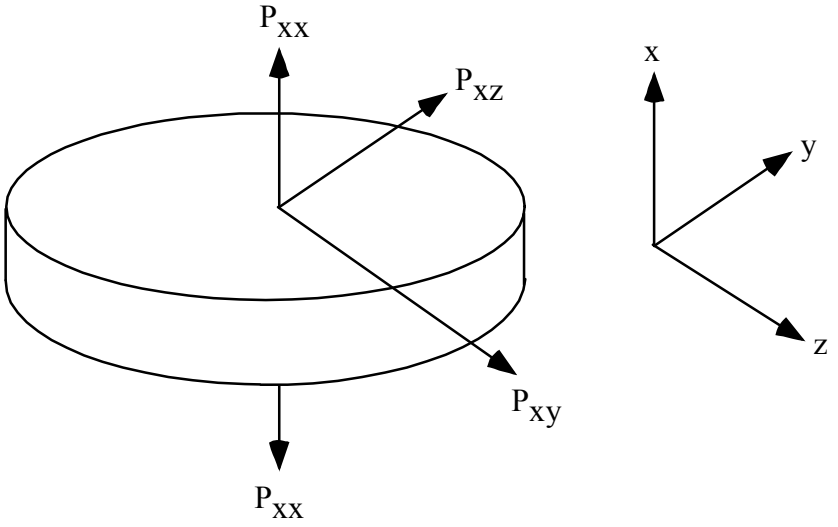


Figure 1.3 Shear stress and normal stresses

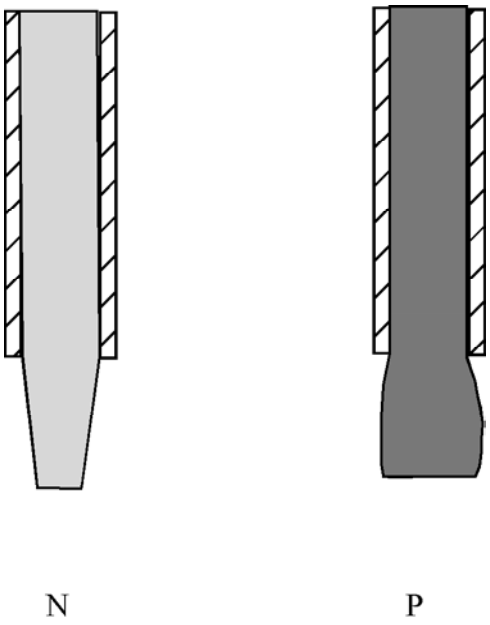


Figure 1.4 Die swell: A stream of Newtonian fluid “N” shows no diameter increase upon flowing out of a tube, a polymeric “P” fluid shows an increase in diameter flowing out of the tube.

1.3 Rheometry

The fundamental difference in Newtonian and non-Newtonian fluid behavior when subject to stress is represented in figure 1.5. The constant viscosity is sufficient to determine the behavior of an incompressible Newtonian fluid under any flow conditions. Measuring the viscosity coefficient requires the use of a device called *viscometer*. The figure shows that the non-Newtonian fluid does not give a constant viscosity value from the nonlinear relation between the stress and deformation. Also, normal stress differences are no longer zero in case of non-Newtonian fluids. The constitutive equation can predict the material rheological properties when subject to stress, but one needs a set of experiments to measure such properties and test such prediction. Measurement of the rheological material functions is called *rheometry*. A rheometer is that device used to measure material functions. The word rheometer can be generic, referring to particular deformation geometry such as cone and plate, or it may refer to a specific instrument for achieving such deformation.

Rheometry has been a subject of many works. Some cover deep details about the mathematical basis and constitutive equations [1,3]; some go into the instrumentation with little attention to the theoretical background [6]; and some cover both the theoretical and the experiment background [4,5].

1.4 Motivation

Figure 1.6 shows the behavior of a non-Newtonian fluid with shear rate. The shear rate covers a wide range from low to the extreme high shear rate. Most polymeric processes are within low to moderate shear rate, where such behavior is accessible to the existing experimental techniques to study the rheological material functions and correlate that with the predicted quantities by the constitutive relations. However, there are high and extremely high shear rate ranges in which several practical processes require knowledge of rheological behavior of materials under such conditions. Systems where high shear rheology is critical include lubrication flow, high-speed coating, and polymer processing. The current research in this area is capable of predicting the behavior of fluid under extreme high shear rate. Despite extensive experimental research in this area,.

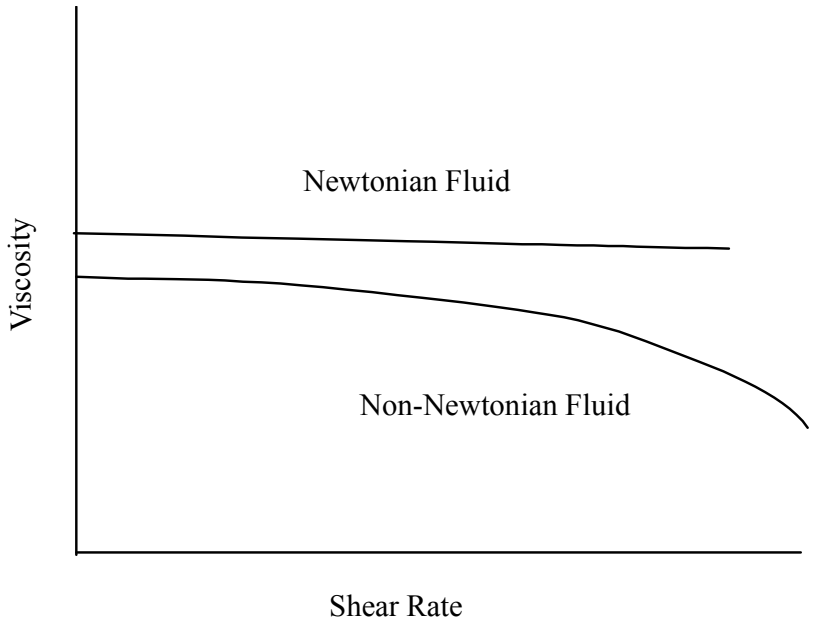


Figure 1.5 Viscosity behaviors for Newtonian and non-Newtonian fluids.

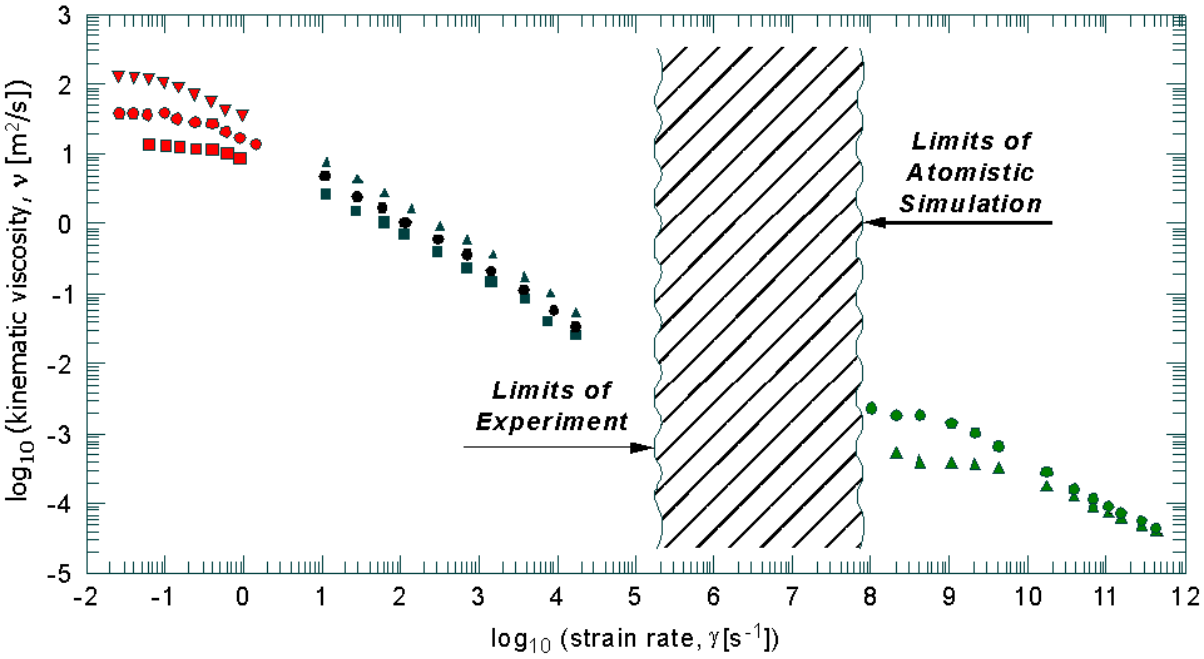


Figure 1.6 Viscosity versus shear rates for non-Newtonian fluid, experimental techniques are limited to moderate shear rate while realistic molecular simulations reach very high rate

the rheological behavior of fluids at high shear rates is not well understood at the fundamental level

A major problem in trying to resolve questions related to high shear rate experiments have been the difficulty of making measurements at high shear rates under well-controlled conditions. Achieving high shear rates in the laboratory is not a difficult problem, but it is difficult to separate the true rheological response from its apparent behavior because of various disturbances that influence the behavior at high flow speeds. The following chapter will have more details and discussion for such difficulties arising during a high shear rate experiment.

The objective of this research is to design and build an apparatus to measure rheological and structural properties of fluids under very high shear rates at near ambient pressures. This allows a predictive theory of flow for complex fluids tested versus convergent simulation and experiment. Experimental data in high shear rate ranges are not available to bridge the gap existing between the current experimental results and simulations results. Knowledge gained from such research has a strong impact on applications in the design of synthetic lubricants and the improvement of polymeric processing techniques.

CHAPTER 2
THEORETICAL BACKGROUND

2.1 Equations of fluid dynamics

When a fluid is subject to a force and the flow is isothermal, its motion is described by the equations of conservation of mass and momentum.

2.1.1 Conservation of mass: Equation of continuity

Assume an arbitrary region of space with volume V and surface S, as in figure 2.1. On every surface element dS there is an outwardly directed normal unit vector **n**. This fixed region is in the midst of a fluid flow field, and the fluid moves across the boundaries of the region. The local rate of mass flow is $\rho(\mathbf{n} \cdot \mathbf{v})dS$, where **v** is the fluid velocity and ρ is the mass density. This rate of flow can be outward or inward. The net rate of outward mass flow can be calculated by integrating over the overall surface S and is given by [1]

$$\int_S \mathbf{n} \cdot (\rho \mathbf{v})\, dS \qquad 2.1$$

This outward flow of mass is balanced by a decrease in the overall mass within V. Thus, the net decrease in the mass in V is given by

$$-\frac{d}{dt}\left(\int_V \rho dV\right) \qquad 2.2$$

The negative sign reflects the decrease in the mass within V.
Combining these two expressions together represents the conservation of the mass.

$$\int_S \mathbf{n} \cdot (\rho \mathbf{v})\, dS = -\frac{d}{dt}\left(\int_V \rho\, dV\right) \qquad 2.3$$

Using the divergence theorem on the surface integral converts the surface as the to

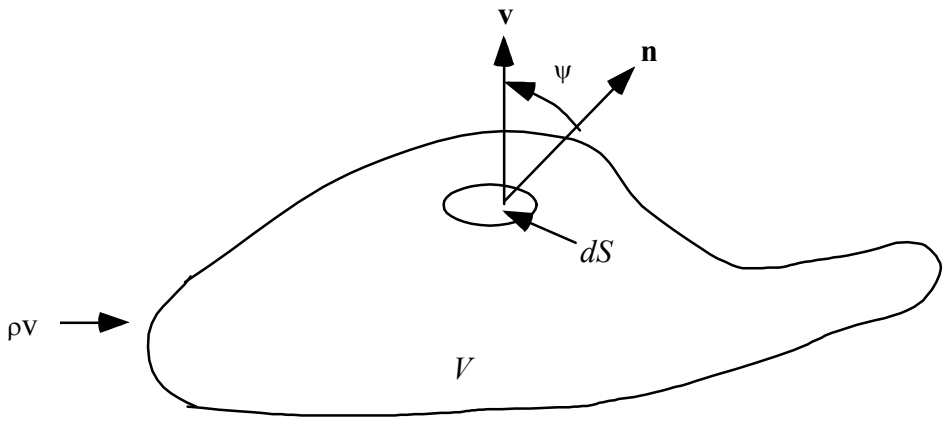


Figure 2.1 Mass and momentum on control volume V.

a volume integral. One obtains the equation for the mass balance that is known as the continuity equation

$$0 = \frac{d\rho}{dt} + \nabla.(\rho \mathbf{v}) \qquad 2.4$$

2.1.2 Conservation of Momentum: Equation of motion

Because the fluid flows across *dS* as in figure 2.1, momentum is carried out across the element of surface *dS* with a rate given by (**n** . **v**)ρ**v** *dS*. This expression can be rearranged as (**n** . ρ**vv**) *dS*. The expression ρ**vv** is the momentum flux (i.e., momentum per unit area per unit time). Sometimes this transport is associated with the bulk flow and referred to as "convective transport" [1,7].

In addition to momentum transported by flow, there is momentum transferred by the molecular forces and interaction within the fluid. This flux of momentum is given by a second order symmetric tensor $\prod$. The component of this tensor $\prod_{ij}$ represents the flux of j-momentum in the i-direction. The rate of flow of momentum resulting from the molecular forces is given by (**n** . $\prod$) *dS*.

The total momentum within *V* will decrease due to a net flux of momentum across S. The law of conservation of momentum can be written as

$$-\frac{d}{dt}\int_V \rho \mathbf{v} dV = \int_S (\mathbf{n} \,.\, \rho \mathbf{vv})\, dS + \int_S (\mathbf{n} \,.\, \prod)\, dS - \int_V \rho \mathbf{g} dV \qquad 2.5$$

rate decrease of momentum of fluid within *V*	rate of momentum outward across S due to bulk flow	rate of momentum outward across S due to body forces	Force on fluid within *V* due to gravity

Using the divergence theorem to change surface integral into volume integral and shrinking the volume to a differential element, since it is arbitrary, results in the differential equation

$$\frac{\partial}{\partial t}\rho v = -\nabla \,.\, (\rho \mathbf{vv}) \; - \nabla \,.\, \prod + \rho \mathbf{g} \qquad 2.6$$

This is called the equation of motion and it is valid for all types of fluids. Combining both equations can give the general equation of motion for any type of fluid (compressible and incompressible fluids)

$$\rho\left(\frac{\partial v}{\partial t} + \mathbf{v}.\nabla\mathbf{v}\right) = -\nabla . \prod + \rho g \qquad 2.7$$

This equation is a powerful tool. It must hold at every point in the flowing fluid. The major element in the equation is the stress tensor $\prod$. To use the equation of motion $\prod$ must be specified.

There are two contributions to the stress tensor: one arises from the thermodynamic pressure p and the second originates from the deformation of the fluid which is referred to as τ. So, the total stress tensor can be written as

$$\prod = p\delta + \tau \qquad 2.8$$

where δ is the unit tensor. The equation describing τ is called a stress constitutive equation. τ is a key parameter to solve the equation of motion and obtain the rheological parameters needed to describe the state of a fluid under stress.

2.1.3 Newtonian fluid

Newton conducted a series of experiments on different incompressible fluids by sliding a plate against a fixed plate while fluid is sheared between the two plates as shown in figure 2.2 [3].

Newton found that the shear stress τ_{21} is proportional to the gradient of velocity and that proportionality constant is the viscosity η.

$$\tau_{21} = \eta\frac{dv_1}{dx_2} \qquad 2.9$$

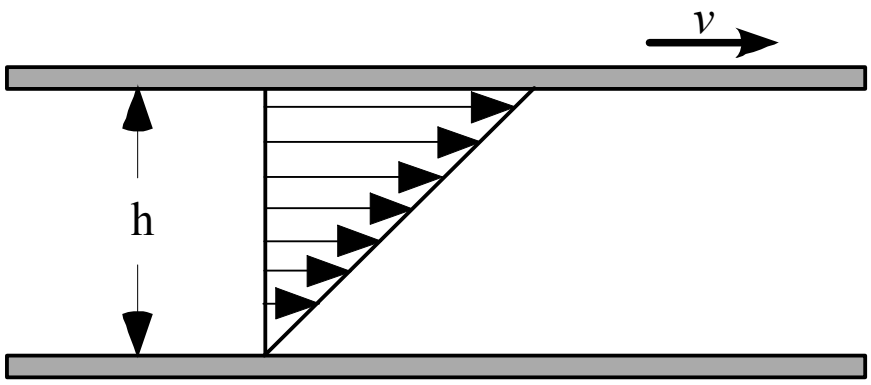


Figure 2.2 Geometry for Newton's experiment

This equation is for the particular flow geometry. The stress due to the fluid deformation can be written as

$$\boldsymbol{\tau} = -\eta[\nabla \mathbf{v} + (\nabla \mathbf{v})^T] \qquad 2.10$$

The tensor in the brackets is called the rate of strain or, in shear flow, the shear rate

$$\dot{\boldsymbol{\gamma}} = \nabla \mathbf{v} + (\nabla \mathbf{v})^T . \qquad 2.11$$

This gives Newton's law of viscosity, $\boldsymbol{\tau} = -\eta \dot{\gamma}$.

2.1.4 Steady simple shear flow

The choice of the flow geometry to probe the rheological behavior of a fluid is arbitrary. Standard flows can be established and need to satisfy two considerations: first, the flow needs to be simple so that the velocity profile or stress field can be calculated; second, the flow situation needs to be experimentally accessible.

Simple shear flow is the most common type of flow discussed in rheology. Figure 2.3 shows the velocity profile for a fluid undergoing simple shear flow between two plates, one plate is fixed and the other is sliding with velocity **v**. In this flow, the velocity has a non-zero component in only one direction, the direction 1 in the figure. Layers of fluid in simple shear flow slide over each other and do not mix except by molecular diffusion as illustrated in figure 2.4 [3]. Within a layer, the distance between the elements sheared fluid is fixed. The velocity profile is given by [1]

$$\mathbf{v} = \begin{pmatrix} v_2 \\ 0 \\ 0 \end{pmatrix} = \begin{pmatrix} \dot{\gamma}_{21} x_2 \\ 0 \\ 0 \end{pmatrix} \qquad 2.12$$

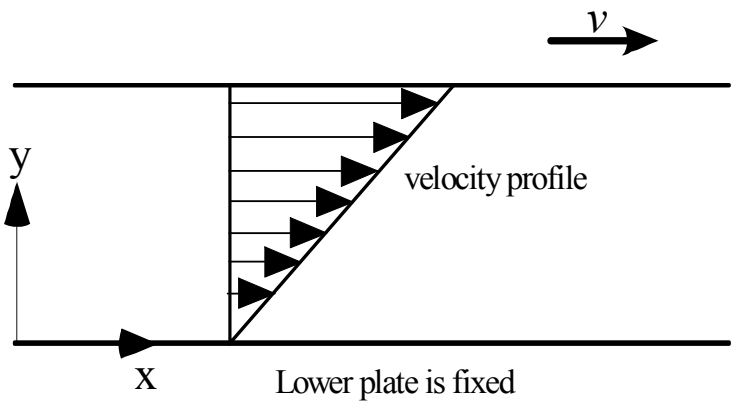


Figure 2.3 Steady state shear flow

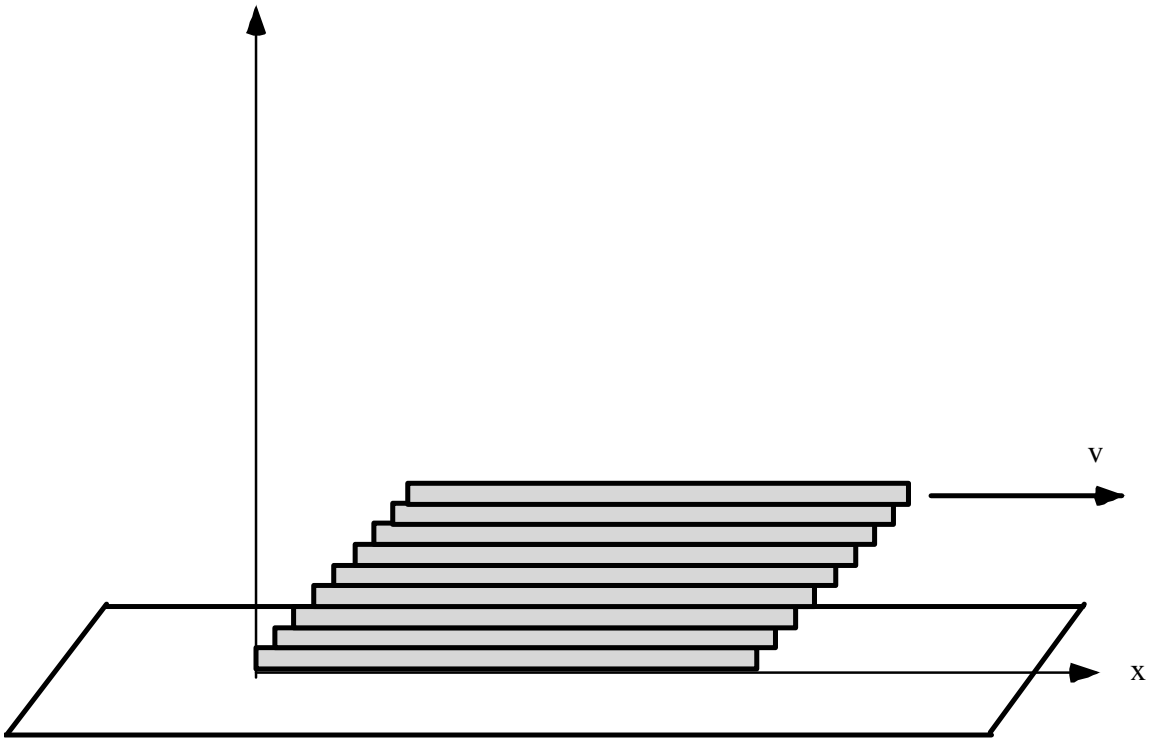


Figure 2.4 Shear planes sliding over each other during steady state flow

where the velocity gradient, $\dot{\gamma}_{21}$, is constant. It is standard to define a certain coordinate system in shear flow. Direction 1 is usually referred to as the flow direction; the direction in which the fluid layers slide. Direction 2 is the velocity gradient direction, and direction 3 is the neutral direction. The velocity gradient tensor has the form

$$\nabla \mathbf{v} = \dot{\gamma} \begin{pmatrix} 0 & 0 & 0 \\ 1 & 0 & 0 \\ 0 & 0 & 0 \end{pmatrix} = \delta_y \delta_x \dot{\gamma} \qquad 2.13$$

where δ_x and δ_y are the unit tensors in the directions 1 and 2 respectively. The shear rate tensor $\dot{\boldsymbol{\gamma}}$ (equation 2.11) is given by

$$\dot{\gamma} \begin{pmatrix} 0 & 1 & 0 \\ 1 & 0 & 0 \\ 0 & 0 & 0 \end{pmatrix} = (\delta_x \delta_y + \delta_y \delta_x) \dot{\gamma} \qquad 2.14$$

In general, the shear stress tensor $\boldsymbol{\tau}$ has nine components. For simple shear flow, the flow is symmetric with respect to 180^o rotation about the 3-axis as in figure 2.5. The symmetry considerations require

$$\tau_{13} = \tau_{31} = 0 \qquad 2.15$$

$$\tau_{23} = \tau_{32} = 0 \qquad 2.16$$

The most general form for the total stress tensor for a simple shear flow is

$$\Pi = p\delta + \boldsymbol{\tau} = \begin{pmatrix} p + \tau_{11} & \tau_{21} & 0 \\ \tau_{21} & p + \tau_{22} & 0 \\ 0 & 0 & p + \tau_{33} \end{pmatrix} \qquad 2.17$$

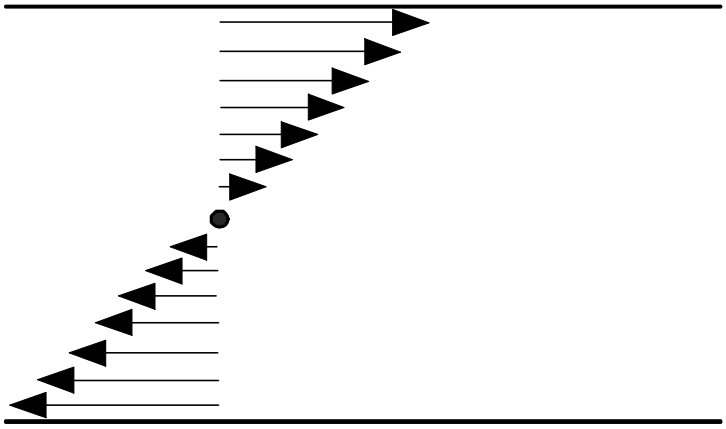


Figure 2.5 Velocity profile with respect to symmetry axis

The quantities of experimental interest are the shear stress and two normal stress differences

Shear stress:	τ_{21}	2.18-a
Primary normal stress difference:	$\tau_{11} - \tau_{22}$	2.18-b
Secondary normal stress difference:	$\tau_{22} - \tau_{33}$	2.18-c

2.1.5 Material functions in steady shear

In steady, simple shear flow, after all transient stresses have died, the stress tensor is constant with time. There are three quantities usually measured in experiments; these quantities are called material functions [1]. The material functions depend upon the shear rate.

Viscosity	$\eta(\dot{\gamma}) = -\frac{\tau_{21}}{\dot{\gamma}}$	2.19-a
First normal stress coefficient	$\Psi_1(\dot{\gamma}) = -\frac{(\tau_{11} - \tau_{22})}{\dot{\gamma}^2}$	2.19-b
Second normal stress coefficient	$\Psi_2(\dot{\gamma}) = -\frac{(\tau_{22} - \tau_{33})}{\dot{\gamma}^2}$	2.19-c

It is common to define the *viscosity* η as the ratio of the steady-state shear stress to the shear rate as in equation 2.19-a. For a Newtonian fluid, the viscosity is shear rate independent and both normal stress coefficients are zero.

2.2 Optical phenomena

Optical techniques are well known in studying polymers especially for the wealth of information they provide on the structure of polymers. When an optical anisotropy is introduced to a transparent polymeric material by mechanical forces such as shearing forces in flow, then optical measurements can provide direct information on the applied

stress. This phenomenon is called *birefringence* and it is a well-established technique in studying polymers in flow. The measured birefringence directly reflects the molecular orientation and shape of a polymeric material under flow which is directly related to the applied stress fields [8].

In a rheological experiment, the measured quantities are related to the forces and/or torques in the system. In the optical experiment, the measured quantities are directly related to structural changes due to the applied stress. Both techniques can be combined together in a rheo-otical experiment. Both techniques can provide sensitivity, spatial resolution, and rapid response to sense shorter time scale effects.

2.2.1 Polarized light

Electromagnetic waves consist of both the electric field vector **E** and the magnetic field vector **B**. For electromagnetic waves propagating in the z-direction, the orthogonal components E_x and E_y of the electric field can be expressed in the following equations [9]

$$E_x(z,t) = E_{ox} \cos(\omega t - k_z z + \delta_x) \qquad 2.20$$

$$E_y(z,t) = E_{oy} \cos(\omega t - k_z z + \delta_y) \qquad 2.21$$

The term $(\omega t - k_z z)$ is the propagator, k is the wave number, ω is the angular frequency, E_{ox} and E_{oy} are the amplitudes, and δ_x and δ_y are the phase shifts. As the electric field vector propagates, it will rotate in space and time according to the phase difference $\delta = \delta_x - \delta_y$, and it will give rise to a vector which describes a locus of points in space. The equation for such vector is

$$\sin^2 \delta = \frac{E_x^2}{E_{ox}^2} + \frac{E_y^2}{E_{oy}^2} - 2\frac{E_x}{E_{ox}}\frac{E_y}{E_{oy}}\cos\delta \qquad 2.22$$

This equation can be decomposed to give rise to different polarization states according to specific values of E_{ox}, E_{oy}, and δ.

Using this representation, linearly horizontal polarization has $E_{oy} = 0$, and the electric field can be represented by

$$E_x(z,t) = E_{ox}\cos(\omega t - k_z z + \delta_x) \qquad 2.23\text{-a}$$

When $\delta = 0^o$ or 180^o, equation 2.22 is reduced to

$$0 = \frac{E_x^2}{E_{ox}^2} + \frac{E_y^2}{E_{oy}^2} \pm 2\frac{E_x}{E_{ox}}\frac{E_y}{E_{oy}}$$

$$E_y = \pm\left(\frac{E_{oy}}{E_{ox}}\right)E_x \qquad 2.23\text{-b}$$

This is equation represents polarization at 45^o; the + is for linearly $+45^o$ polarized light, and the – is for linearly -45^o polarized light. When $E_{ox} = E_{oy}$ and $\delta = 0^o$ or 270^o, that is the case of circularly polarized light.

2.2.2 The Jones Vectors and Stokes Vectors

There is a convenient way of representation for the electromagnetic wave represented in equations 2.20 and 2.21 as

$$\mathbf{E} = \begin{bmatrix} E_x \\ E_y \end{bmatrix} = \begin{bmatrix} E_{ox}e^{i\delta_x} \\ E_{oy}e^{i\delta_y} \end{bmatrix} \qquad 2.24$$

This representation is called the Jones vector [9,8], it is a simple description of light. It assumes monochromatic, perfectly coherent, and perfectly polarized light. It is customary to normalize the Jones vector as follows

$$E_{ox}^2 + E_{oy}^2 = E_o^2 = 1 \qquad 2.25$$

The Jones vector contains complete information about the amplitudes, the phases of the electromagnetic wave, and the polarization of the wave. For example, horizontal, linearly polarized light ($E_{oy} = 0$) can be represented with Jones vectors as

$$\mathbf{E} = \begin{bmatrix} E_{ox} e^{i\delta_x} \\ 0 \end{bmatrix} \qquad 2.26$$

Using the normalization relation, $E_{ox} = 1$ and suppressing the exponent term, the Jones vector for such polarization becomes

$$\mathbf{E} = \begin{bmatrix} 1 \\ 0 \end{bmatrix} \qquad 2.27$$

The elements in a Jones vector can not be measured directly since they are complex vectors. The different possible polarization states of a monochromatic light can be represented by a set of four real quantities, called Stokes parameters, each of which has the dimensions of intensity. For a plane wave represented by equations 2.20 and 2.21, the Stokes parameters are defined as follows

$$S_o = E_{ox}^2 + E_{oy}^2 \qquad 2.28\text{-a}$$

$$S_1 = E_{ox}^2 - E_{oy}^2 \qquad 2.28\text{-b}$$

$$S_2 = 2E_{ox}E_{oy}\cos\delta \qquad 2.28\text{-c}$$

$$S_3 = 2E_{ox}E_{oy}\sin\delta \qquad 2.28\text{-d}$$

S_0 represents the total intensity. S_1 is the difference in intensities between horizontal and vertical linearly polarized components; $I_o - I_{90}$. S_2 is the difference in intensities between linearly polarized light oriented at $+45^o$ and -45^o, $I_{45} - I_{-45}$. S_3 is the difference in intensities between right and left circularly polarized components. The Stokes

parameters describe the polarization state of any optical beam regardless of its state of polarization, from completely polarized to unpolarized light.

The Stokes parameters of monochromatic light can be regrouped in a 4x1 column vector as

$$\mathbf{S} = \begin{bmatrix} S_0 \\ S_1 \\ S_2 \\ S_3 \end{bmatrix} = \{S_0 \quad S_1 \quad S_2 \quad S_3\} \tag{2.29}$$

Jones vectors are compact and easier for manipulation, but they are in terms of amplitudes that cannot be measured directly; on the other hand, Stokes vectors represent intensities, which can be measured directly by optical detectors. Table 2.1 gives the Jones and Stokes representation for various polarization states.

2.2.3 Mueller Matrices and Jones Matrices

The most convenient way to describe the polarization effects of optical elements is by the Stokes vector as described above. The matrices that are used to describe the transformation of polarization state due to particular optical elements are Mueller matrices [9], which are 4x4 real matrices. If **S** represents the Stoke vector of an incident light interacting with an optical element that changes the polarization state as illustrated in figure 2.6 [8], then **S'** is the Stoke vector of the emerging beam; both beams are related through Mueller matrices **M**.

$$\mathbf{A}' = \mathbf{M} \cdot \mathbf{S} \tag{2.30}$$

When working with Jones vectors, the matrices that are used to perform the transformation are called Jones matrices. The elements of Jones matrices, **J**, are complex numbers.

$$\mathbf{A}' = \mathbf{J} \cdot \mathbf{A} \tag{2.31}$$

Table 2.1 Jones and Stokes vectors for various forms of polarized light

Polarization State	Jones Vector (**A**)	Stokes Vector (**S**)
Linearly horizontal polarization	$\begin{bmatrix}1\\0\end{bmatrix}$	$E_{ox}^2\begin{bmatrix}1\\1\\0\\0\end{bmatrix}$
Linearly vertical polarization	$\begin{bmatrix}0\\1\end{bmatrix}$	$E_{oy}^2\begin{bmatrix}1\\-1\\0\\0\end{bmatrix}$
Linearly 45^o polarized	$\frac{1}{\sqrt{2}}\begin{bmatrix}1\\1\end{bmatrix}$	$E_o^2\begin{bmatrix}1\\0\\1\\0\end{bmatrix}$
Linearly -45^o polarized	$\frac{1}{\sqrt{2}}\begin{bmatrix}1\\-1\end{bmatrix}$	$E_o^2\begin{bmatrix}1\\0\\-1\\0\end{bmatrix}$
Right circular polarization	$\frac{1}{\sqrt{2}}\begin{bmatrix}1\\i\end{bmatrix}$	$E_o^2\begin{bmatrix}1\\0\\0\\1\end{bmatrix}$
Left circular polarization	$\frac{1}{\sqrt{2}}\begin{bmatrix}1\\-i\end{bmatrix}$	$E_o^2\begin{bmatrix}1\\0\\0\\-1\end{bmatrix}$

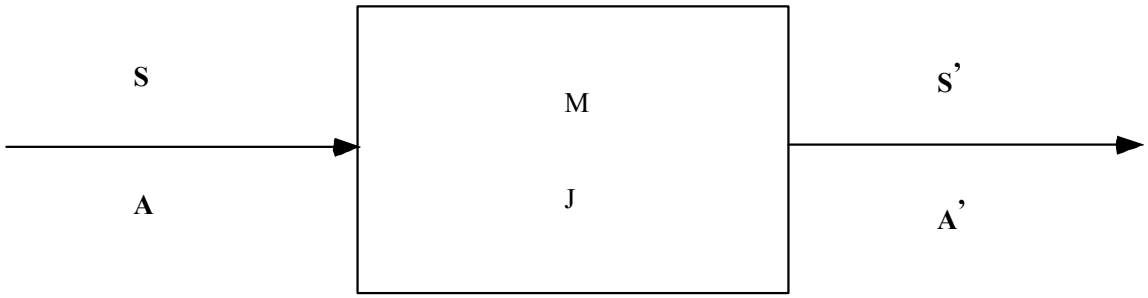


Figure 2.6 Transformation of light by polarizing optical element

Any series of optical elements can be described using Mueller matrices and Jones matrices. If one assumes n optical elements and the incident light is represented with **So**, then the emerged beam after the element n, $\mathbf{S_n}$ can be related to $\mathbf{S_o}$ by

$$\mathbf{S_n} = \mathbf{M_n} \cdot \mathbf{M_{n-1}} \cdots \mathbf{M_2} \cdot \mathbf{M_1} \cdot \mathbf{S_o} \qquad 2.32$$

Where $\mathbf{M_i}$ is the Mueller matrix for the element i. Similarly, the emerged beam $\mathbf{A_n}$ can be related to the incident beam $\mathbf{A_o}$ using Jones matrices

$$\mathbf{A_n} = \mathbf{J_n} \cdot \mathbf{J_{n-1}} \cdots \mathbf{J_2} \cdot \mathbf{J_1} \cdot \mathbf{A_o} \qquad 2.33$$

Where $\mathbf{J_i}$ is the Jones matrix for the element i. It is important to recognize that these matrices are simple matrices and not tensors.

In practice, it is straightforward to derive the Jones matrix of an optical element. Once the Jones matrix elements are obtained, it is possible to derive the Mueller matrix of that particular element using a conversion matrix given in appendix A. Stokes matrices and Jones matrices for various optical elements are also given in appendix A.

2.2.4 Anisotropic Retardation: Birefringence

When a light beam propagates through an isotropically refracting and absorbing material, the light beam is both retarded and attenuated. For such a material, the retardation and attenuation depend on the thickness of the material and are independent of the direction of propagation and state of polarization of the incident beam [10].

The case is different when the material is anisotropic. Retardation and attenuation observed in such materials are dependent on the direction and on the polarization state of the beam. The anisotropic material is characterized with a dielectric tensor of the form

$$\varepsilon_{ij} = \begin{bmatrix} \varepsilon_{xx} & 0 & 0 \\ 0 & \varepsilon_{yy} & 0 \\ 0 & 0 & \varepsilon_{zz} \end{bmatrix} \qquad 2.34$$

where ε_{ij} is the dielectric tensor element. The principal refractive indices n_{ii} are defined

$$n_{ii} = \sqrt{\varepsilon_{ii}} \tag{2.35}$$

Light transmitted through the material along z-axis will be retarded in phase along the x and y axis. The components of the electric field can be written

$$\mathbf{E} = \begin{bmatrix} E_x \\ E_y \\ 0 \end{bmatrix} = \begin{bmatrix} E_{ox}\, \mathrm{expi}(\frac{2\pi n_{xx} z}{\lambda} - \omega t) \\ E_{oy}\, \mathrm{expi}(\frac{2\pi n_{yy} z}{\lambda} - \omega t) \\ 0 \end{bmatrix} \tag{2.36}$$

with

$$n_{xx} = \sqrt{\frac{\varepsilon_{xx}\mu}{\varepsilon_o \mu_o}}; \qquad n_{yy} = \sqrt{\frac{\varepsilon_{yy}\mu}{\varepsilon_o \mu_o}} \tag{2.37}$$

where n_{xx} and n_{yy} are the refractive indices, and μ is the magnetic permeability.

The refractive index tensor $\mathbf{n} = \mathbf{n}' + \mathbf{n}''$ is anisotropic with principle values (n_{xx}, n_{yy}, n_{zz}). The Jones matrix for an element of thickness *d* is

$$\mathbf{J} = \begin{bmatrix} e^{i\frac{2\pi n'_{xx} d}{\lambda}} & 0 \\ 0 & e^{i\frac{2\pi n'_{yy} d}{\lambda}} \end{bmatrix} \tag{2.38}$$

$$= e^{i\frac{2\pi n'_{xx}\, d}{\lambda}} \begin{bmatrix} 1 & 0 \\ 0 & e^{-i\frac{2\pi \Delta n' d}{\lambda}} \end{bmatrix} \tag{2.39}$$

$$= e^{i\frac{2\pi n'_{xx} d}{\lambda}} \begin{bmatrix} 1 & 0 \\ 0 & e^{i\delta'} \end{bmatrix} \quad 2.40$$

where

$$\Delta n' = n'_{xx} - n'_{yy} \quad 2.41$$

is the linear birefringence in the (x, y) plane and

$$\delta' = \frac{2\pi \Delta n' d}{\lambda} \quad 2.42$$

is the retardation.

Similarly, the complex part of the refractive index gives rise to the linear dichroism defined as

$$\Delta n'' = n''_{xx} - n''_{yy} \quad 2.43$$

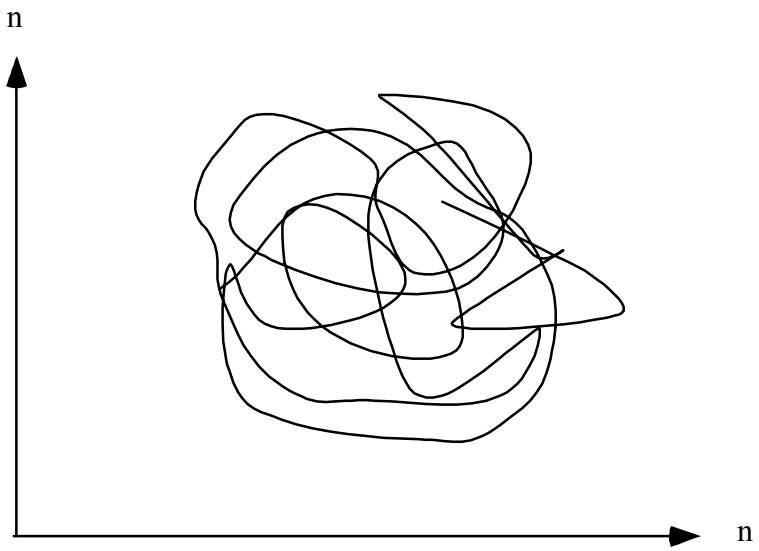
and the extinction is defined as

$$\delta'' = \frac{2\pi \Delta n'' d}{\lambda} \quad 2.44$$

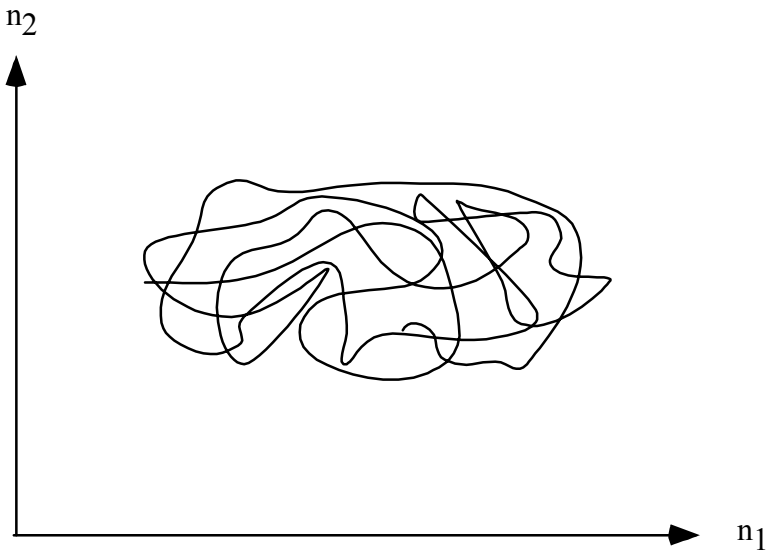
In flow experiments, the stresses generated on the flow of polymer melts and solutions are caused by displacement of polymer chains from their equilibrium random configurations toward elongated configurations. These elongated configurations are not isotropic, and the stressed polymers display anisotropic optical properties or birefringence as illustrated in figure 2.7

2.3 Experimental measurements

Rheo-optical experiments are used extensively in rheology to solve problems in structure and dynamics of complex fluids. The technique of birefringence is a powerful technique and been used in different flow geometries in studying flow-induced conformational changes in polymers.



Isotropic chain, isotropic polarization



Shear applied, chain has orientation, anisotropic polarization

Figure 2.7 Anisotropic polarization due to chain orientation through applying stress

Extensive research has been devoted to study the relationship between the induced anisotropy and the stress field. That relation is known as *stress-optical rule* (SOR), which is an empirical relation between the stress tensor $\boldsymbol{\tau}$ and the index of refraction tensor **n**. Janeschitz-Kriegl [11], J. Wales [12] summarize a comprehensive account of the research in the area of the stress-optical rule.

Birefringence has been used in different rheology experimental configurations to study polymeric systems; the measured quantities are the magnitude of the birefringence and the extinction angle between the flow direction and the optical axis when the system is subject to steady-state flow. Dexter et al. [13] used the flow birefringence to study both the birefringence and the extinction angle for the 1-2 plane, which is parallel to the shear plane, and also for the 1-3 plane, which is perpendicular to the flow plane. Birefringence was used to study the phase separation and the mixing of polymer solutions and blends subject to flow [14].

Takahashi and Fuller [15] used the flow birefringence to measure the stress tensor in one experimental set-up using an oblique transmission with respect to the shear plane. Measuring flow-induced orientation in two-dimensional films was the subject of different flow-birefringence studies to understand the fundamental interactions that control the development of molecular alignment during vertical deposition [16,17].

The measurement of systems under transient-flow conditions became a powerful technique to study the conformational changes under such conditions. Osaki et al. [18] used flow birefringence to study polymer solutions under a time-dependent flow field condition. In their system, two measurements were required at two different configurations to measure the birefringence under such flow conditions. Chow et al. [19] reported using flow birefringence to study transient-flow conditions, but birefringence was measured in one set of experiments.

To date, no high shear-rate flow birefringence experiment has been reported. In this research, a high shear rheometer and a birefringence system are integrated into a high shear rheo-optical apparatus in order to study flow birefringence of complex fluids under high shear rate. Chapter 3 details the concepts behind the design and chapter 4 details this apparatus.

CHAPTER 3
OPTICAL RHEOMETER DESIGN CONCEPTS

3.1 Introduction

This chapter concerns the details of concepts used in designing the high shear-rate optical rheometer in this work.

The continuity equation (conservation of mass), the equation of motion (conservation of momentum), and the constitutive equation, which relates the deformation to stress, all describe the response of a fluid to external forces. The response is different depending on fluid type and shear rate. Newtonian fluids exhibit a directly proportional relation between applied stress and deformation. The response of a non-Newtonian fluid does not follow such a simple relation. Some materials respond with Newtonian behavior within some range of applied stress and show a different response under a higher stress. Table 3.1 contains several examples having different shear rates along with practical situations where such ranges are applicable.

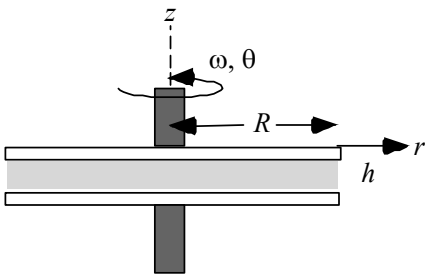
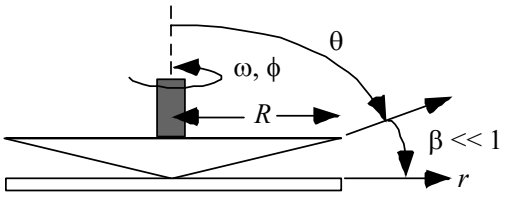
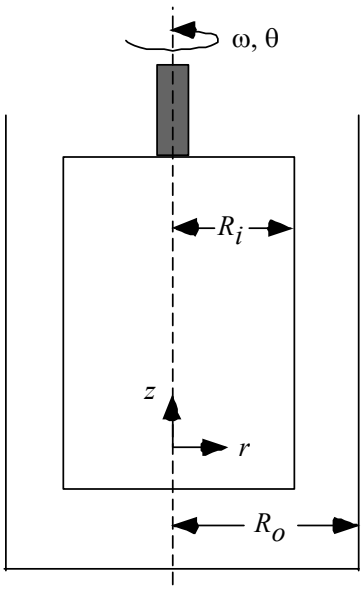
To describe the rheological behavior of a fluid, some conditions are imposed, and the fluid response is observed. In one approach, a deformation can be imposed on a fluid, and then the stresses generated are measured. In another approach, stress is imposed on a fluid, and the deformation is measured. Table 3.2 gives a summary of some common viscometric flow geometries [1]. Each represents a deformation imposed in a certain coordinate system with well-defined geometry. In these geometries, the flow is a simple shear flow in which the mathematical description of the stress and deformation allows straightforward experimental measurements. The most commonly used flow geometries are two parallel-plates, cone-plate, and concentric cylinders. These are called drag-flow techniques, in which the shear is generated between moving and fixed surfaces.

High shear rates represent a very important range for many practical processes such us lubricant flow, spin coating, and polymeric processing. A major obstacle in trying to study rheological effects under high shear rates has been making measurements under well-controlled conditions. The obstacle arises from the difficulty in separating the true rheological response from various disturbances that influence the hydrodynamics at

Table 3.1 Typical shear rates for familiar materials processes

Situation	Shear rate (s^{-1})	Application
Draining under gravity	10^{-1} - 10^{1}	Painting
Extruders	10^{0} - 10^{2}	Polymers
Mixing	10^{1} - 10^{3}	Manufacturing of liquid
Rubbing	10^{4} - 10^{5}	Rubbing lotion on skin
High speed coating	10^{5} - 10^{6}	Paper coating
Lubrication	10^{3} - 10^{8}	Engines, computer hard disk

Table 3.2 Common shear flow geometries

Flow	Coordinates	Velocity Field
a. Parallel-plates rotational flow 	r	$v = v_\theta(r, z)$
	θ	$v_r = 0$
	z	$v_z = 0$
b. Parallel-plates rotational flow 	r	$v = v_\phi(r, \theta)$
	θ	$v_r = 0$
	ϕ	$v_\theta = 0$
c. Concentric cylinders (Couette geometry) flow 	r	$v = v_\theta(r)$
	θ	$v_r = 0$
	z	$v_z = 0$

high flow speed. The most difficult problem is the viscous heat generation at high shear rates. At high shear rates, viscous heating can cause an increase in temperature, which causes a decrease in the observed viscosity.

Several types of experimental set-up are used for measuring rheological behavior of fluids at high shear rates. Van Wazer et al. [6], describe several techniques in detail. Capillary flow is the oldest technique. Capillary flow represents pressure driven flow in which shear is generated between the stationary capillary wall and the fluid driven by a pressure difference over a closed channel. In capillary flow, the fluid is forced to flow out of a bore by imposing pressure. By measuring the volumetric flow rate and the pressure, the viscosity of a Newtonian fluid can be determined. If the fluid is not Newtonian, the velocity profile must be assumed or measured. Lodge [20] measured shear rates up to 10^6 s^{-1} based on a pressure-driven slit-die design. The technique is based on forcing the liquid through a thin rectangular channel or slit. Viscous heating can affect the data, and a correction is used to adjust the data. A disadvantage of the slit-flow technique is the inability to measure lower shear rate and stress.

Couette geometry (with two concentric cylinders, one fixed and the other rotating) has been used for measuring high shear-rate rheology [21]. The shear rate and shear stress are determined by measuring the separation, rotating speed, and the torque maintaining the rotation. Viscous heat is a major difficulty in such flow.

The cone-plate geometry is used to measure rheology up to a moderate shear rate range [4,5]. The shear rate is calculated by measuring the rotational speed and the cone angle. Shear stress is determined by measuring the torque required to maintain the rotation on the plate and the known radius of the plate. The range is limited by the cone angle and viscous heat.

Parallel-plate rotational geometry [22,23,24] can be used to achieve high shear rates by operating the rheometer at small gaps to dissipate the viscous heat and avoid its effects.

3.2 Parallel plate rheometry

3.2.1 Theory of the parallel-plate rotational rheometer

Mooney [25] first suggested the parallel disk geometry, but the original design consisted of a disk rotating inside a cylindrical cavity. Figure 3.1 shows two parallel-disks in which one plate is fixed and the other is rotating at constant angular velocity Ω. The coordinate system is (r, θ, z) where θ is the flow direction, z is the velocity gradient direction, and r is the neutral direction. The only non-zero velocity component is v_θ

$$v = \begin{bmatrix} 0 \\ v_\theta \\ 0 \end{bmatrix} \tag{3.1}$$

The flow between the two plates is assumed to be steady, laminar, and isothermal [4]. The continuity equation can be written as $\partial v_\theta / \partial \theta = 0$. The velocity profile can be written as

$$v_\theta = A(r)z + B(r) \tag{3.2}$$

Using the boundary conditions Ω(z = 0) = 0, Ω(z = h) = Ω., where h is the gap height between the two plates, the velocity equations becomes

$$v_\theta(r,z) = \frac{r\Omega z}{h} \tag{3.3}$$

The rate of deformation tensor (equation 2.11) becomes [3]

$$\dot{\gamma} = \begin{bmatrix} 0 & \frac{\partial v_\theta}{\partial r} - \frac{v_\theta}{r} & 0 \\ \frac{\partial v_\theta}{\partial r} - \frac{v_\theta}{r} & 0 & \frac{\partial v_\theta}{\partial z} \\ 0 & \frac{\partial v_\theta}{\partial z} & 0 \end{bmatrix} = \begin{bmatrix} 0 & 0 & 0 \\ 0 & 0 & \frac{r\Omega}{h} \\ 0 & \frac{r\Omega}{h} & 0 \end{bmatrix} \tag{3.4}$$

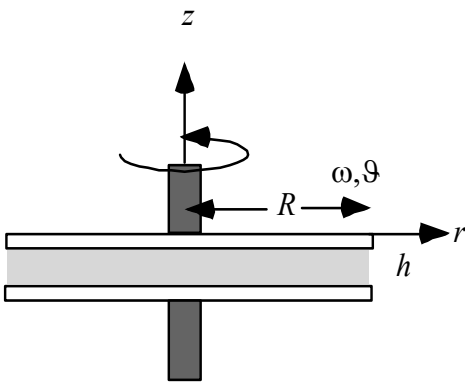


Figure 3.1 Schematic of parallel-plate rheometer

The shear rate is given by

$$\dot{\gamma} = \left| \dot{\gamma} \right| = \frac{r\Omega}{h} \tag{3.5}$$

The above equation shows that the shear rate has a radial dependence and is not homogenous.

The viscosity is calculated from the ratio of the shear stress to the shear rate

$$\eta = \frac{-\tau_{z\theta}}{\dot{\gamma}(r)} \tag{3.6}$$

The shear stress for flow between two plates is given by [3]

$$\boldsymbol{\tau} = \begin{bmatrix} \tau_{rr} & 0 & 0 \\ 0 & \tau_{\theta\theta} & \tau_{z\theta} \\ 0 & \tau_{z\theta} & \tau_{zz} \end{bmatrix} \tag{3.7}$$

The equation of motion (equation 2.7) can be written for the flow between two parallel-plates.

$$\begin{bmatrix} -\frac{\rho v_\theta^2}{r} \\ 0 \\ 0 \end{bmatrix} = \begin{bmatrix} 0 \\ 0 \\ 0 \end{bmatrix} - \begin{bmatrix} \frac{1}{r}\frac{\partial}{\partial}(r\tau_{rr}) - \frac{\tau_{\theta\theta}}{r} \\ \frac{\partial \tau_{z\theta}}{\partial z} \\ \frac{\partial \tau_{zz}}{\partial z} \end{bmatrix} \tag{3.8}$$

The θ - component of the equation of motion gives

$$\frac{\partial \tau_{z\theta}}{\partial z} = 0 \tag{3.9}$$

$$\tau_{z\theta} = C(r) \tag{3.10}$$

The total torque M required to turn the rotating plate is given by

$$M = \int_A (\tau_{z\theta})(r)dA \tag{3.11}$$

By measuring the shear forces at a distance r, the shear stress can be calculated, and the viscosity can be calculated from equation 3.6.

The parallel plate geometry can be very useful to measure material functions at high shear rates. Equation 3.5 suggests high shear rates are attainable by increasing rotational speed or decreasing gap. By taking this approach, problems normally generated in high-speed flows are reduced.

The magnetic hard disk drive system consists of a multilayer disk and a head with motion relative to each other as in figure 3.2. The disk is mounted on a ball-bearing spindle and rotated with constant speed. The head has much smaller area compared to the disk area and has a rectangular surface; it floats over the disk with a suspension system allowing the interface to be at nanometer scale. The hard-disk configuration has been used to study the tribology of the interface and the wear of the disk due to disk-head interaction. This is usually done by studying the friction force. Recently it has been used to study the viscosity of thin films at the interface [23,24]. The configuration of the hard disk drive system with one plate flying allows one to achieve high shear rates by using thin films and higher rotational speeds.

3.2.2 Viscous heating

In a shearing fluid, some energy is dissipated as heat. This generated heat causes temperature to increase within the liquid [26]. The viscosity dependence on temperature can be given approximately by

$$\eta = Ae^{bT} \tag{3.12}$$

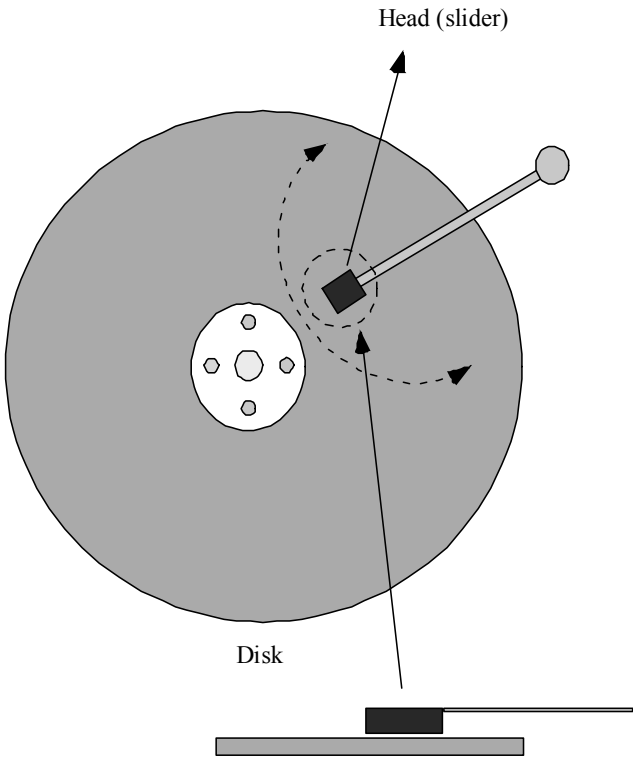


Figure 3.2 Hard disk drive system

where A is a constant, b is the temperature sensitivity of the viscosity and depends on the activation energy of the flow process. This viscosity-temperature dependence arises from the fact that a molecule must posses enough energy to overcome a potential energy barrier to move from one equilibrium position to next. The equation shows that a temperature increase can affect viscosity and manifests itself as a rheological shear-thinning effect especially in liquids of low thermal conductivity.

For a system of fluid between two surfaces (figure 3.3) where one is fixed and the other is moving at speed v, the energy equation is given by [1]

$$\rho c_{\mathrm{v}} \frac{\mathrm{DT}}{\mathrm{Dt}} = k\nabla^2 + \Phi \qquad 3.13$$

where ρ is the density, c_v is the specific heat, T is the temperature, t is the time, k is the thermal conductivity, and Φ is the dissipation function.

Assuming viscosity, η, and thermal conductivity, k, to be temperature-independent (the validity of the assumption about viscosity is to be examined shortly) and for laminar flow with $\mathrm{v} = v_{\mathrm{x}}(y)$, $v_{\mathrm{y}} = v_{\mathrm{z}} = 0$, the equation of motion can be solved, and the velocity distribution is given by

$$v_x = v_{\mathrm{o}}\left(\frac{y}{h}\right) - \frac{1}{2\eta}\frac{\partial \mathrm{p}}{\partial \mathrm{x}}\left[hy - y^2\right] \qquad 3.14$$

Since the physical properties are assumed to be constant and the momentum is independent of x, then $\partial \mathrm{p} / \partial \mathrm{x} = 0$.

The temperature can be assumed as $\mathrm{T} = \mathrm{T}(y)$. Then the dissipation function Φ can be written as

$$\Phi = \eta\left(\frac{\mathrm{d}v_{\mathrm{x}}}{\mathrm{d}y}\right) \qquad 3.15$$

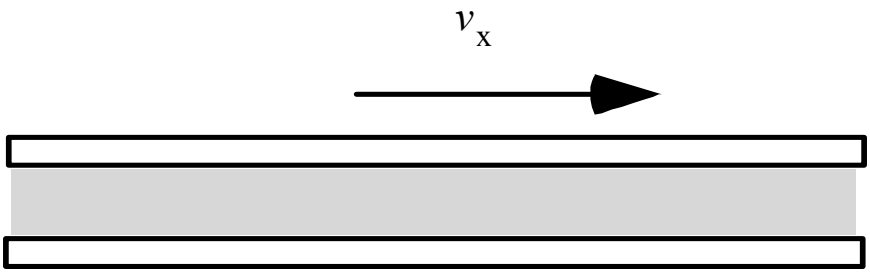


Figure 3.3 Schematic of flow between horizontal plates

Using the above solution for the velocity distribution, the dissipation function becomes

$$\Phi = \eta\left(\frac{v^2}{h}\right) \qquad 3.16$$

Then the equation of energy can be solved using the following boundary conditions

$$\text{At} \qquad y = 0,\ T = T_o \qquad 3.17.a$$

$$\text{At} \qquad y = h,\ T = T_o \qquad 3.17.b$$

The resulting temperature distribution is

$$T - T_o = \frac{\eta v^2}{2kh^2}\left[hy - y^2\right]. \qquad 3.18$$

The maximum temperature increase occurs at $y = h/2$

$$\Delta T_{max} = \frac{\eta v^2}{8k} \qquad 3.19$$

The estimated change in viscosity due to change in temperature is given by [23]

$$\Delta\eta = b\Delta T \qquad 3.20$$

Combining equations 3.19 and 3.20 yields

$$\Delta\eta = \frac{b\eta v^2}{8k} \qquad 3.21$$

Using the above equation, one can estimate the change in the viscosity due to a change in temperature. For the Fomblin YR lubricant used in this study, this estimate gives an increase in viscosity of less than 1.5%, which shows the validity of the assumption of temperature-independence for the system described in this work.

3.3 Capacitance

Equation 3.5 indicates that higher shear rates can be obtained in a rotational rheometer using a thinner film between the two parallel-plates. The shear rate is calculated in such system by measuring the rotational velocity and the thickness of the film between the two plates. Typically, film thickness has been measured before loading the sample to the instrument by ellipsometry or other film thickness measuring technique. This approach may cause an error in the measured quantities due to change in thickness of the film as function of normal pressure and sliding speed.

The film thickness can be measured and monitored in situ by using a capacitance approach. The plates can be conductive and the capacitance between the two plates can be measured. The capacitance between two nonparallel plates shown in figure 3.4 is given by

$$C = \frac{\varepsilon_r \varepsilon_o w}{\theta}\left(1 + \frac{l \sin\theta}{h}\right) \qquad 3.22$$

where w and l are the width and the length of plates, respectively., θ is the angle between the two plates, and ε_r and ε_o are the film dielectric constant and vacuum permittivity respectively; for Fomblin YR ε_r is 2.1, For two parallel plates $\theta = 0$, and equation 3.22 reduces to

$$C = \frac{\varepsilon\varepsilon_o A}{h} \qquad 3.23$$

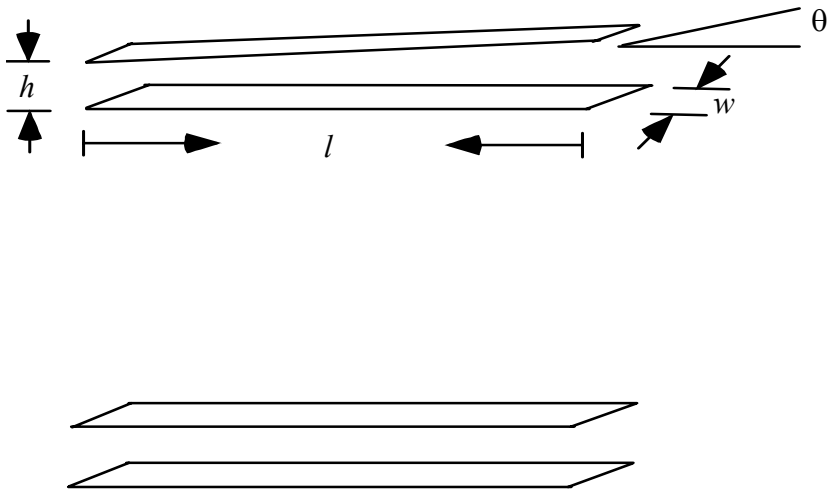


Figure 3.4 Nonparallel and parallel plates

where A is the plate area, h is the thickness, ε_o is the vacuum permittivity, and ε is the dielectric constant of the material between the plates. By measuring the capacitance, the film thickness can be determined and monitored during the experiment.

3.4 Optical rheometry

The rheology experiment entails the measurements of a force and either a displacement or velocity. The mechanical response senses the dissipation of energy. This response is integrated over the entire sample. In contrast, an optical signal can directly reflect the molecular orientation and shape, and it may sense some optical property due to applied stress. Both the mechanical measurements and optical measurements can be combined into a *rheo-optical* experiment. These can be complementary approaches.

The birefringence of a material, the difference in the refractive indices along two selected orthogonal axes, has been found often to be directly proportional to the stresses, and it can provide a good way of measuring stress fields in some systems.

3.4.1 Birefringence measurement

The design of an optical experiment integrates different optical elements suitable to obtain desired structural and dynamic information from the sample under study. In a birefringence experiment, the material is viewed between two crossed polarizing elements to sense the changes within the sample. When an isotropic liquid is at rest between two crossed polarizes, there is no signal coming out of the second polarizer. When the liquid is subject to hydrodynamic forces, then biaxial anisotropy occurs. That is, the sample becomes birefringent; it possesses three different principal axes with three different refractive indices. One of these is axes is in the light direction, and the other two lie in the plane of observation. When linearly polarized light passes through a doubly refracting medium it is resolved in two linearly polarized light components, one along each principle axis. These components emerge with phase difference, or retardation δ. The two measured quantities in a birefringence experiment are the

magnitude of retardation due to the applied stress and the extinction angle between the principle refractive index $\mathbf{n_1}$ and the flow direction **1** as in figure 3.5.

There are different experimental designs for measuring flow birefringence. Fuller [8] has a comprehensive discussion of different setups for optical rheometry. The basic setup adapted in the present work is suitable for measuring flow birefringence in the flow situation between the two parallel-plates in a rotational rheometer. It is capable of probing the structural changes within the time scale of the experiment. The design used in the present work is based on the *polarization modulation technique* (PMT).

3.4.2 Polarization modulation Technique

The polarization modulation technique is one in which polarized light is modulated through a time-dependent variation of an optical element. This modulation can be through rotation of the optical element with fixed optical properties or fixed orientation with modulated optical properties. A typical design includes a polarizing element and a polarization modulation element, which is called a polarization state generator (PSG). An alternative design includes a polarization modulation element and a polarizing element acting as analyzer, which is referred to as polarization state analyzer (PSA). The modulation can be in the PSG section of the instrument, the PSA section, or in both sections. The design used in the current work is based on using a PSG made of a polarizing element and a polarization modulation element. Details of the optical train are given in the next chapter.

3.4.3 Photoelastic modulator (PEM)

A normally isotropic element is set into time-dependent oscillation by means of attachment to a crystal driven by an external ac voltage [27]. Typically, the isotropic element is fused silica attached to a vibrating crystal quartz as shown in figure 3.6. A modulator of such kind is a photoelastic modulator (PEM). When a PEM is used with a linear polarizer oriented at $\pm 45^{o}$ with respect to the PEM, then the resulting polarization state of the light emerging from the polarizer-PEM is elliptically polarized. The polarization state oscillates between linear, elliptical, and circular polarization states,

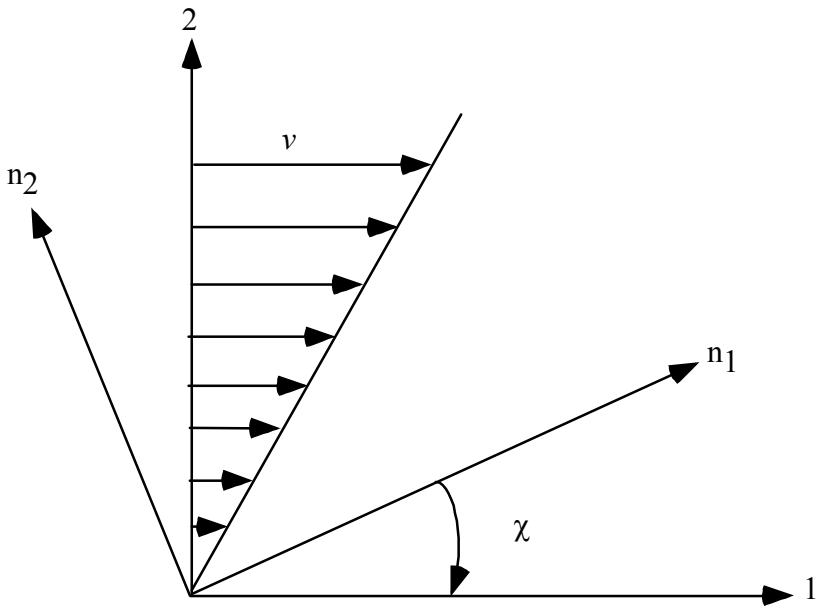


Figure 3.5 Axes of stresses and refractive indices in simple shear

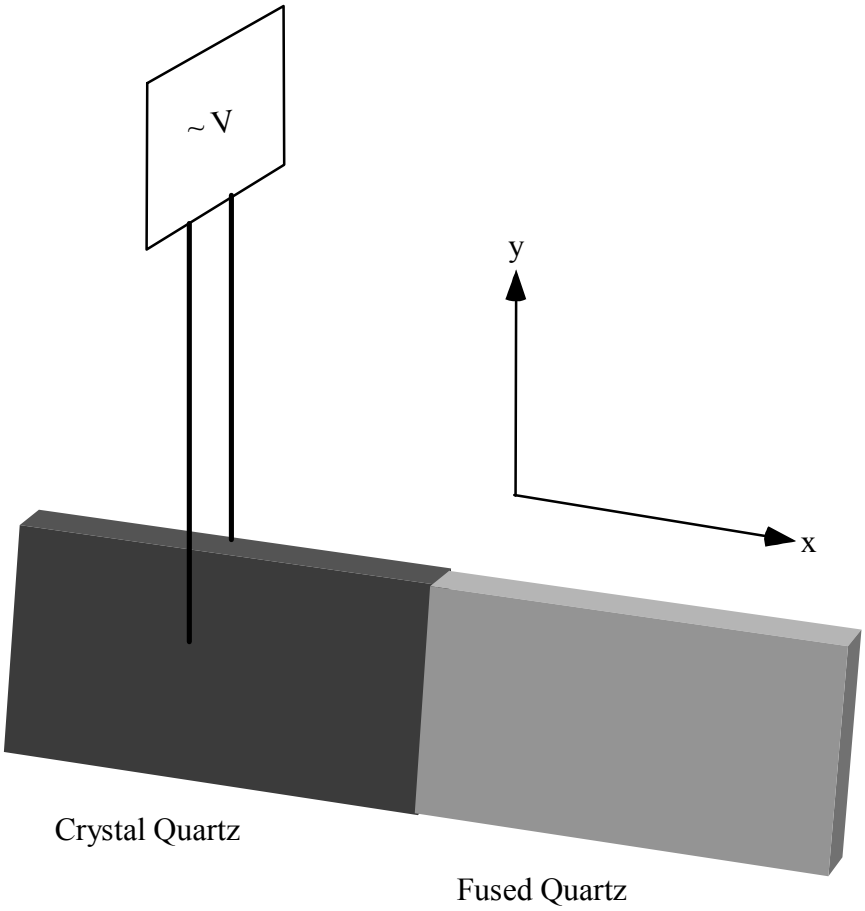


Figure 3.6 Photoelastic Modulation (PEM)

depending on the strain status of the PEM as illustrated in figure 3.7.

All optical elements contain some residual static strain, which introduces static retardation in the element. This might be introduced during the manufacturing process of the element. The static retardation, which is referred to as δ_o, normally is small (~0.003 rad).

Figure3.7 shows the configuration of a PEM [28] in which applied ac voltage acts on the driving element which dynamically strains the optical element through which light passes. The optical element oscillates in a way such that it expands in one of its axis directions, resulting in contraction in the other axis direction. For example, expansion along the x-axis means contraction along the y-axis direction, making the optical element optically uniaxial. The retardation of the device can be expressed as [10]

$$\delta = \frac{d}{\lambda}\pi n^3(\lambda)(q_{11} - q_{12})(P_{xx} - P_{yy}) = \frac{d}{\lambda}\pi n^3(\lambda)Q(\lambda)P \qquad 3.24$$

where d is the thickness of the optical element, λ is the wavelength of light, $n(\lambda)$ is the unstrained refractive index of the element at wavelength λ, P_{xx} (P_{yy}) is the strain in the xx (yy) direction, and q_{11} (q_{12}) is the strain-optic coefficient.

Since the driving element is driven by an oscillating voltage with frequency ω, then at any point (x, y) within the optical element the strain is given by

$$P(x, y, t) = P_o(x, y) + \sum_k P_k \sin(k\omega t + \phi_k) \qquad 2.25$$

where $P_o(x, y)$ is the strain at (x,y) through the optical element, and ϕ_k is the phase difference for the k^{th} harmonic of ω. The equation above assumes the direction of the static strain is along either the x- or the y- axis of the optical element. In most cases, the first harmonic term is the dominant term. Using the P expression (equation 2.25) in equation 2.24, the retardation in the optical element can be written as

$$\delta = \frac{d}{\lambda}\pi n^3(\lambda)Q(\lambda)(P_o + P_1 \sin(\omega t + \phi_o) = A(\lambda)\sin(\omega t + \phi_o) + \delta_o(\lambda) \qquad 3.26$$

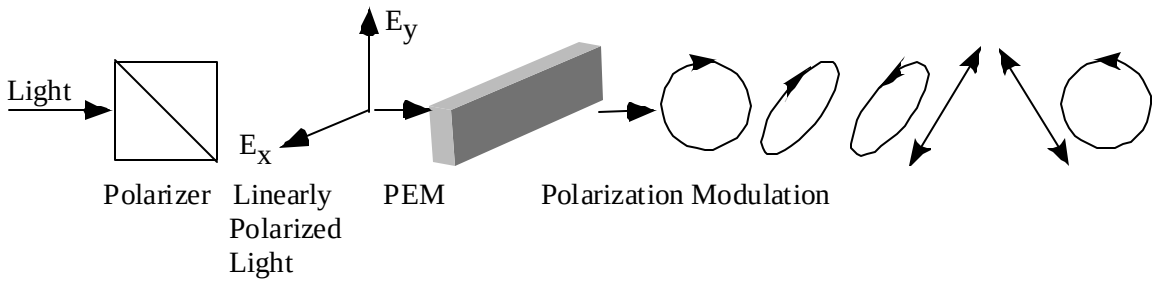


Figure 3.7 Polarization modulation technique

In most cases, the amplitude of modulation P_1 is controlled by an external ac voltage V_m. The relation between P_1 and V_m is assumed to be a linear relation

$$P_1 = K_m V_m \tag{3.27}$$

Then

$$V_m = \frac{P_1}{K_m} = \frac{A_o \lambda}{K_m d \pi n^3(\lambda) Q(\lambda)} \tag{3.28}$$

The above equation represents the relation between the amplitude of the applied voltage and the response of the photoelastic modulator to that voltage.

3.4.4 Stokes vector description of polarimetry design

In polarimetry experiments, the most common arrangement of optical elements consists of polarizer and polarizer-PEM pairs, which can be azimuthally rotated about the input or output beam direction. In the visible region of the spectrum, polarizes are nearly perfect, and in the following it will be assumed they are perfect. The Stokes representations for each of these arrangements is [28]

1) Polarizer acting as PSG

When a polarizer is used as a polarization state generator, the Stokes vector for the polarized light emerging from the polarizer is

$$\mathbf{S}_{PSG} = \mathbf{R}(-\theta_p)\mathbf{M}_p\,\mathbf{R}(\theta_p)\begin{pmatrix}1\\0\\0\\0\end{pmatrix} = \begin{pmatrix}1\\C_p\\S_p\\0\end{pmatrix} \tag{3.29}$$

where $S_p = \sin(2\theta_p)$; $C_p = \cos(2\theta_p)$, θ_p is the angular position of the polarizer with respect to a reference axis, $\mathbf{R}(\theta)$ is the rotational matrix from one frame to another with angle θ between the two frames.

2) Polarizer acting as PSA

When a polarizer is used as a polarization state analyzer, the emerging light Stokes vectors is

$$S_{PSA}^{T} = \begin{pmatrix} 1 & 0 & 0 & 0 \end{pmatrix} \mathbf{R}(-\theta_p)\mathbf{M}_p\, \mathbf{R}(\theta_p) = \begin{pmatrix} 1 & C_p & S_p & 0 \end{pmatrix} \tag{3.30}$$

where same notation is used as in the previous case.

3) Polarizer-photoelastic modulator (PEM) pair acting as PSG

The most common configuration uses the polarizer-PEM to modulate the polarization. The azimuthal angles of the PEM is θ_m, and for the polarizer, θ_p, then the Stokes vector for the light beam is

$$\mathbf{S}_{PSG} = \mathbf{R}(-\theta_m)\mathbf{M}_m\, \mathbf{R}(\theta_m)\mathbf{R}(-\theta_p)\mathbf{M}_p\, \mathbf{R}(\theta_p) \begin{pmatrix} 1 \\ 0 \\ 0 \\ 0 \end{pmatrix} \tag{3.31}$$

where $\mathbf{M}_m$ is the Mueller matrix for the modulator. For a modulator with optical retardation δ the Mueller matrix is given by

$$\mathbf{M}_m = \begin{pmatrix} 1 & 0 & 0 & 0 \\ 0 & 1 & 0 & 0 \\ 0 & 0 & \cos(\delta) & \sin(\delta) \\ 0 & 0 & -\sin(\delta) & \cos(\delta) \end{pmatrix} = \begin{pmatrix} 1 & 0 & 0 & 0 \\ 0 & 1 & 0 & 0 \\ 0 & 0 & Y_\delta & X_\delta \\ 0 & 0 & -X_\delta & Y_\delta \end{pmatrix} \tag{3.32}$$

The quantities Y_δ and X_δ contain all of the time dependence in the expression for the PSG. Using equation 3.26 and considering the phase difference ϕ_k to be zero, X_δ and Y_δ can be written as

$$\begin{aligned} X_\delta &= \sin(A \sin(\omega t) + \delta_o \\ &\sim \sin(A \sin(\omega t) + \delta_o \cos(A \sin(\omega t)) = X + \delta_o Y \end{aligned} \tag{3.33}$$

$$X_\delta = \cos(A \sin(\omega t) + \delta_o)$$
$$\sim \cos(A \sin(\omega t) - \delta_o \sin(A \sin(\omega t)) = Y + \delta_o X \qquad 3.34$$

where the approximation above assumes that δ_o is small.

The basis functions for the polarizer-PEM pair X and Y are related to the trigonometric basis functions using an infinite series of integer Bessel functions.

$$X(t) = \sin(A \sin(\omega t) = 2\sum_{j=0} J_{2j-1}(A)\sin((2j-1)\omega t) \qquad 3.35$$

$$Y(t) = \cos(A \sin(\omega t) = J_o(A) + 2\sum_{j=1} J_{2j}(A)\sin(2j\omega t) \qquad 3.36$$

The integer Bessel functions are functions of the Bessel angle A, which depends on the modulator retardation and is usually proportional to the drive voltage as in equation 3.28.

Combining the different elements for the polarizer-PEM pair together gives the Stokes vector for the pair

$$\mathbf{S}_{PSG} = \begin{pmatrix} 1 \\ C_m C_b + S_m S_b Y_\delta \\ S_m C_b - C_m S_b Y_\delta \\ S_b X_\delta \end{pmatrix} \qquad 3.37$$

where $S_m = \sin(2\theta_m)$, $C_m = \cos(2\theta_m)$, $S_p = \sin(2\theta_p)$, $C_p = \cos(2\theta_p)$, $\theta_b = \theta_m - \theta_p$. Most polarizer-PEM systems are configured with $\theta_b = \pm 45^o$; then the Stokes vector for the polarizer-PEM becomes

$$\mathbf{S}_{PSG} = \begin{pmatrix} 1 \\ \pm(-2C_m + S_m Y_\delta) \\ \mp(2S_m - C_m Y_\delta) \\ \pm X_\delta \end{pmatrix} \qquad 3.38$$

3.4.5 Intensity for PSG PSA configuration

Figure 3.8 represents a basic setup of a transmission-polarization design in which light passes through a polarization element and a polarization modulation element (together forming PSG), sample S, then another polarizing element acting as PSA before falling on a detector [28,8]. The Stokes vector for the light received at the detector is given by

$$\mathbf{S}_d = \mathbf{M}_{PSA} \,.\, \mathbf{M}_S \,.\, \mathbf{M}_{PSG} \,.\mathbf{S}_o \qquad 3.39$$

where Ms are the Mueller matrices for the elements, and Ss are the Stokes vectors for the elements.

The light intensity on the detector can be obtained by matrix multiplication

$$I = Io(\mathbf{S}_{PSA}^{T}\ \mathbf{M}\ \mathbf{S}_{PGA}) \qquad 3.40$$

where matrix M is the Mueller matrix for all elements between the PSG and the PSA.

The design of a particular experiment requires the specification of the elements to be measured in the matrix of the sample $\mathbf{M}_S$. $\mathbf{M}_S$ can be expressed in its general form as

$$\mathbf{M}_S = \begin{bmatrix} 1 & m_{12} & m_{13} & m_{14} \\ m_{21} & m_{22} & m_{23} & m_{24} \\ m_{31} & m_{32} & m_{33} & m_{34} \\ m_{41} & m_{42} & m_{43} & m_{44} \end{bmatrix} \qquad 3.41$$

which contains 15 unknown elements. The Mueller matrix is normalized to m_{11} because most measurements do not measure absolute transmission of the sample.

The values of each of the optical elements are meaningful when correlated to the physical properties of a sample, for example its optical isotropy. To measure certain elements, one may put the PSG and the PSA at certain known angular positions to reduce

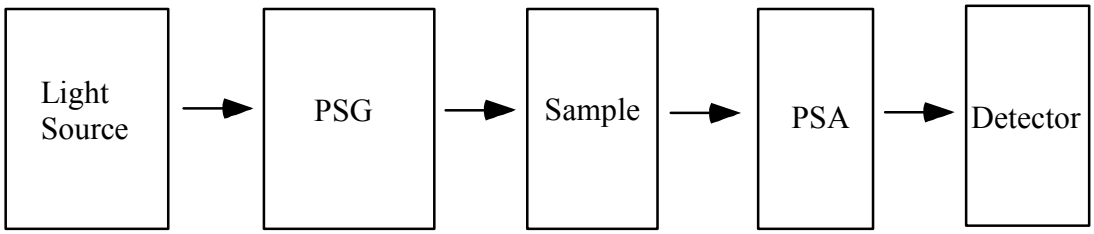


Figure 3.8 Polarimetery experiment design

the number of non-zero elements. For example, in measuring the properties for linear birefringence of a birefringent sample oriented at angle θ, only elements m_{32} and m_{34} need to be measured; so the PSG and PSA are set-up at certain angular positions with respect to a reference in order to eliminate all other elements from the $\mathbf{M}_S$

Using the configuration in figure 3.7 along with equations 3.30 and 3.37, the intensity of light measured by the detector is given by [28]

$$I(t) = \begin{pmatrix} 1 & C_{p1} & S_{p1} & 0 \end{pmatrix} \mathbf{M} \begin{pmatrix} 1 \\ C_m C_b + S_m S_b Y_\delta \\ S_m C_b - C_m S_b Y_\delta \\ S_b X_\delta \end{pmatrix} \tag{3.42}$$

where $C_{p1} = \cos(2\theta_{p1})$, $S_{p1} = \sin(2\theta_{p1})$, and $\theta_{p1} = \theta_a - \theta_m$, **M** is the Stokes vector for the elements between the PSG and PSA given in the general form in equation 3.41.

Multiplying the matrices yields

$$I(t) = I_{dc} + I_X X_\delta + I_Y Y_\delta = I_{dc} + (I_X - \delta_o I_Y) X(t) + (I_Y + \delta_o I_X) Y(t) \tag{3.43}$$

The parameters contributing to the intensity are the basis function $X(t)$, $Y(t)$ (equations 3.35 and 3.36), I_{dc}, I_X, and I_Y, the last three parameters are given by

$$\begin{aligned} I_{dc} &= 1 + C_{p1} m_{21} + S_{p1} m_{31} + C_b \{ C_m (m_{12} + C_{p1} m_{22} + S_{p1} m_{32}) \\ &+ S_m (m_{13} + C_{p1} m_{23} + S_{p1} m_{33}) \} \end{aligned} \tag{3.44}$$

$$I_X = S_b (m_{14} + C_{p1} m_{24} + S_{p1} m_{34}) \tag{3.45}$$

$$I_Y = S_b \{ -C_m (m_{13} + C_{p1} m_{23} + S_{p1} m_{33}) + S_m (m_{12} + C_{p1} m_{22} + S_{p1} m_{32}) \} \tag{3.46}$$

The above expressions require the Stokes vector for the sample be specified in order to obtain the full expression for the intensity on the detector.

3.5 Concluding remarks

Using two parallel-plates as a rotational rheometer operated at thin gap between the plates allows achieving high shear rates without generating problems usually associated with typical rheometerical designs for such high shear-rate measurements. The magnetic hard disk drive system allows such design to be possible. The idea of building an instrument capable of studying the rheological and structural properties of polymeric liquids at high shear-rate range is achievable through combining the design for a high-shear, two parallel-plate rotational rheometer in a hard disk drive configuration and optical techniques such as birefringence. This allows a complete study of the flow process at high shear rate in polymeric liquids.

CHAPTER 4
EXPERIMENTAL SETUP

4.1 Literature review

Rheometry research for studying systems under high shear rate has been investigated by different groups. This section is a review of the use of two parallel-plates rheometers in attempts to achieve high shear rates. The second part of the review represents a brief look at the use of birefringence measurements in rheometry.

4.1.1 High-shear-rate rheometry

Measurements at high shear rate have been a subject of study by different groups. The parallel-plates rotational rheometer as discussed in chapter 3 is suitable for high shear rate measurements. Binding and Walters [29] used two plates having the same diameter with a thin film of 3.2 μm. and were able to reach shear rates as high as 10^5 s^{-1}. Connelly and Greener [22] modified a conventional parallel-disks rotational rheometer capable of reaching high shear rates of 10^5 s^{-1} by using a thin film between the two plates. In their design, the gap between the plates was kept at about 50 μm. They used in their experiment a thixotropic loop (T-loop) in which the shear rate is ramped at a given rate from some starting value to a maximum value, and then it is ramped down from the maximum value to the minimum starting value. The T-loop is useful in detecting the presence of disturbances in conventional two-plates rotational rheometry such as viscous heating, radial immigration, and surface fracture. Using the T-loop procedure, the effects of such disturbances were easily detected and separated from the actual rheological responses.

The use of the magnetic hard-disk-based designs for studying tribology of the magnetic disk has been well established. Recently [23,24], some groups have used a rotational rheometer to measure the viscosity of different lubricants films at high shear rates based on that design. A common way of using such a design involves measuring the thickness of the film between the plates using techniques such as ellipsometry or

electron spectroscopy for chemical analysis, but the thickness was not measured in situ [23], that is during shear. This might make the measured rheological properties questionable since the thickness could change with normal pressure and sliding speed. Jonsson and Bhushan [24] claimed to have reached a shear rate approaching 10^7 s^{-1}. In their design, they developed a capacitance technique in order to monitor the thickness in situ, but they used the thickness measured by ellipsometry in their calculations for shear rate and viscosity.

4.1.2 Measurement of polymer birefringence

Birefringence has been used in research in concerning polymeric liquids subject to flow for long time [30,31]. Birefringence at first was used in steady-state flows, but then, using the advancements in the optical polarization techniques [32], it has been used to study time-dependent flow fields. Janeschitz-Kriegl [11] and Wales [12] present comprehensive reviews of the use of birefringence in studying polymeric materials. The basic technique employed a sample sandwiched between two crossed polarizers. When the sample is in flow, the signal passing through the polarizers due to the birefringence developed in the sample is measured. The retardation and orientation can be studied and related to the mechanical responses of the sample. Such a set-up requires mechanical rotation of the optical elements and the sample to obtain enough information on the sample. This limited the use of the technique to steady-state flow.

Kemp [27] introduced a technique in which the modulation of the polarization of light at fixed frequency is used. This method is based on the photoelastic effect. Different experimental arrangements were used in studying polymeric liquids with this technique. The most common set-up uses a polarizer and photoelastic modulator as the polarization state generator and analyzes the elliptically polarized light using an analyzer and then processes the signal with a lock-in amplifier. Such a technique allows measurement of birefringence in the sample at low and high levels [8,33-34]. Measurements of flow birefringence in time-dependent flow, such as the start up and a sudden cessation of steady state shear flow, were introduced first using a conventional technique [8,36], with a sample sandwiched between two polarizers. In this case, the

determination of birefringence and orientation requires physical rotation of the polarizers at two different positions. This may introduce difficulties in the measurements due to possible small shifts of the spatial point of measurements and also the zero matching of the start time for each run. One solution for such problems was introduced through a technique which uses a two-color laser [19]. In this experiment, a single measurement is sufficient for getting enough information on the sample since two different polarized beams labeled with the two colors pass through the sample simultaneously. Analyzing the two beams allows one to obtain the birefringence and orientation at the same time.

The above-cited experiments for high-shear-rate measurements were performed without any attempt to introduce birefringence measurements or optical measurements within the experiments, and the above-cited birefringence experiments were limited to small to moderate shear rate ranges. Simultaneous measurements of rheological properties and structural properties at high shear rate have not previously been reported. The following sections describe the experimental set up for an experiment to measure both rheological and structural properties of complex fluids from high to extremely high shear rates within one experiment.

4.2 Rheometer

The concept of rheometer design using two parallel-surfaces is based on generating a simple shear between the two surfaces. Fixing one of the plates and moving the other at constant velocity generates the simple shear. Details of the design of the rheometer to generate simple shear at high shear rate are discussed in this section.

4.2.1 Shearing disk

In this design, the disk is one of the two plates forming the shearing surfaces. It is a crucial part, and its design is important. The disk used in this instrument is made of float glass with 100 mm diameter and 6.35 mm thickness with a 25.4 mm diameter hole (figure 4.1) manufactured by Optical Components Inc. Inadequate surface quality can limit the ultimately performance of the part. High surface quality reduces scattered light and eliminates unwanted diffraction patterns. The surfaces of the disk used in this

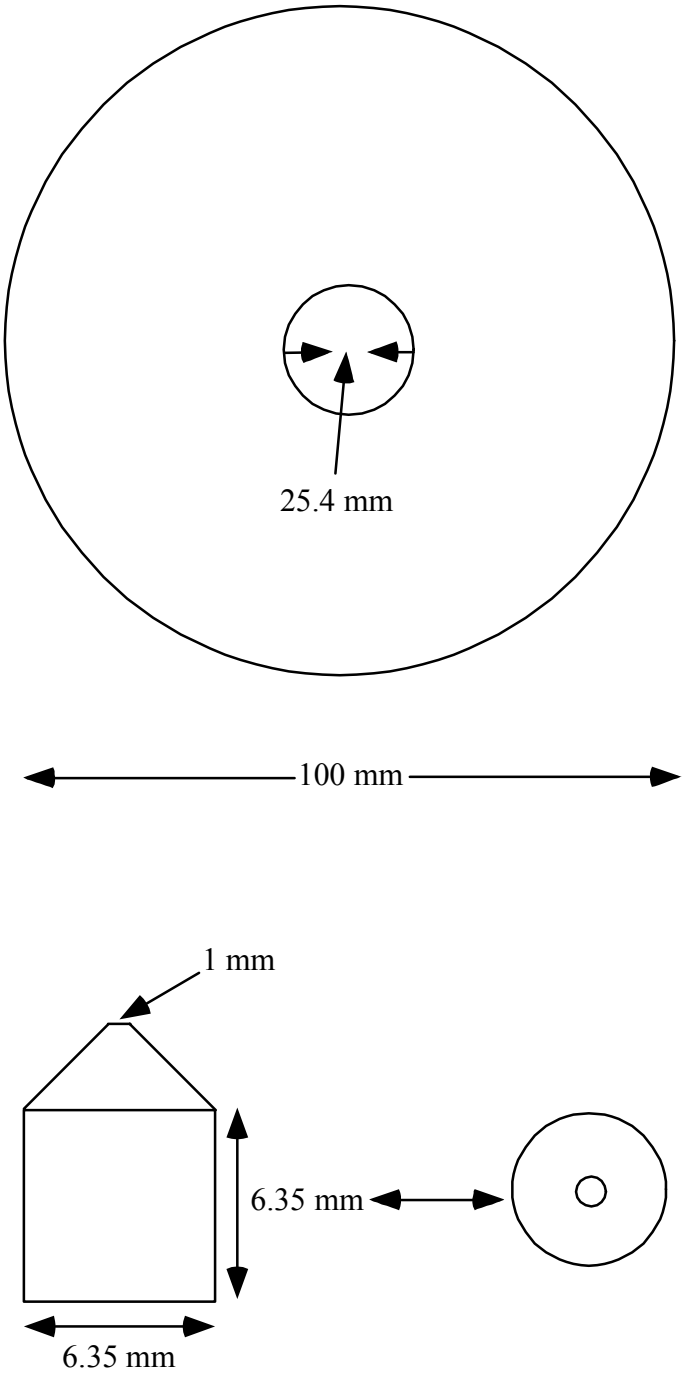


Figure 4.1 The disk and slider

instrument have surface roughness of 3 nm RMS or better, as required to achieve thinner films on the surface, and has parallelism of 5 arc sec. The surface irregularity is λ/5 - λ/20 with 10-5 Scratch-Dig (scratch-dig is a rating which measures the visibility of the surface defects such as scratches and dips). The surface is coated with a 500 Å thick layer of electrically conductive indium tin oxide (ITO) which allows > 85% of normal incident light to pass through the disk.

4.2.2 Slider

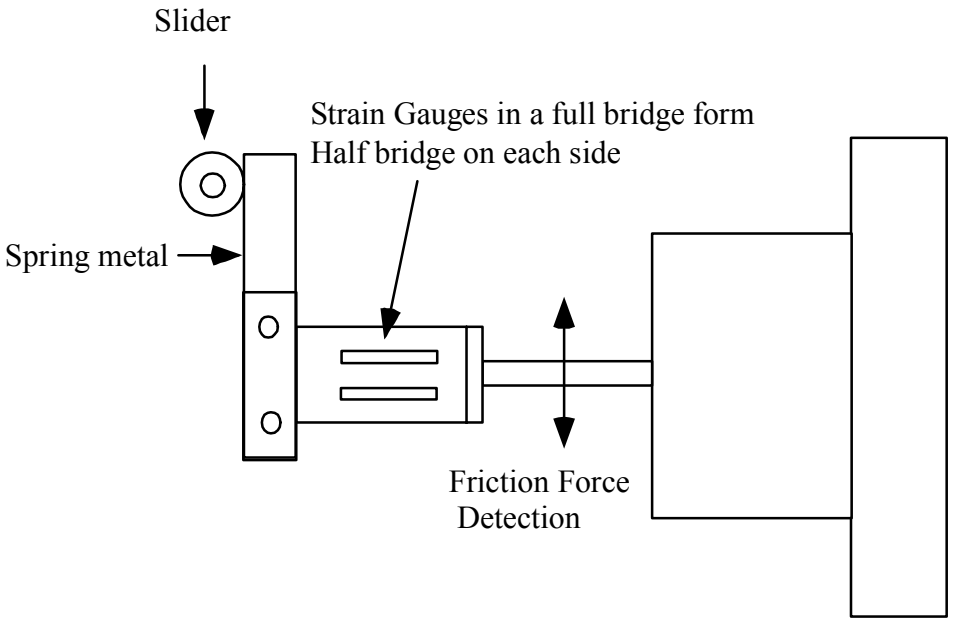
The slider is made of float glass in a cone prism shape as shown in figure 4.1 . The cylindrical portion is 6.35 mm diameter and 6.35 mm height. The cone shaped portion has its apex truncated with 1 mm diameter and 3.18 mm height. Both top and bottom surfaces of the slider have similar flatness of λ/5 - λ/10. Only the truncated apex surface is coated with a 500 Å ITO layer.

4.2.3 Slider arm

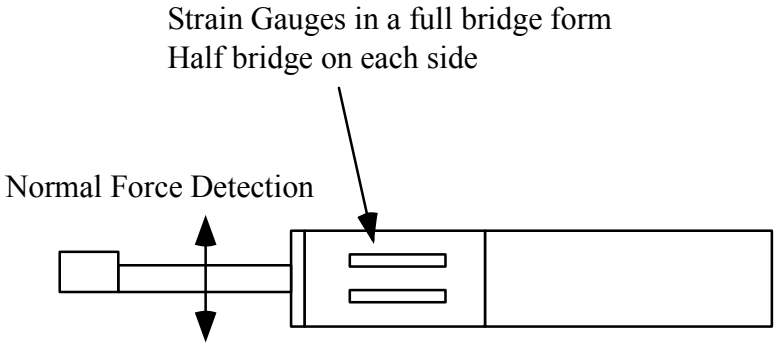
The slider is supported by an instrumented, dual-cantilever slider arm with I beam shape made of aluminum and a stainless steel spring as in figure 4.2. With this support the slider acts as a floating plate over the disk in order to achieve thinner films and at the same time allows the slider to follow the surface topographic variations within the film due to any irregularity during motion. Since the change in deflection of the spring due to these variations is small, the spring exerts a nearly constant normal force. The slider is equipped with strain-gauges for the force measurements, and the dual-cantilever form allows both normal and friction force transducers to be installed on the same beam with minimal interaction. The slider arm sits on a triaxial stage with its vertical-motion micrometer (AD-30, Newport) motorized by a μ-drive controller (ESA-CSA, Newport). The whole stage sits on a bench, which allows the stage to be moved off the disk.

4.2.4 Supporting system

The disk sits on a balance table with fine and coarse screws used to adjust and level the disk. The top side of the table is covered with an electrically insulating Teflon



Top view



Side view

Figure 4.2 Strain gauges structure and strain gauges arm

piece that supports the disk. The bottom side of the balance table sits on a shaft connected to the high precision spindle. The top of the disk is fixed by another Teflon piece, which also serves as a holder for a mercury cup that provides an electrical connection from the ITO on the disk surface. Figure 4.3 shows the disk-slider assembly. The whole apparatus is mounted on an optical table with an air suspension to reduce vibration.

4.3 Drive system

The drive system rotates one of the plates with respect to the other plate to generate shear; a wide range of speeds, stability, and low vibration are required. The drive system is illustrated in figure 4.4. The driving motor is a pancake ServoDisc (S9M4HI, KILLMORGEN) with 187 watts output power, with controls allowing both automatic and manual operation. The ServoDisc has unique advantages such as absolute zero cogging for ultra smooth velocity, operation over wide speed range, low mass armature for high acceleration and deceleration, low electrical noise, and compact size.

The other part of the drive system is the high precision spindle, which sits below a small platform, which supports the triaxial stage for the slider arm and other instrument components. The spindle has a high quality bearing system with very low radial run out, high stability and low vibration. One side of the spindle is attached to an encoder using three-beam flexible coupling for measuring the angular position and rotational speed with no backlash and constant velocity.

Motion is transferred between the motor and the spindle by a system of belts and pulleys through a gearing system with high precision shafts and ball bearings (Browning Standard). This gearing system allows motion transfer without vibrations from the motor.

4.4 Detection system

The quantities measured in the shear experiment are the shearing forces, the applied normal forces, the rotational velocity, and the thickness of the films. These quantities have to be measured accurately and simultaneously.

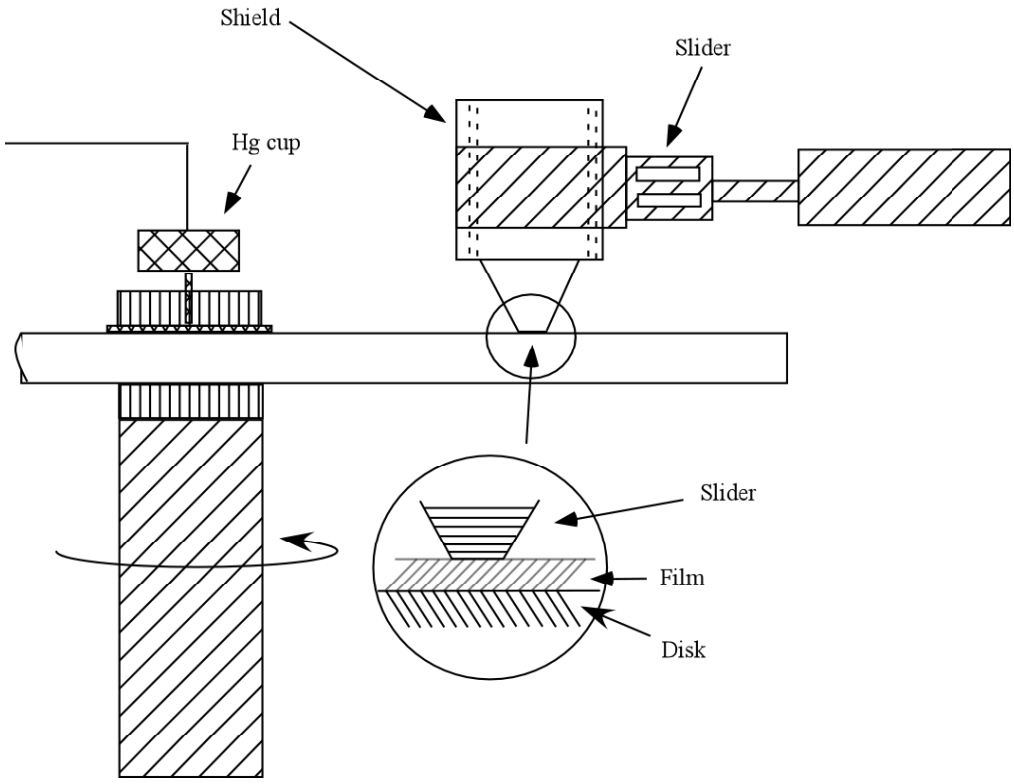


Figure 4.3 Schematic of disk-slider assembly

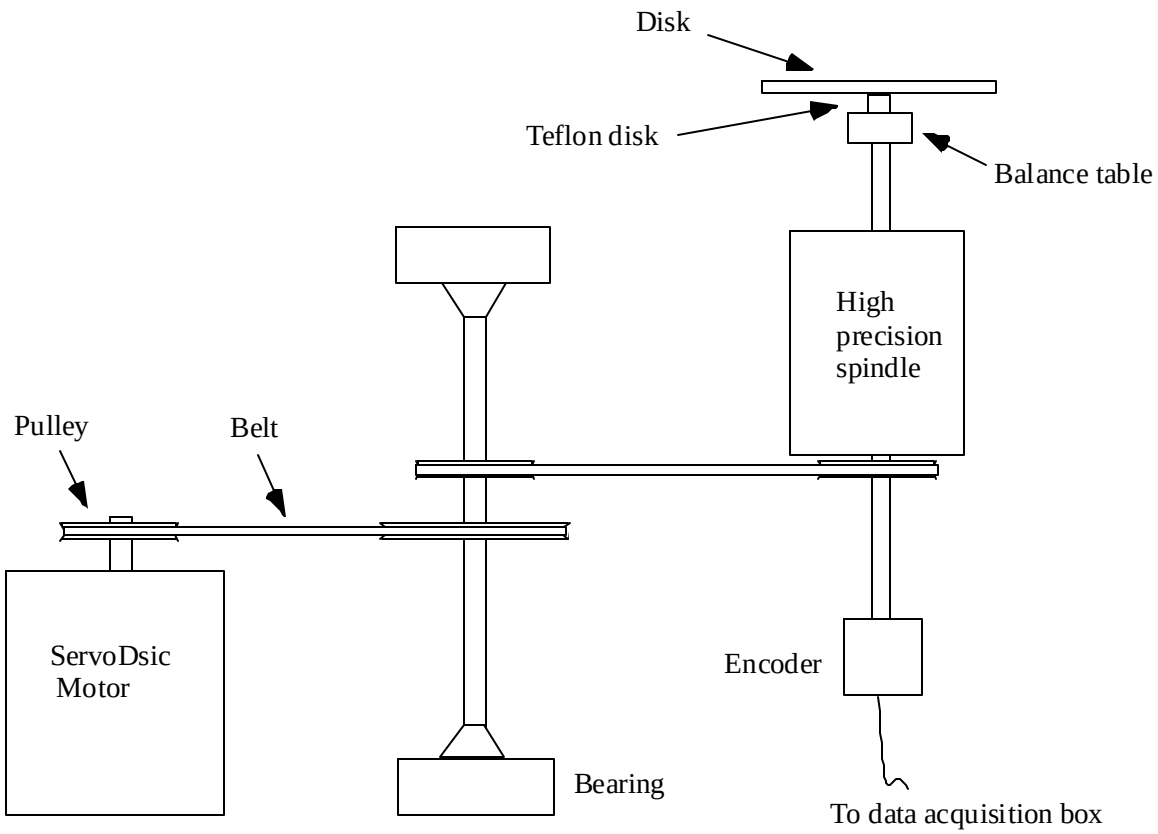


Figure 4.4 Drive and support system

4.4.1 Force measurements

Measuring the shearing force is the primary measurements. As shown in chapter 3, equation 3.11, the shear force is required to calculate the shear stress and the viscosity. A sensitive detection system is crucial in order to measure small shearing forces. The detection system is based on strain gauges which measure the strain in the slider arm**.**
Four strain gauges (N2A-13-S061P-350/E6, Vishay Measurements Group, Inc.) in full bridge design were installed with each half of the bridge on opposite faces of the vertical and horizontal portions of the dual-cantilever slider arm. The bridge for normal force measurement is on the top and bottom surfaces of the beam, and the bridge for friction force measurement is on front side and backside of the beam as in figure 4.2. This design allows measurements of small forces as well as large forces. For each bridge, an excitation voltage is applied to activate the bridge, and the resultant signal is detected through a signal-conditioning amplifier.

4.4.2 Rotational speed measurement

In order to calculate the shear rate, the relative velocity of the shearing surfaces must be measured and monitored. The velocity is determined by measuring the rotational velocity with an encoder attached to the high precision spindle, as in figure 4.4, through a rubber mount to isolate vibrations. The encoder (Dynapar brand, model E2310001948, Danaher) is a high resolution, optical incremental encoder with 1000 pulses per revolution, low noise, and high performance. It is attached to a data acquisition box connected to the computer for measuring the rotational speed and angular position.

4.4.3 Capacitance measurement

Calculating the shear rate requires knowing the liquid thickness between the two plates. The present design allows measuring the capacitance between the two plates in order to monitor and measure the thickness in situ. Both disk and slider are coated with conductive layer of ITO which serve as the two conducting plates of a capacitor. The slider has a shielding system made of two concentric copper cylinders insulated from each other with Teflon. The inside cylinder contacts the ITO layer on the slider

establishing a electrical connection with that side of the capacitor, and the outside cylinder is grounded.

The ITO on the disk side of the capacitor is connected through a copper ring at its center, which is also in contact with a mercury (Hg) cup. The cup serves as a contact between the disk and the outside through a pin dipped into the mercury to reduce mechanical and electrical noise.

The capacitance is measured through four shielded coaxial cables, two connected to each side of the capacitor with one for the drive signal and the other for sensing the signal; these coaxial cables are connected to a capacitance meter. A capacitance meter (SR715 LCR Meter, SRS) has 100 Hz to 10 kHz test frequency range and measures the capacitance with a range 10^{-4} pF to 0.99 F with accuracy between 1% to 5%.

4.5 Birefringence

The birefringence set up is based on a polarization state generator (PSG) made of a polarizer and a photoelastic modulator (PEM) in addition to a polarizer as a polarization state analyzer (PSA) as discussed in chapter 3. The optical train consists of a HeNe laser as light source, a PSG, a sample, PSA and photodetector as in figure 4.5 [8, 28, 37, 38]. This section presents the details of the optical train and the different elements used in building the birefringence experimental set up.

4.5.1 Laser source

An ultra stable HeNe laser (model 200, Laboratory for Science) with 4 mWatt output at 632 nm wavelength was used as a light source providing high output intensity and a well-collimated Gaussian beam.

4.5.2 Linear polarizer

Light emerging from the source passes through a linear polarizer. A perfectly linear polarizer assumed in chapter 3. A calcite linear polarizer with extinction ratio of 10^5 was used. The polarizer is oriented at $\pm 45^o$ with respect to a reference; this simplifies

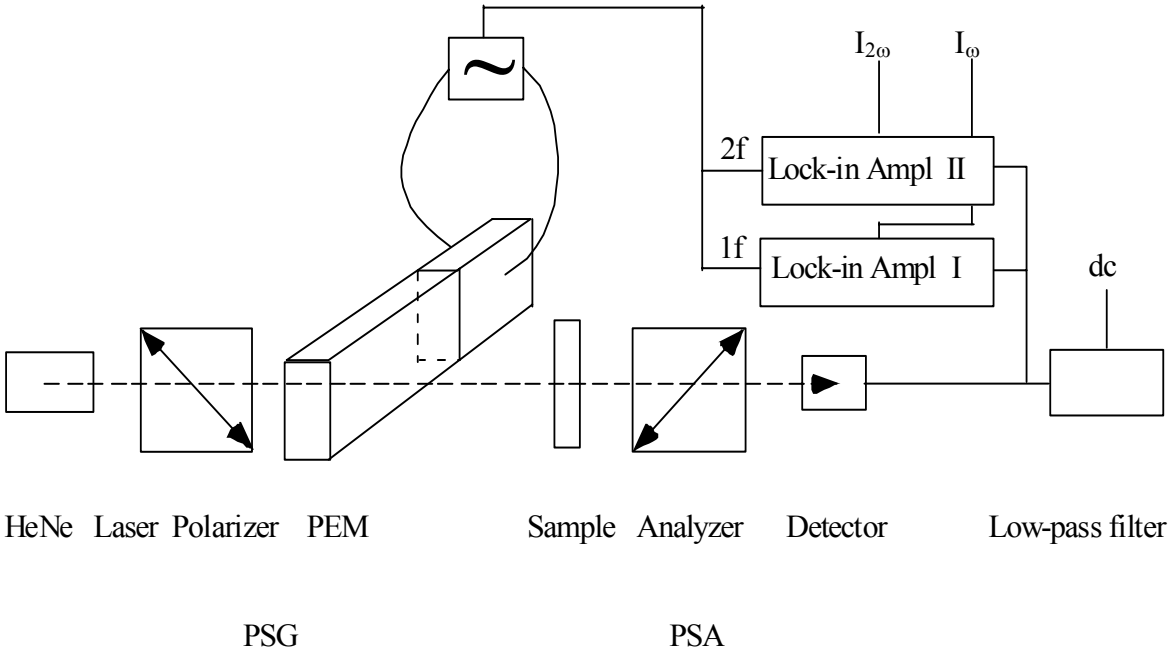


Figure 4.5 Optical system elements with orientation

the Stokes vector for the polarization state generator and to gives the maximum intensity of light emerging from the polarizer.

4.5.3 Photoelastic modulator (PEM)

The photoelastic modulator (PEM) is an instrument used for modulating or varying the polarization of a beam of light at a fixed frequency. The principle of operation is based on the photoelastic effect, in which a mechanically stressed optical element exhibits birefringence; it is stressed at a fixed frequency to vary polarization at that frequency.

The PEM used in the present set up is PEM-90 (model I/FS50) made by Hinds Instruments, Inc. The PEM is a rectangular piece of fused silica that is bonded to a quartz piezoelectric transducer. By applying ac voltage with certain frequency to the transducer, an oscillating birefringence occurs at this frequency (as in figure 3.6). The frequency used is 50 kHz. The amplitude of the birefringence is controlled electronically with the PEM-90 controller.

The linear polarizer and the PEM form a PSG in which the PEM is oriented at 0^o with respect to a reference and the polarizer is oriented at $\pm 45^o$ with respect to the PEM (section 3.4.4 and equation 3.38). Light passing through the polarizer-PEM oscillates between the left and right circularly polarized light, with elliptically polarized light between these extremes as in (see figure 3.7). The optical oscillation frequency is at the modulator frequency. This light is incident on the sample.

4.5.4 Analyzing polarizer

A calcite linear polarizer is used as a polarization state analyzer (PSA) to analyze the light emerging from the sample before it strikes the photodetector. The linear polarizer has the same properties as the polarizer used in the PSG. The PSA is oriented at $\pm 45^o$ with respect to the PEM to simplify the analysis (section 3.4.4, equation 3.40)

4.5.5 Stokes vector of the sample

The general form of the Mueller matrix of the sample is given in equation 3.41. For a sample with retardance δ and orientationχ, the Mueller matrix is given as

$$\mathbf{M}_S = \begin{pmatrix} 1 & 0 & 0 & 0 \\ 0 & \cos^2(2\chi)+\sin^2(2\chi)\cos(\delta) & \sin(2\chi)\cos(2\chi)[1-\cos(\delta)] & -\sin(2\chi)\sin(\delta) \\ 0 & \sin(2\chi)\cos(2\chi)[1-\cos(\delta)] & \sin^2(2\chi)+\cos^2(2\chi)\cos(\delta) & \cos(2\chi)\sin(\delta) \\ 0 & \sin(2\chi)\sin(\delta) & -\cos(2\chi)\sin(\delta) & \cos(\delta) \end{pmatrix} \quad 4.1$$

The general form of the intensity on the photodetector is given by equations 3.44 – 3.46. Using the PSG, the PSA orientations specified above, and the sample Mueller matrix given above, the basis functions I_X and I_Y given in equations 3.45 and 3.46 can be written as

$$I_X = \cos 2\chi \sin\delta \quad (4.2)$$

$$I_Y = \sin) 2\chi \cos\chi (1\text{-}\cos\delta \quad (4.3)$$

Measuring the coefficients of the basis functions can lead to knowledge of the sample retardation and orientation.

4.6 Electronics and control systems

The different elements in the rheometer require careful simultaneous control and data acquisition. Such coordination requires fast electronics for controls and measurements and powerful software to facilitate such control and data acquisition. This section will discuss the different electronics involved in controlling the system and measuring the signals from the instrument transducers. Figure 4.6 displays the data flow a block diagram of data control and collection.

4.6.1 Rheometer control system

A home built box contains an electronic circuit that controls the drive system in the rheometer. The circuit allows both manual and electronic control of the speed of the motor. The electronic control is through a circuit connected to a data acquisition box on a personal computer.

Each strain gauge bridge is excited and sensed through a signal conditioning amplifier (model 2311, Vishay Measurements Group, Inc.). The amplifier allows varying the excitation voltage, filtering the signals, balancing the bridge, and adjusting the gain.

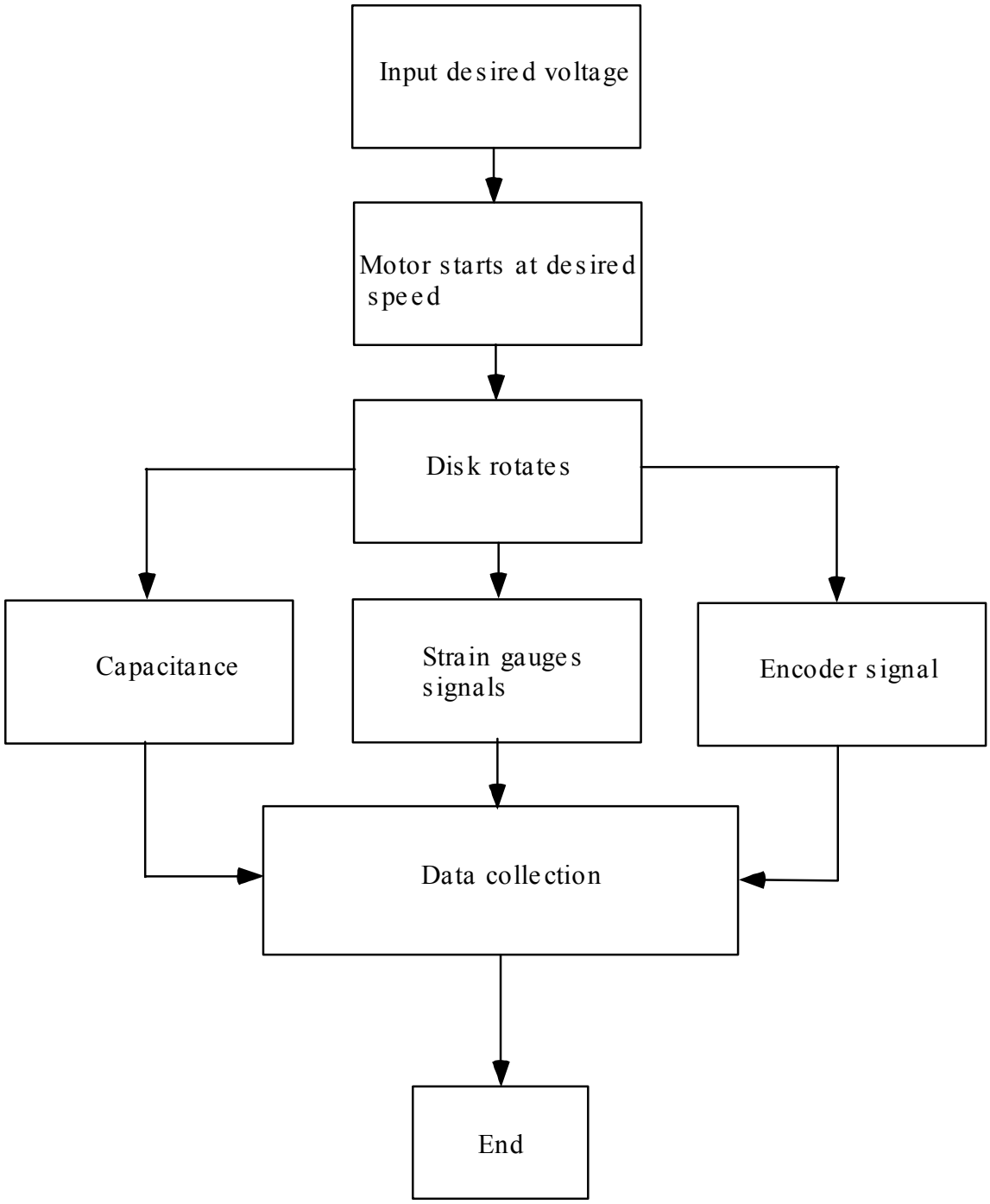


Figure 4.6 Data control and collection for the rheometer

Each amplifier is connected to a voltmeter (model 199 DMM/Scanner, Keithley) for monitoring the output signal and a data acquisition box (SCB-68, National Instruments) for collecting the data to the computer.

The capacitance meter (SR715 LCR Meter, SRS) has 100 Hz to 10 kHz test frequency range and capacitance range 10^{-4} pF to 0.99 F with accuracy between 1% to 5%. The meter is connected directly to the computer using a GPIB card that allows measurement and control by the computer.

The measurements are started through triggering the system by the computer. The computer applies a certain voltage to the motor control box which starts the motor. The motor drives the high precision spindle, which has an encoder at its bottom. The computer senses the encoder signal through the data acquisition box, which is connected through a high-speed data acquisition card. The shear stress due to rotation of the disk is transmitted through the sample film to the slider and alters the balance of each of the strain gauges bridges, which measure both the normal force and friction force. The change is sensed as change in the voltage of the bridge in the signal conditioning amplifiers, and each of the signals is transferred to the computer through the data acquisition box. The computer records the angular position, the rotational speed, the time, the friction force, the normal force, and the capacitance.

The above simultaneous control and data acquisition system requires powerful software able to coordinate the different processes. A data acquisition system based on Labview™ (National Instruments) was built and used for the experiment.

4.6.2 Birefringence control system: Waveform analysis

The intensity on the photodetector has the form given in equation 3.43. All measured quantities are contained in that equation. But equation 3.43 is given in terms of the basis functions X and Y given in equations 3.35 and 3.36. Rewriting equation 3.43 in terms of the expanded form of the basis functions gives [28]

$$\begin{aligned} \mathrm{I(t)} = \mathrm{I_{dc}} &+ (\mathrm{I_Y} + \delta_o \mathrm{I_X}) J_0(\mathrm{A}) + 2(\mathrm{I_X} - \delta_o \mathrm{I_Y})[J_1(\mathrm{A})\sin(\omega t) + J_3(\mathrm{A})\sin(3\omega t) + ...] \\ &+ 2(\mathrm{I_Y} + \delta_o \mathrm{I_X})[J_2(\mathrm{A})\sin(2\omega t) + J_4(\mathrm{A})\sin(4\omega t) + ...] \end{aligned} \quad (4.4)$$

The equation for intensity contains an infinite number of terms, but enough information concerning the sample is available in the first and second harmonics. Thus, rewriting equation 4.4 keeping only the first and second harmonic from the expansion yields expression for the signal intensities

$$I(t) = I_{dc} + (I_Y + \delta_o I_X)J_0(A) + 2(I_X - \delta_o I_Y)J_1(A)\sin(\omega t) + 2(I_Y + \delta_o I_X)J_2(A)\sin(2\omega t) \tag{4.5}$$

The total intensity has a dc component, $I_{dc} + (I_Y + \delta_o I_X)J_0(A)$, a first harmonic component, $2(I_X - \delta_o I_Y)J_1(A)$, and a second harmonic component, $2(I_Y + \delta_o I_X)J_2(A)$. A normalized intensity with respect to the dc component is

$$I = 1 + I_\omega \sin(\omega t) + I_{2\omega} \sin(2\omega t) \tag{4.6}$$

where the I_ω and $I_{2\omega}$ are the coefficients of the basis functions and defined as

$$I_\omega = \frac{2J_1(A)I_X}{(I_{dc} + J_o(A)I_Y)} \tag{4.7}$$

$$I_{2\omega} = \frac{2J_2(A)I_Y}{(I_{dc} + J_o(A)I_Y)} \tag{4.8}$$

A common way to analyze the intensity is by converting the intensity waveform into a voltage waveform. This can be done using a photodetector with a parallel resistor. A high-speed silicon detector (DET 110, THORLABS) with neutral density filter was used in the set-up. The voltage waveform can be characterized using a lock-in amplifier technique. The amplifier compares the signal of the detector with a reference signal from the PEM. The first harmonic signal I_ω (I_X component) and the second harmonic signal $I_{2\omega}$ (I_Y component) are measured using two separate lock-in amplifiers. The signals must be normalized by the dc signal, which is measured by a simple meter. An electronic phase shift can be adjusted using the phase adjustment on the lock-in amplifiers. The

signals can be simplified by eliminating the dependence on the coefficient I_Y. This can be done by setting the modulator amplitude at 2.4048 radians, giving $J_o(A) = 0$.

The birefringence set-up has different elements that require simultaneous coordination. The PEM is controlled to set the oscillation frequency (1f) and to set the voltage to the piezoelectric transducer so that the modulator amplitude is 2.4048. The PEM provides the reference frequencies 1f and 2f to the lock-in amplifiers. Two Stanford Research Systems lock-in amplifiers (model SR530) were used for measuring the first and second harmonics coefficients. A Keithley multimeter (model 199 DMM/Scanner) was used to monitor the dc signal, which was extracted using a low-pass filter. The dc, 1f, and 2f signals were recorded using a computer through a high-speed data acquisition card. Labview™ based software was used for controlling the data acquisition system and synchronizing the rheometer and birefringence computers. A block diagram of the control system is given in figure 4.7. Figure 4.8 illustrates the whole set-up for both the rheometer and birefringence.

4.7 Test samples

In the past decade, perfluoroethers (PFPEs), which constitute a special class of fluoropolymers, have attracted interest because of their unique properties [39-41]. Different families of PFPEs are produced [42]. These are Fomblin® (Ausimont, Italy), Krytox® (Du Pont, USA), Denmum® (Daikin, Japan), and Aflunox® (NOK, Japan). PFPEs can be homopolymers or copolymers and can be prepared using anionic open ring polymerization of tetrafluoroethylene in the presence of oxygen under UV to produce the branched polymer (PFPE-Y) or the linear polymer (PFPE-Z). The PFPEs can be prepared with non-reactive end groups $-CH_3$; an example is PFPE Y, or with functionalized end group with oxygen (such as –OH); an example of such compounds is he PFPE-Z-diol. In these experiments, Fomblin® YR of Ausimont has been used. The structure of Fomblin YR is

$$CF_3 - O - (\underset{\displaystyle CF_3}{\underset{|}{CF}} - CF_2 - O)_m - CF_2 - O)_n - CF_3$$

with m/n ~ 40/1. Some properties of Fomblin YR are given in table 4.1.

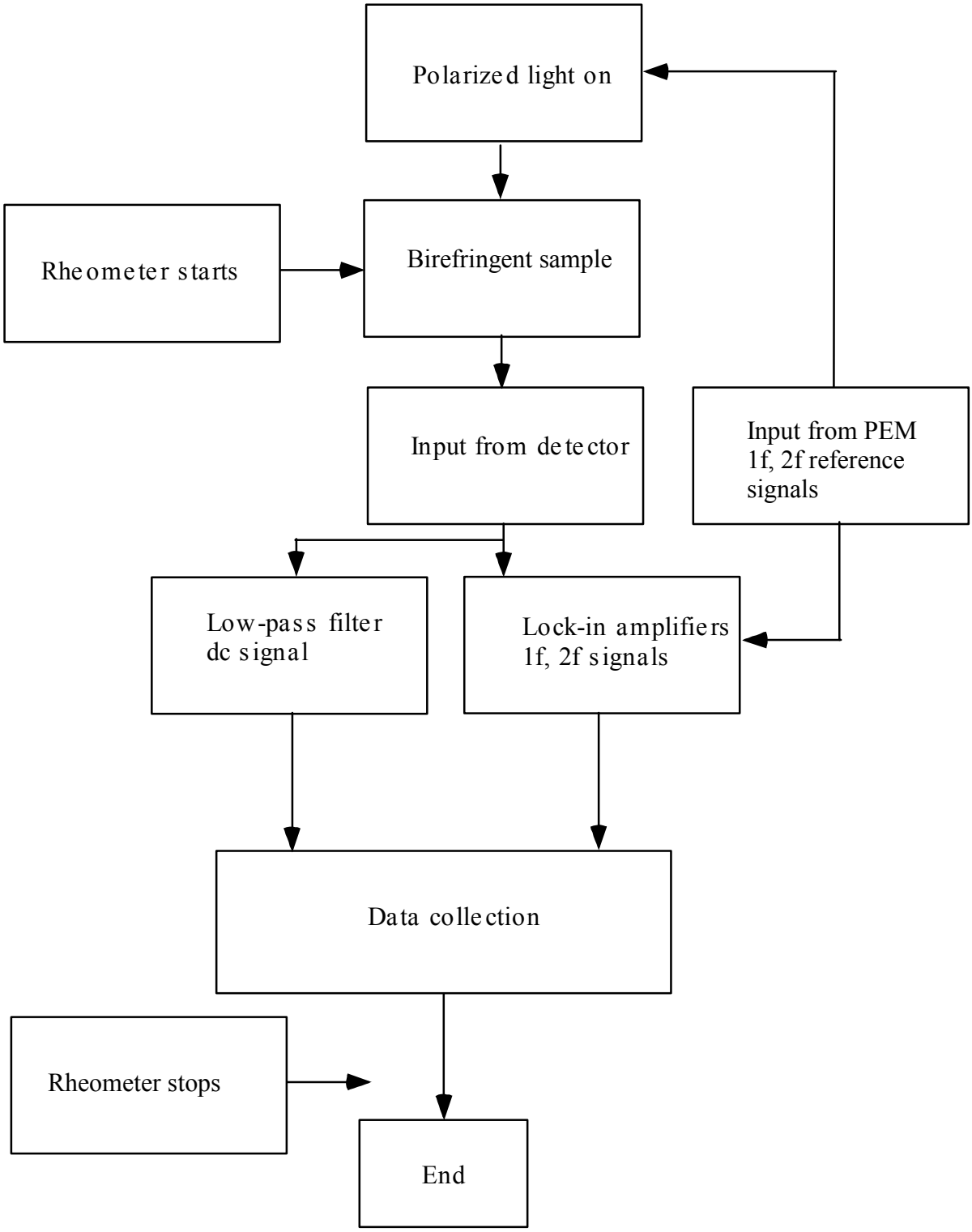


Figure 4.7 Data control and collection for the birefringence

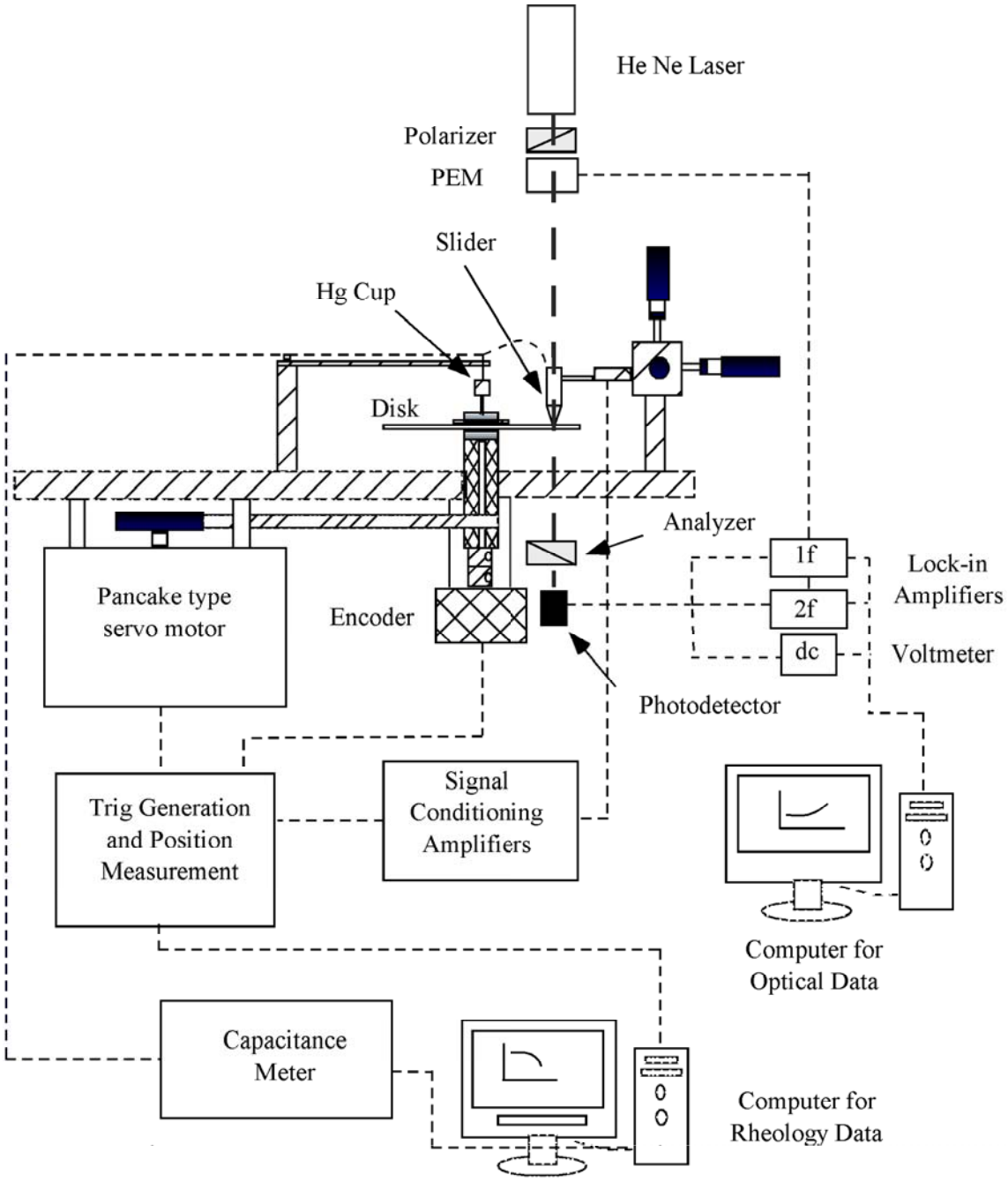


Figure 4.8 Schematic illustration of whole apparatus

Table 4.1. Properties of Fomblin YR

Molecular weight	Specific gravity (g/cm^3)	Viscosity (at 20 °C) reported (Pa.s)	Viscosity (at 25 °C) measured (Pa.s)
6,250	1.91	1.70	2.90

The PFPEs have been the subject of an intensive research effort. PFPE molecular weight, molecular weight distribution and molecular dimensions have been studied using small angle laser scattering [43], gel permeation chromatography (GPC) [44], and nuclear magnetic resonance (NMR) [45]. Their fractionation and solution properties were studied in two different solutions and correlated to their physical properties [46,47]. The pVT data of PFPEs and their relation to the flow of the PFPE were reported [48]. It was shown that the reduced equation of state of Flory, Orwoll, and Vrij is well suited for the description of the temperature and pressure dependence of the densities of PFPE compounds and is very helpful in discussing their flow behavior.

The PFPE compounds, due to their unique properties, have been used as lubricants for hard disk drive system [41]. Their use in that field has promoted an intensive research effort to study their flow properties, tribological properties [49], and correlation between their rheological and tribological properties [50,51]. The spread of PFPEs on different surfaces studied by infrared (IR) [52] spectroscopy, atomic force microscopy [53], and scanning polarization force microscopy (SPFM) [54] suggest that the chain conformation of PFPE liquids on surfaces is unlike bulk conformation, with polymer chains extended preferentially along the surface.

Different groups studied the rheological properties and their dependence on temperature and molecular weight. Kono etal.[50] studied the viscosity, storage modulus, and loss modulus of different PFPE melts with reactive end groups using a concentric cylinders rheometer at low and moderate shear rate ($\sim 10^3\ s^{-1}$). The viscosity

exhibited Newtonian behavior within the shear rate investigated and its dependence on molecular weight was found to have a transition at some critical molecular weight. The temperature dependence of the viscosity has an Arrhenius form ($\eta = \eta_o \exp(E_a/RT)$ where E_a is the activation energy. Ajroldi etal.[55], previous to the early report by Kono, reported the viscosity dependence of PFPEs on molecular weight at constant pressure and temperature and they found similar results. Side branching was found to cause microstructure due to the interactions between different reactive groups.

Viscosity for PFPEs with non-reactive end groups (Fomblin Y and Fomblin Z) for molecularly thin films have been investigated using the surface force apparatus [56,57]. The molecularly thin films have different lubricating behavior than the bulk films. Linear chains tend to align when subjected to shear, while side-branched molecules resist structuring and retain some fluid like properties. Shear stress was found to be decreasing with increasing number of molecular layers and approaching Newtonian flow when 7-10 layers are present.

PFPE compounds used as lubricant for hard disk drives helped in reducing the gap between the head and the disk. In such application, the disk rotates at speed of ~10 m/s, with a film thickness about 25 nm, the shear rate experienced by the lubricant film is of the order of 10^8 s^{-1}, this shows the importance of studying rheology at high shear rate. Cantow etal.[21] used a concentric cylinders type viscometer to study the viscosity of different PFPE compounds at high shear rate. They reported a viscosity transition from Newtonian to non-Newtonian behavior at high shear rate, but at the same time there was a temperature increase within the system of about 10 °C. Corrections were made for such temperature change, and zero shear (Newtonian) viscosity was reported to be 1.70 Pa.s for Fomblin YR and 0.23 Pa.s for Fomblin Z25. Streator etal.[23] investigated the rheology of different PFE compounds using a hard disk drive as a rheometer and reached shear rate up to 10^6 s^{-1}. The bulk viscosity was retained over the thickness they used (80 – 23 nm). Within the shear stress range 10^4 Pa$\leq \tau \leq 10^5$ Pa, shear-thinning behavior was experienced with each lubricant as in the previous study by Cantow [21]. Jonsson and Bhushan [24] used a rotational rheometer based on the magnetic hard disk design and investigated the rheological behavior of different PFPE compounds at high shear rates

while monitoring the thickness in situ. They reported shear-thinning behavior at shear rate order of 10^6 s^{-1}, while previous studies reported transition at lower shear rate.

4.8 Sample preparation

Samples were prepared by dissolving a certain percentage by weight of PFPE in a hydrofluoroether solvent, HFE-7100 ($C_4F_9OCH_3$, nanoafluoro-1-methoxybutanc, 3M Corp.). The solutions were filtered using 0.45 μm pore size syringe filter to remove any possible dust particles. The sample was applied over the disk using a spin coating technique. The thickness of the sample is determined by the solution concentration, spin coating speed, and duration of application. The solvent was evaporated during the spin coating and then the disk with sample film was kept over night over molecular sieves (pore size 5 Å).

The disk with the sample film is loaded on the instrument then balanced using the balance table while monitoring the capacitance and normal force. Data collection for both rheometer and birefringence are as listed in figures 4.6 and 4.7 respectively. After each experiment, the sample was washed off the disk by using the solvent (HFE-7100) while spinning the disk at high rpm.

CHAPTER 5
RESULTS AND DISCUSSION

The optical rheometer was designed and built in this work for measuring rheological and structural properties of complex fluids under high shear rate. Different calibration procedures for different elements of the rheometer were needed before using the rheometer to study the test samples. This chapter discusses different calibrations for the optical rheometer as well as the results on the test samples.

5.1 Calibration

5.1.1 Strain gauges

The strain gauges calibration was carried out by suspension of different masses using the slider arm and measuring the output voltage of the conditioning amplifier. The output voltage is plotted with the applied force in figure 5.1, at a bridge voltage of 5 V, gain of 1100, and filter of 100. The output is linear within 95% confidence. The estimated standard deviation of the force measurement is ±2.9%. The ultimate sensitivity is 241 μN.

5.1.2 Speed calibration

The computer applies voltage to the motor to achieve desired speed; this rotational speed is measured using an encoder. A calibration curve, to serve as a predictive tool for desired speed, was constructed (figure 5.2) by applying known voltage and measuring the speed. The speed was calibrated within an accuracy of 1.7%, but the ultimate accuracy depends on the accuracy in measuring the radial position of the slider over the disk.

5.1.3 Capacitance calibration

Capacitance between the disk and slider was measured to obtain and monitor the film thickness in situ. To compensate for inductance and capacitance of the cables in capacitance measurements, calibrations were performed with films of known thickness.

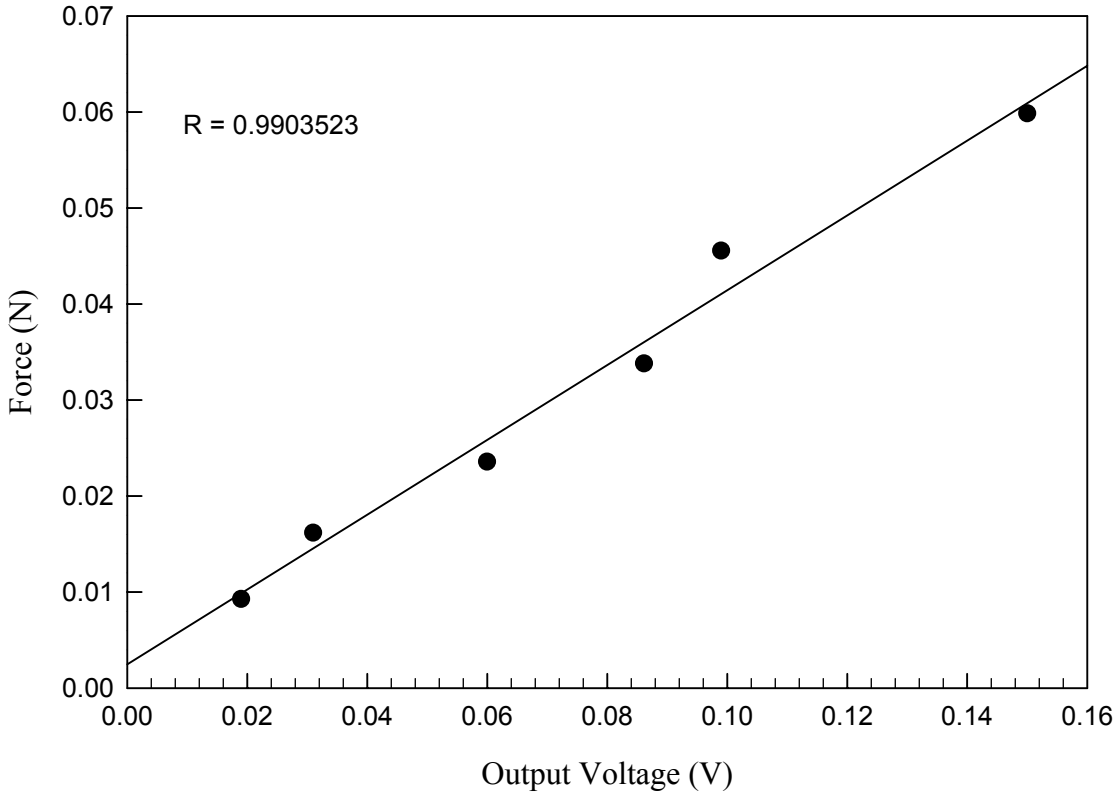


Figure 5.1 Output voltages of strain gauges versus applied force

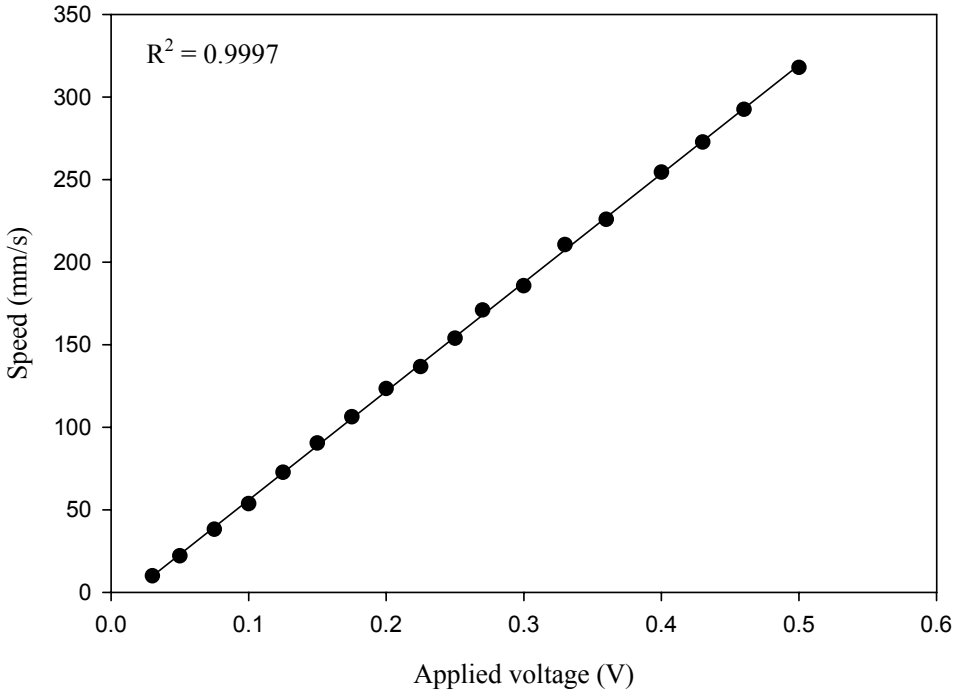


Figure 5.2 Speed calibrations

Polystyrene films were prepared by spin coating and their thickness was measured with a surface profiler and ellipsometer. A calibration curve was constructed as in figure 5.3. For the thicknesses measured in the experiment, with 0.1 V used as an oscillator voltage at 1 kHz frequency, a resolution of ± 9% of the measured value is observed [58].

5.1.4 Birefringence calibration

The birefringence apparatus required the following calibrations:

1) The azimuthal angle of the polarizer with respect to the PEM, θ_b.
2) The modulator static strain, δ_o.
3) The amplitude of the modulation, A.

The calibrations are performed occasionally since in this set up a single wavelength source has been used. Each calibration requires a specific arrangement of the optical train.

5.1.4.1 Determination of θ_b

The calibration of θ_b is made with a straight-through configuration [59] where there is no sample in place. The Mueller matrix for free space is

$$\mathbf{M} = \begin{pmatrix} 1 & 0 & 0 & 0 \\ 0 & 1 & 0 & 0 \\ 0 & 0 & 1 & 0 \\ 0 & 0 & 0 & 1 \end{pmatrix} \qquad 5.1$$

For such a configuration, the coefficient I_X (equation 3.45) is zero and the coefficient $I_Y = \sin(2\theta_b)$ (see equation 3.46). Setting the θ_b at 0^o or 90^o nulls this coefficient. Then, using the precision rotator, θ_b is set to $\pm 45^o$ with respect to the modulator. The accuracy of setting θ_b is primarily a function of the accuracy of the attached rotator, $\sim 0.05^o$ in this case.

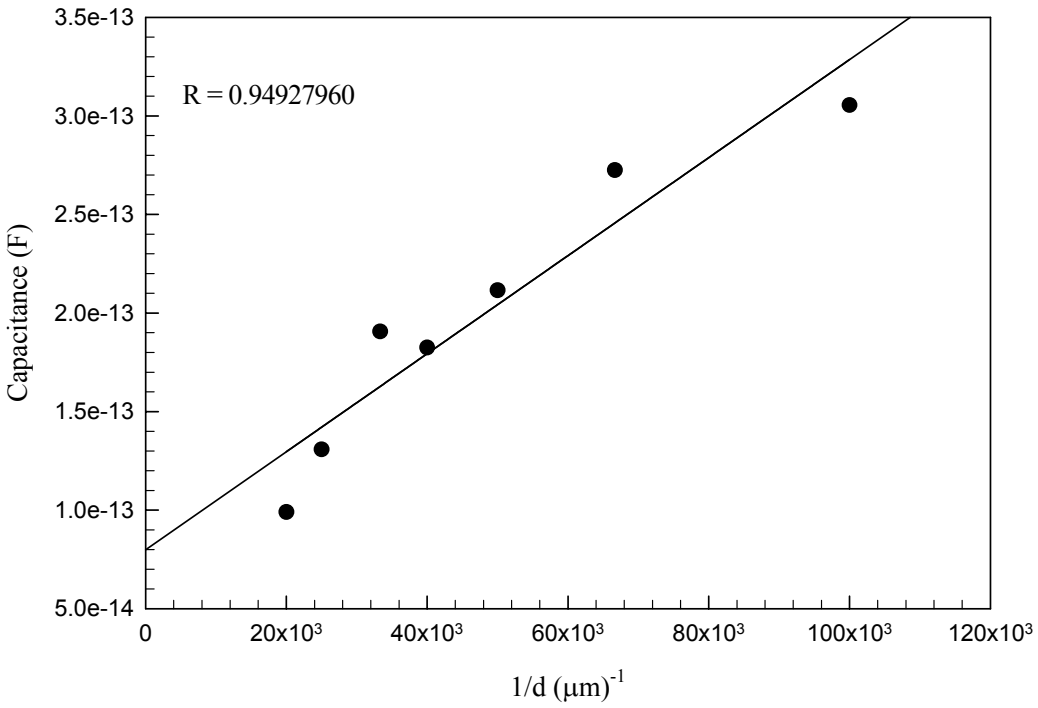


Figure 5.3 Capacitance calibration curve

5.1.4.2 Determination of δ_o

The static retardation of the PEM δ_o is dispersive and wavelength dependent [60]. In this setup, a single wavelength (λ = 632 nm) light source has been used, and the calibration is done at that wavelength. A straight-through configuration [61] has been used to determine the static retardation of the modulator, with $\theta_b = 45^o$. Then

$$I_\omega = \frac{J_1(A)\delta_o}{I_{dc}} \qquad 5.2$$

Measuring I_ω and I_{dc} and knowing $J_1(A)$ allows calculation of δ_o. The measured value of δ_o was found to be 0.004674 rad and can be ignored in the calculations.

5.1.4.3 Determination of A

To make the analysis of dynamical measurements simpler [28], it is beneficial to set $J_o(A)$ to zero, when $J_1(A) = 0.5191$ and $J_2(A) = 0.4317$. This can be accomplished by setting up the system in a straight-through configuration with the polarizer at 45^o and the analyzer at -45^o with respect to the PEM. The ratios I_ω, which is proportional to $J_1(A)$, and $I_{2\omega}$, which is proportional to $J_2(A)$, can be measured by mapping the modulator amplitude A. Figure 5.4 shows the modulator calibration. from the curve, the desired calibration set point where $J_0(A)$ is zero found to be when A = 2.4084, and both $J_1(A)$ and $J_2(A)$ are 0.5191 and 0.4317 respectively.

5.1.4.4 Determination of the normalization coefficients

The I_ω and $I_{2\omega}$, in equations 4.7 and 4.8 are proportional to I_X and I_Y, respectively, and the proportionality constant is known as the gain factor. Normalization [62,63] can be done by using a quarter wave plate ($\lambda/4$) to serve as a retarder with known retardation (retardance = $\pi/2$) where both harmonics I_ω and $I_{2\omega}$ are present. The maximum retardance for this occurs at $\pi/2$ radians. This has been accomplished by setting up the system in a data-collecting configuration, and rotating the quarter wave plate from 0^o to 90^o. Figure 5.5 shows data for I_ω and $I_{2\omega}$ before and after normalization.

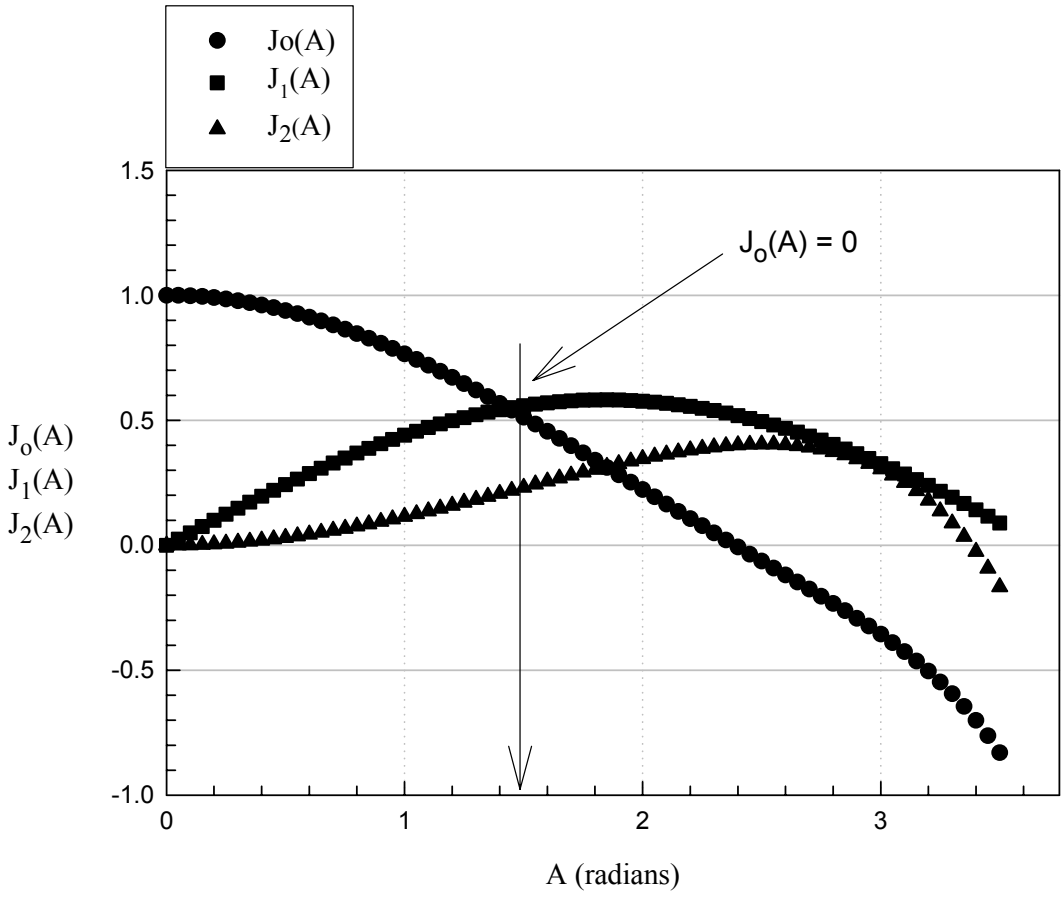


Figure 5.4 The Bessel function calibration curve for the PEM

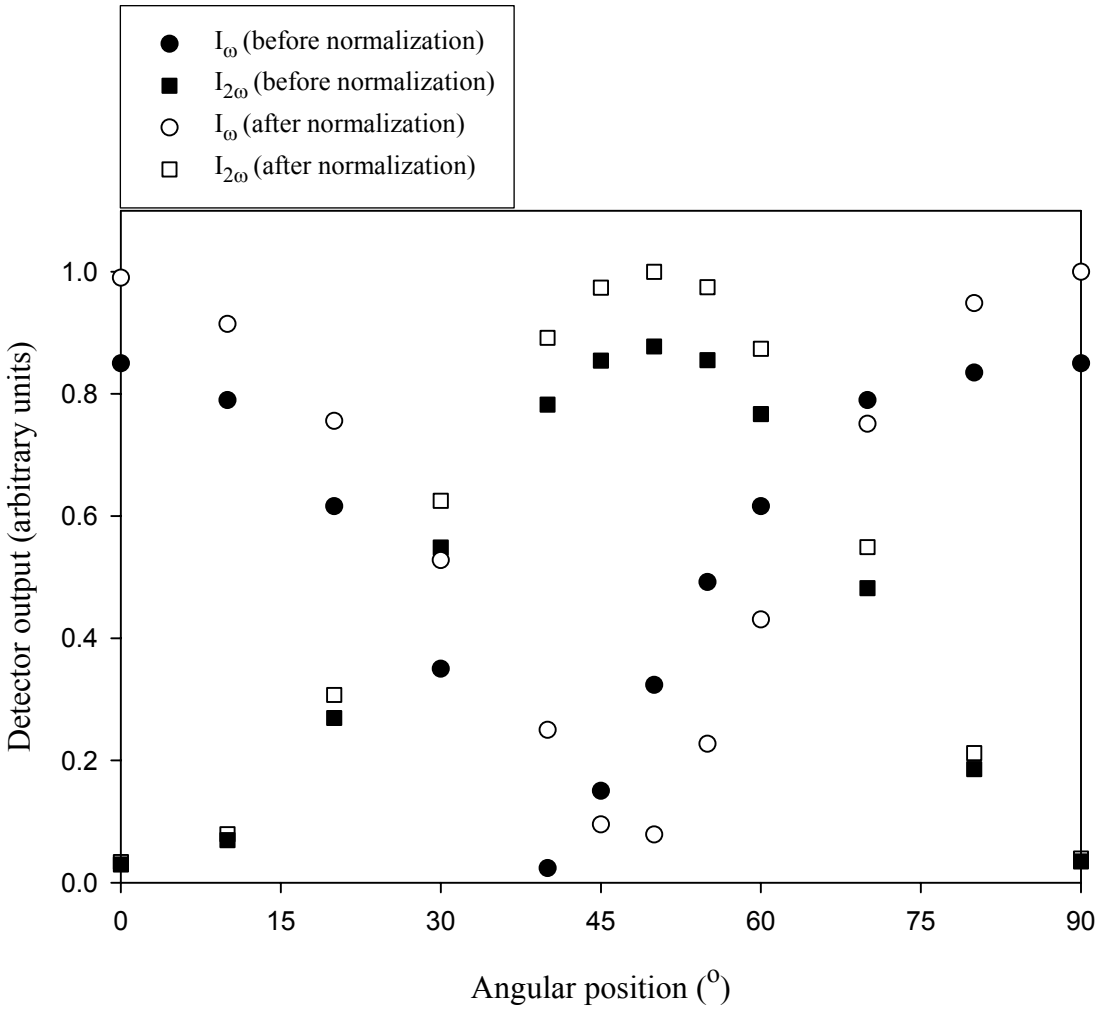


Figure 5.5 Normalization of the output signals

The experimentally observed deviations come from the electronics, cables, and time delays of the lock-in amplifiers.

5.1.4.5 Birefringence of quarter wave plate (QWP)

A well-known retardation device finds wide applications in the design of optical polarimeters. This is the quarter wave plate with a retardation $\delta' = \pi/2$. The Mueller matrix for a quarter wave plate oriented at angle θ is

$$\mathbf{M}_{\lambda/4}(\theta) = \begin{bmatrix} 1 & 0 & 0 & 0 \\ 0 & \cos^2 2\theta & \sin 2\theta \cos 2\theta & -\sin 2\theta \\ 0 & \sin 2\theta \cos 2\theta & \sin^2 2\theta & \cos 2\theta \\ 0 & \sin 2\theta & -\cos 2\theta & 0 \end{bmatrix} \qquad 5.3$$

Equations 3.45 and 3.46 give the parameters (I_X and I_Y) contributing to the signal on the detector.

$$I_X = \cos 2\theta \sin \delta \qquad 5.4$$

$$I_Y = (\sin 2\theta \cos 2\theta + \sin^2 2\theta)(1 - \cos \delta) \qquad 5.5$$

By rotating the quarter wave plate, the signals I_ω and $I_{2\omega}$ can be measured. The output is plotted in figure 5.6, and the typical retardation effect of a quarter wave plate is observed. The maximum retardation $\delta' = 1.51 \pm 0.07$ radians, and the minimum is 0.024 radians. The angular positions show some deviation of ~1.5° from the ideal case; this is due to the alignments and the tolerance of the precision of the different optical elements. This difference in the angular adjustment was taken in consideration in the experiment.

5.1.4.6 Windows effect

Both slider and disk were made from a non-birefringenet glass and both are coated with an indium tin oxide (ITO) layer. Testing showed that no such retardation was

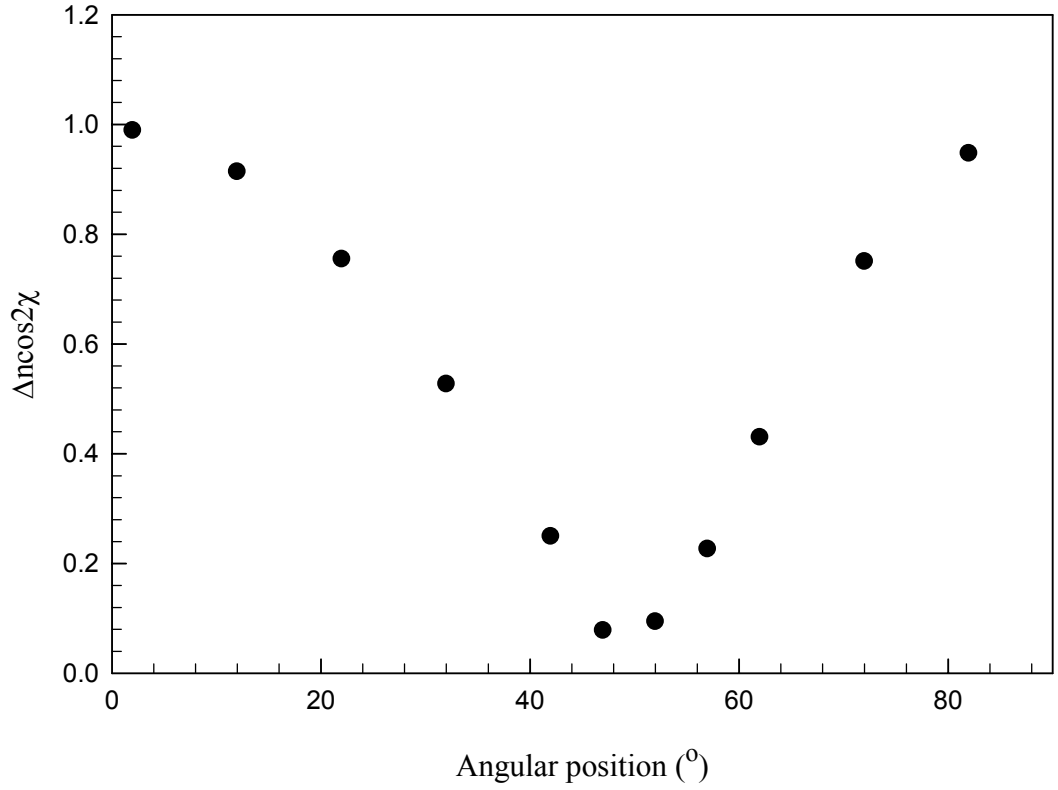


Figure 5.6 Quarter wave plate retardation

inherent in the disk but the slider showed a small amount due to parasitic conditions such as strain in the coating. A Soleil-Babinet optical compensator [8,10] has been used to null the parasitic birefringence developed within the slider. The compensator generates a known retardance and orientation angle. The compensator consists of two wedges of a birefringenet material sandwiched together as in figure 5.7. Variation of the retardation can be accomplished by translating the bottom wedge relative to the top wedge, thereby changing the total retardation thickness, d. The retardation is $(2\pi d / \lambda)\Delta n'$, where $\Delta n'$ is the birefringence and λ is the wavelength.

The slider can be treated as a birefringenet element at fixed orientation with very small birefringence. The Mueller matrix for such an element is

$$\mathbf{M}_S(\delta^s) = \begin{bmatrix} 1 & 0 & 0 & 0 \\ 0 & 1 & 0 & 0 \\ 0 & 0 & \delta^s & 0 \\ 0 & 0 & 0 & \delta^s \end{bmatrix} \qquad 5.6$$

The compensator was inserted in the optical train and rotated to test its effect on the birefringence developed due to the parasitic effects. The position of the compensator to null these effects was set at 0^o angle with respect to the reference direction (chapter 3). Figure 5.8 shows the output of channel one with and without the compensator. This demonstrates the ability to use the compensator to null the parasitic effect.

5.2 Rheometer results

5.2.1 Test measurements

As an initial test of the rheometer, a series of measurements was performed using different films of Fomblin YR. The test procedure was repeated at different speeds in random order to determine the influence of different elements on the measurements.

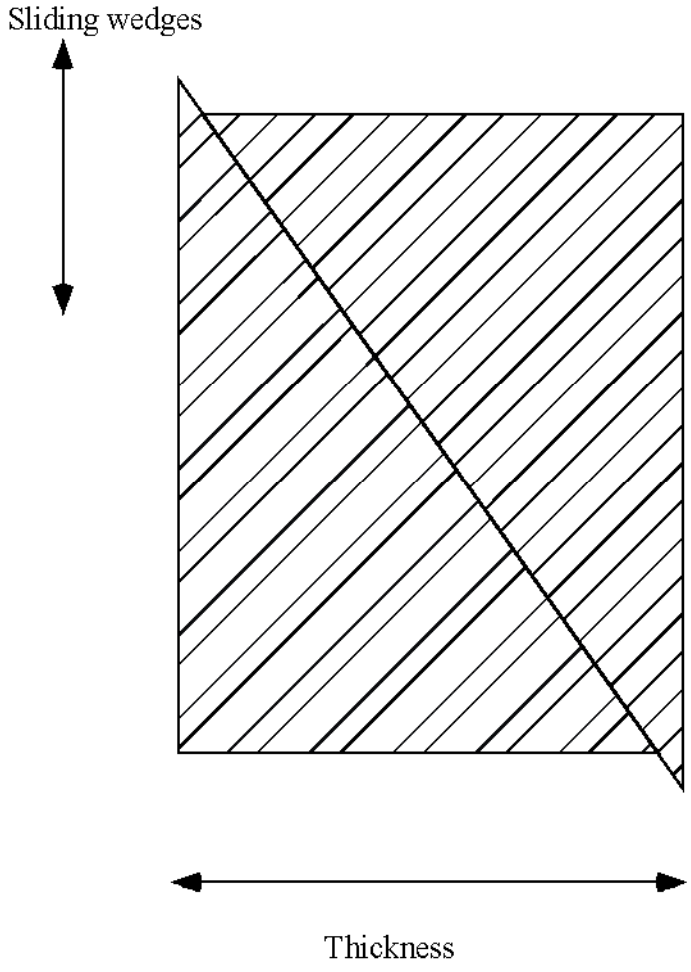


Figure 5.7 Soleil-Babinet compensator

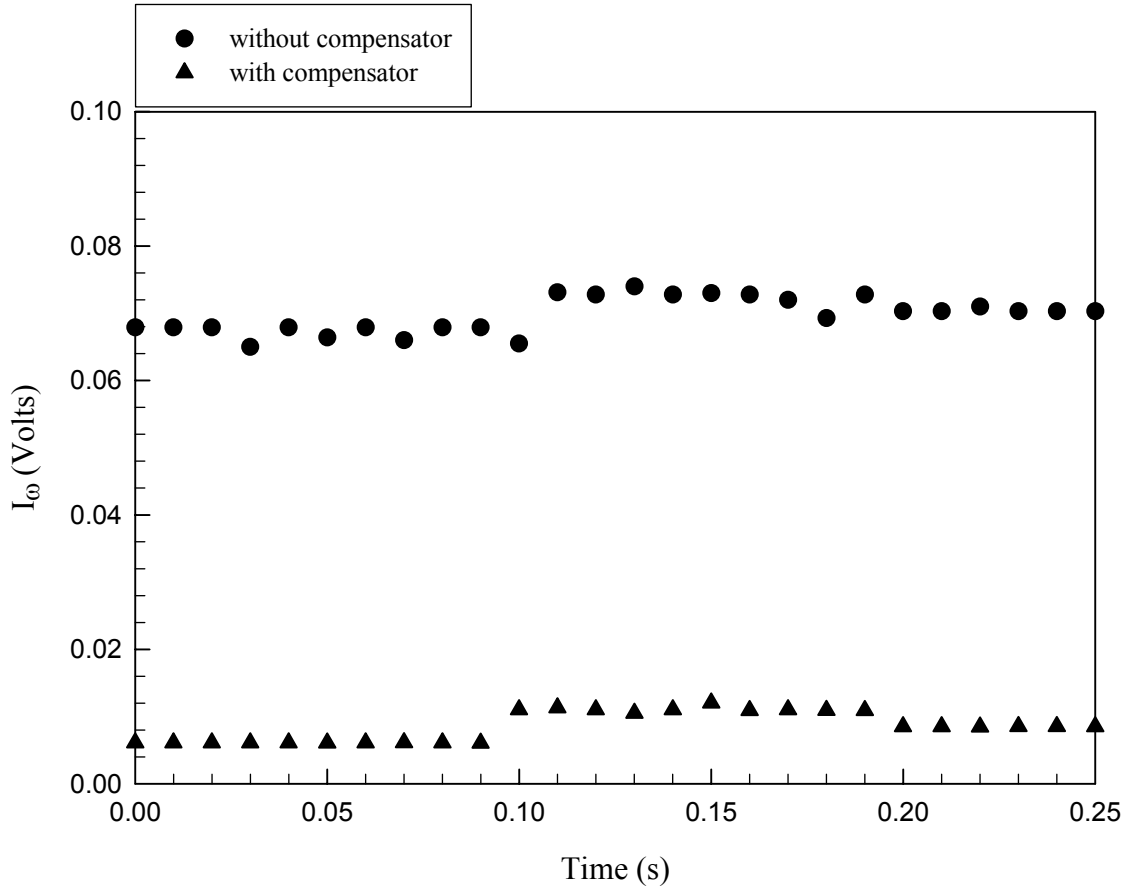


Figure 5.8 Output of channel 1 without and with Soleil-Babinet compensator

5.2.1.1 Force measurements

The shear stress is calculated by measuring the shear force using the strain gauges and the area of the slider. Figure 5.9 shows the shear stress for one full revolution on a sample of Fomblin YR. The sample has a film thickness of 485 nm and the sliding speed was 50 mm/s. The measured shear force τ on a slider with area A from a film with thickness h is

$$\tau = \frac{\eta V}{h} \tag{5.7}$$

where η is the viscosity of the film, V is the relative slider-disk velocity. Variations in h can introduce considerable error into the shear stress calculations.

5.2.1.2 Capacitance measurements

To measure and monitor the thickness, the capacitance method was used; the capacitance for the same film was measured over one revolution. Figure 5.11 shows the measured capacitance and the calculated thickness using the calibration curve for the capacitance. The variation of the thickness, which may arise from the disk topography, is within 12%.

5.2.1.3 Normal force measurements

The slider is loaded on a motorized micrometer that brings the slider down to the disk, applying a normal force of the desired value. The normal load is measured with strain gauges that are attached to the slider arm. The normal load for an 800 nm film is shown in figure 5.12. The normal load is constant over one revolution and with reproducibility over several revolutions as seen in figure 5.12.

5.2.1.4 Shear stress vs. capacitance

As a first test of the rheometer, it was used with a film to study the shear stress and capacitance for one revolution. Both shear stress and capacitance vary with the thickness of the film in inverse proportional. When the film thickness under the slider area varies substantially within one revolution on the desk, then the measured shear stress and

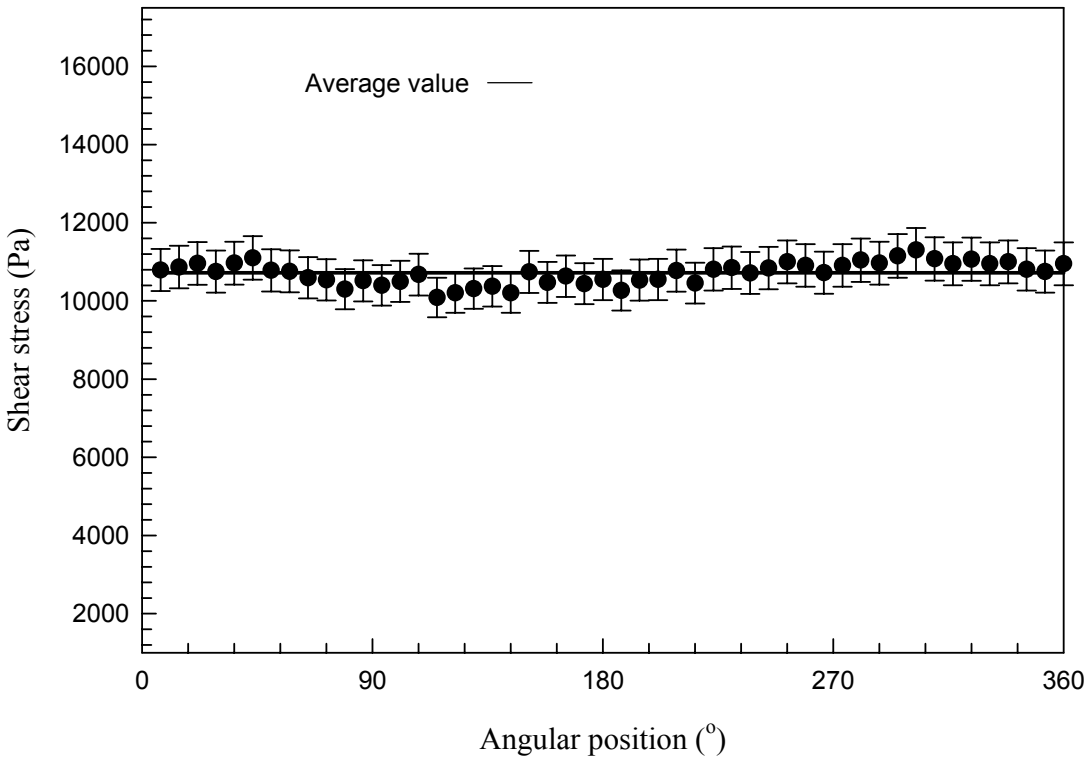


Figure 5.9 Shear stress for one revolution, the film is Fomblin YR with thickness of 485 nm and sliding speed 50 mm/s.

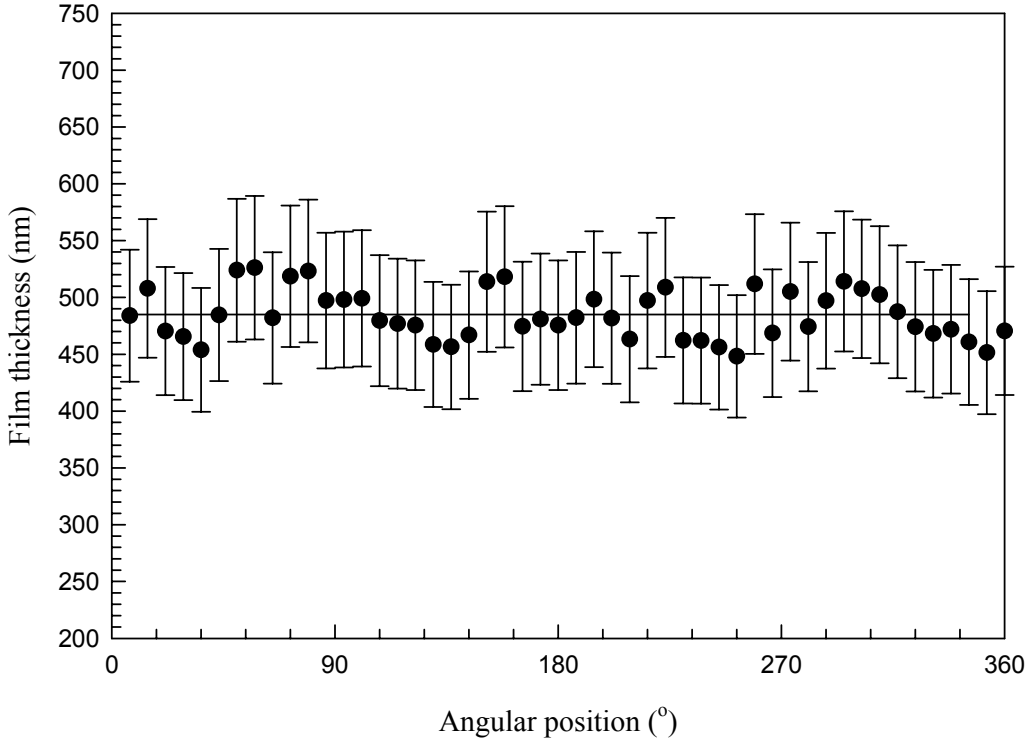


Figure 5.10 Film thickness calculated from the capacitance

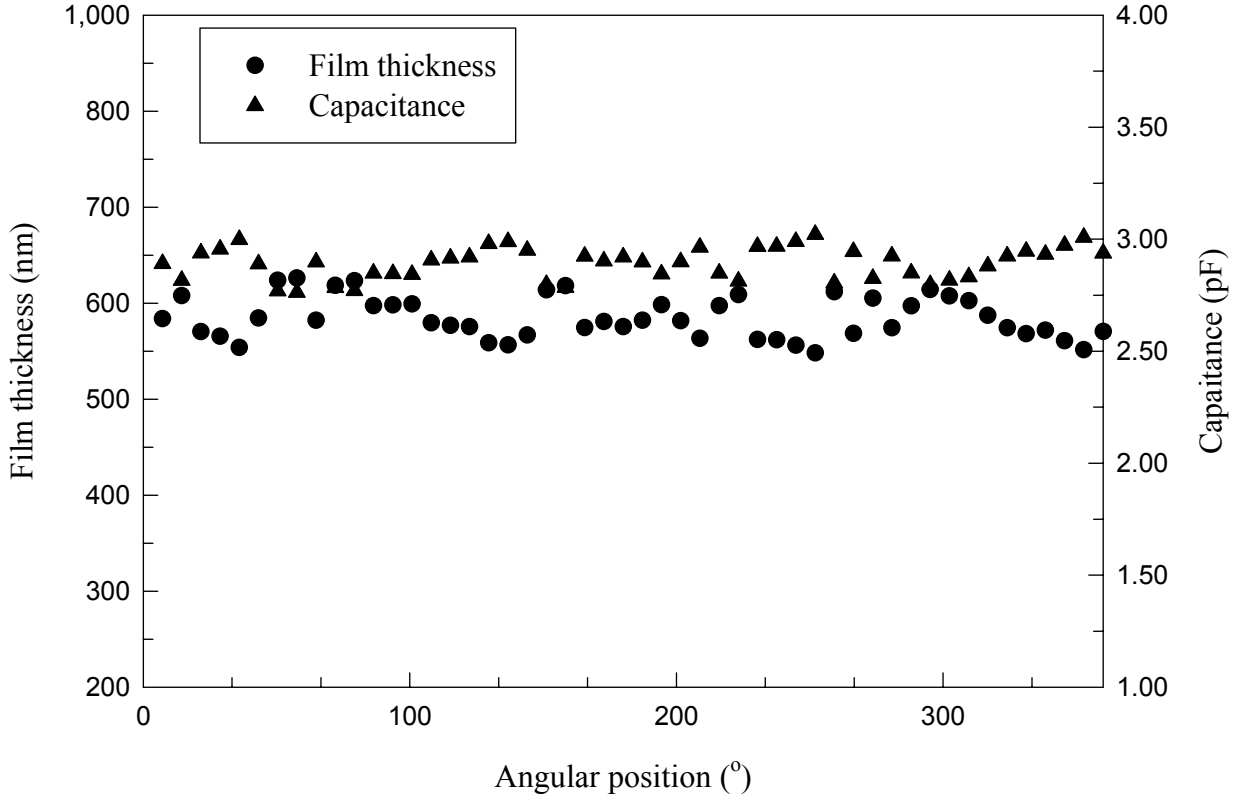


Figure 5.11 Capacitance and thickness for film of 485 nm thickness at sliding speed 50 mm/s

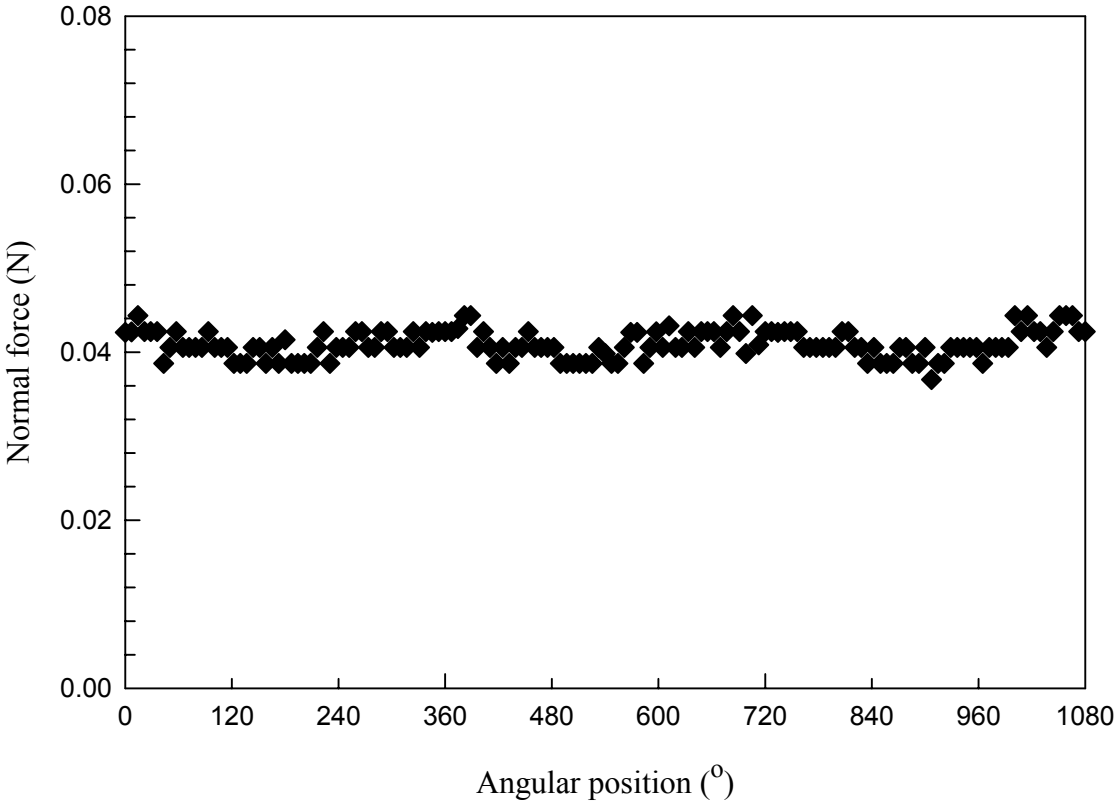


Figure 5.12 Normal load output voltages for three rotations

capacitance under the same slider area would not agree. The results displayed in figure 5.13 show a good agreement in the variation of the shear stress and capacitance.

5.2.1.5 Viscosity measurements

The viscosity is calculated using equation 3.6. The shear rate is calculated by measuring the film thickness and rotational velocity using equation 3.5. Both thickness and rotational velocity were measured simultaneously. The viscosity as a function of the disk position during a full revolution with shear rate of 1.03×10^{5} s^{-1} is represented in figure 5.14. The variations in the viscosity are within the uncertainty introduced by different measured quantities which is about ±20%.

5.2.1.6 Viscous heating

One of the most serious difficulties in achieving rheological measurements for complex fluids at high shear rates is the viscous heating. The consequences of temperature rise is twofold: it manifests itself as a rheological behavior (section 3.2.2) and so can lead to changes in the pattern of flow and heat generation; second, it can lead to undesirable chemical reactions, such as degradation. In section 3.2.2, it was shown that a temperature rise could be ignored in this design.

To examine the issue of shear heating closely, several experiments were run with Fomblin YR at different film thickness prepared under the same conditions. The experiments were carried out at different shear rate ranges with random change of the rotational velocity to test the effect of shear rate on the viscosity. Figure 5.15 shows the variation of viscosity with shear rate for different films, thickness ranging from 32 μm to 240 nm. The viscosity for the different films shows Newtonian behavior at moderately low shear rate and then shear-thinning behavior (non-Newtonian) at high shear rate with a transition from the Newtonian to the non-Newtonian occurring at a shear rate of $\sim 10^{4}$ s^{-1}.

At the same shear rate, thinner films should transfer viscous heat from their interior to the environment more rapidly than thicker films and thus would have lower average temperature and higher measured viscosity than thicker films. The agreement of the

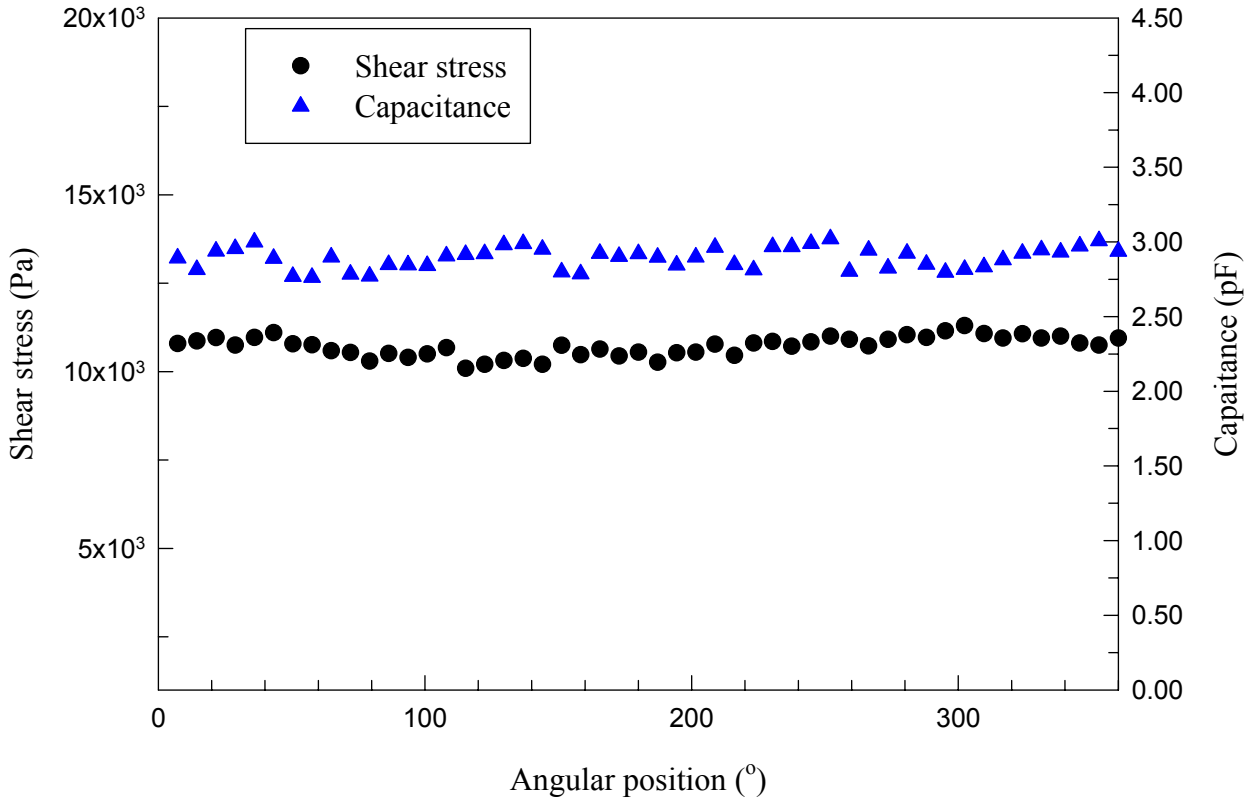


Figure 5.13 Shear stress and capacitance for a disk lubricated with 485 nm Fomblin YR and sliding speed 50 mm/s

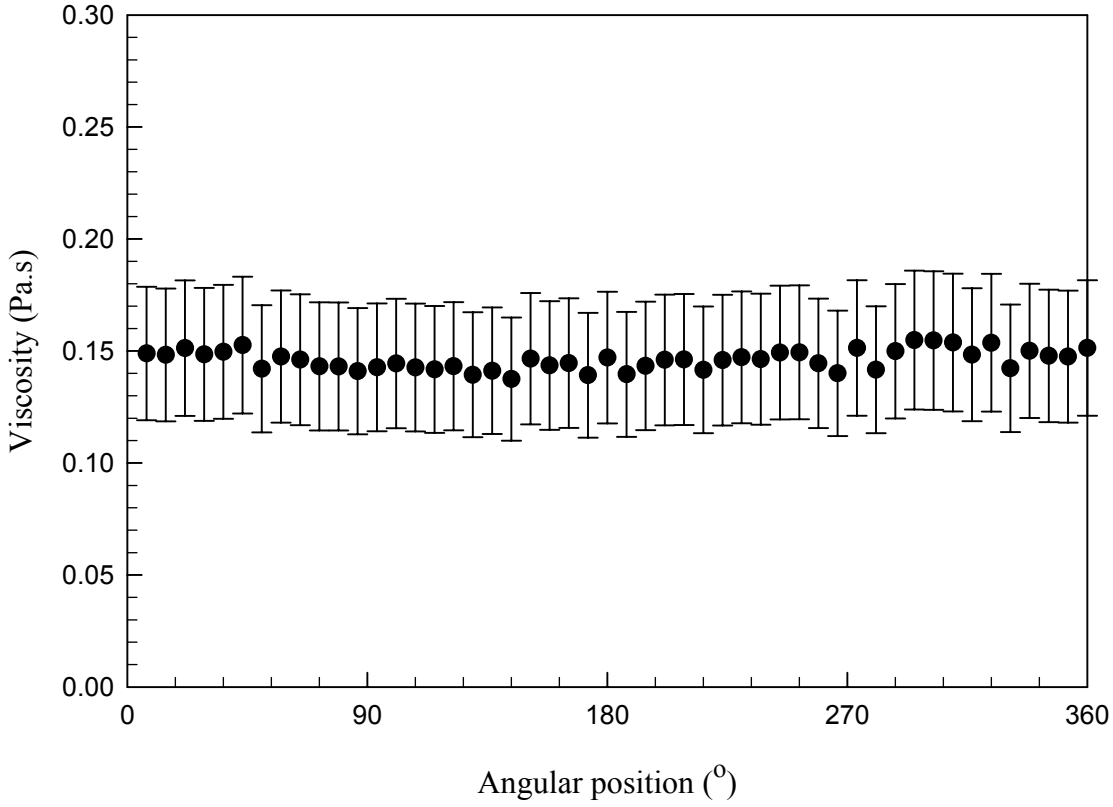


Figure 5.14 Viscosity of Fomblin YR film over one revolution

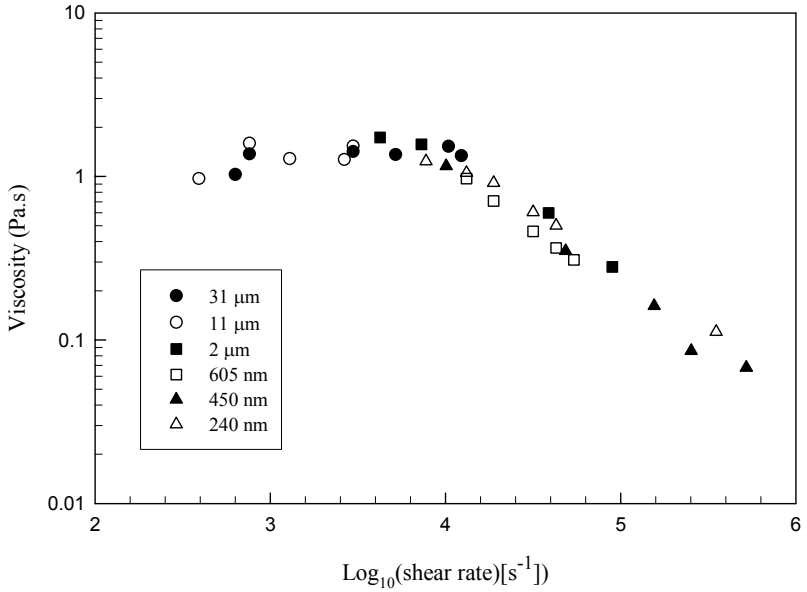


Figure 5.15 Viscosity of Fomblin YR for different films

viscosity behavior of different films with different thicknesses demonstrates that even for the thickest films at even the highest velocity the effect of viscous heating is negligible within measurement error. This can be explained by the fact that even the thickest films studied still sufficiently thin that the viscous heat is efficiently conducted away.

The same behavior for the different films is demonstrated very clearly in the shear stress versus shear rate as in figure 5.16. These results demonstrate the validity of ignoring the viscous heat effect as stated in chapter 3 as a concept used in the design.

5.2.2 Rheology of Fomblin YR

Shear stress (τ) and shear rate ($\dot{\gamma}$) are two important quantities measured in rheology experiments to determine the flow behavior of a fluid. The viscosity function (η) is the best known of the material functions measured in rheology experiments. For a Newtonian fluid, the relation between the shear stress and shear rate is linear with the coefficient of proportionality as the viscosity. This behavior is no longer the case for the non-Newtonian fluid where the viscosity is not constant but is a function of the shear rate.

5.2.2.1 Shear stress vs. shear rate

Measurements of viscosity are carried out in steady-state flow. Before steady state is reached, however, there is a startup transient in which the stress grows from zero at rest to its steady-state value.

Figure 5.17 shows the steady state shear stress versus the shear rate for different films of Fomblin YR. The behavior of different thickness shows agreement of the shear stress and shear rate measured for different films. The shear stress shows a linear relation with shear rate to a certain shear rate and then a transition occurs above that shear rate. The transition shear rate is $\sim 1\times10^{4}$ s^{-1}. Above this transition region, the shear stress varies less strongly with the shear rate. This is the typical case for non-Newtonian flow.

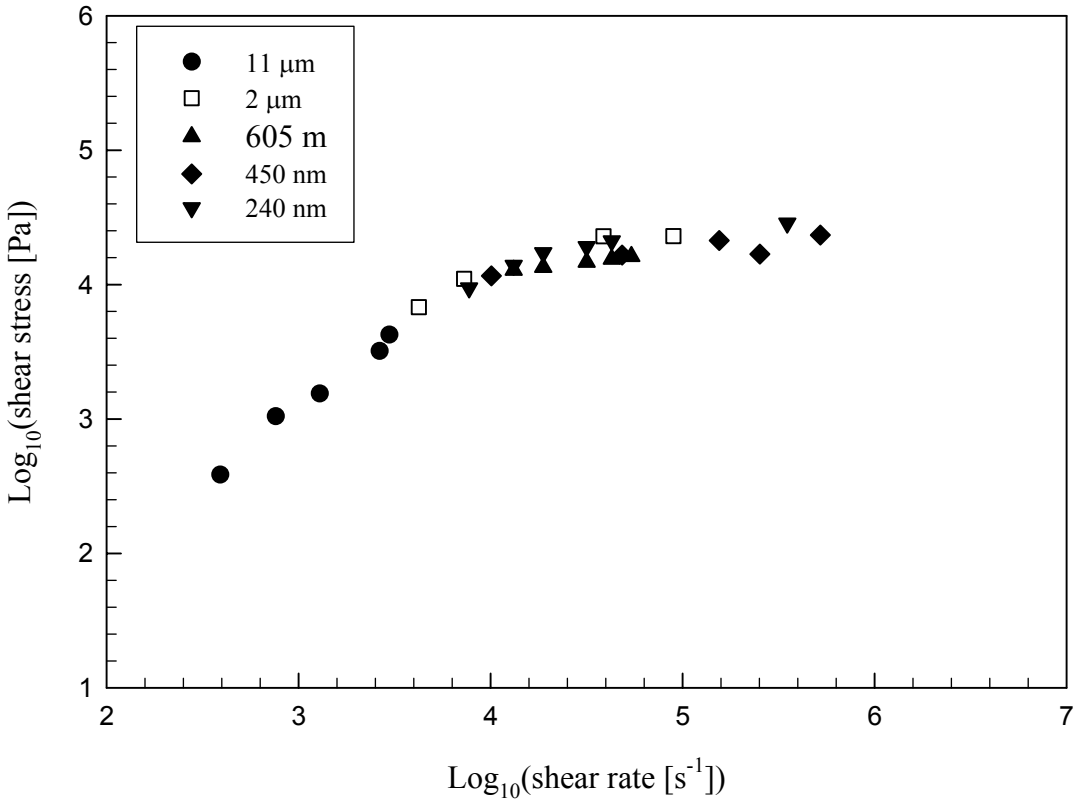


Figure 5.16 Shear stress versus shear rate for different Fomblin YR films

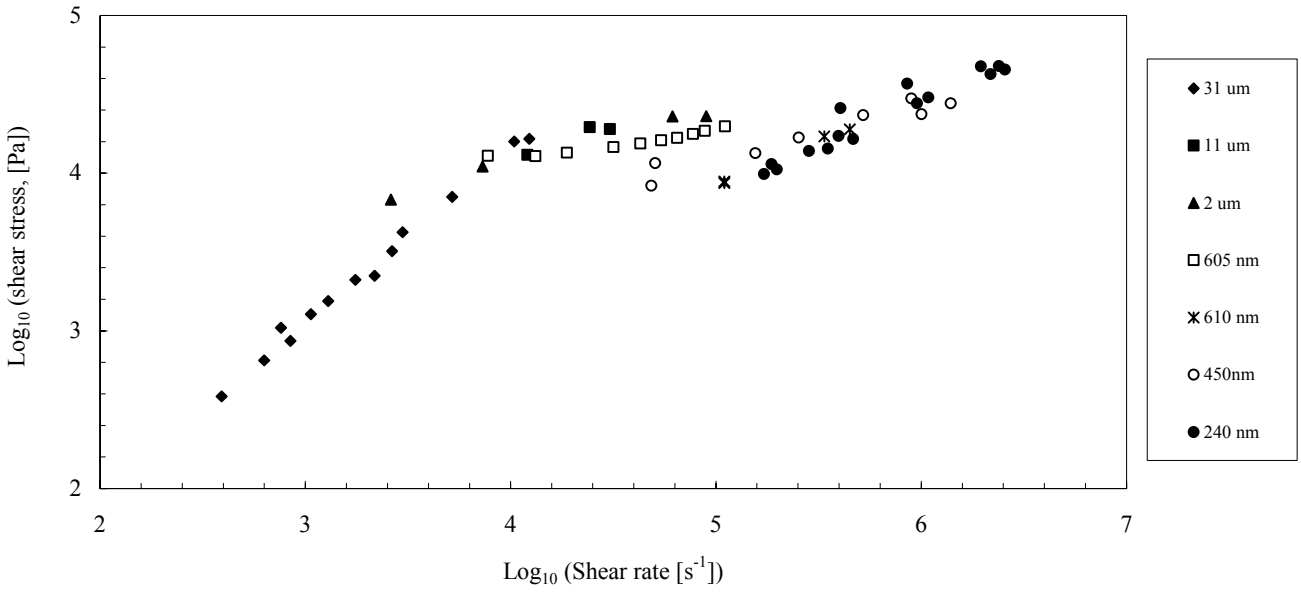


Figure 5.17 Shear stress versus shear rate for different Fomblin YR films

5.2.2.2 Viscosity of Fomblin YR

The viscosity function (η) is the best known of the different material functions measured in rheology experiments. Figure 5.18 shows the viscosity of Fomblin YR taken at different shear rates, $\dot{\gamma}$, ranging from low to the extremely high. At low shear rates, the shear stress is proportional to $\dot{\gamma}$, and the viscosity approaches a constant value η_o, the zero-shear viscosity. At higher shear rates, the viscosity decreases with increasing shear rate. This is the shear-thinning region. The range of shear rate over which the transition from the constant viscosity to the shear-thinning region is fairly narrow for narrow molecular weight distributions (see chapter 6). As the molecular weight distribution broadens, the transition region is broadened.

The transition occurs at shear rates which is proportional to the relaxation time of the polymer. The relaxation time is about 10^{-4} s for this system based on the transition shear rate.

The most important point from this graph is the high shear rate achieved in the experiment, 2.5×10^6 s^{-1}, with a film thickness of 240 nm. The estimated zero shear viscosity can be obtained from the extrapolation of the viscosity data to the low shear rate range. The estimated zero shear viscosity is found to be 1.21 Pa.s, which is in good agreement with previous published data.

The dependence of viscosity on shear rate constitutes an important physical characteristic of polymeric systems, determined by their nature, the temperature, and the pressure. The graphical representation of the dependence of viscosity on shear rate is called the flow curve. Figures 5.17 and 5.18 give complete flow curves.

5.2.2.3 Rheology of Fomblin YR: Discussion

The rheology of PFPEs has been a subject of intensive research since the fluids are used in many practical applications as well as to study the rheology at high shear rate. Simulations provide techniques capable of predicting the rheological parameters at high shear rate. The experimental techniques are limited to moderately high shear rates. Combining the nonequilibrium molecular dynamics [65,66] results with

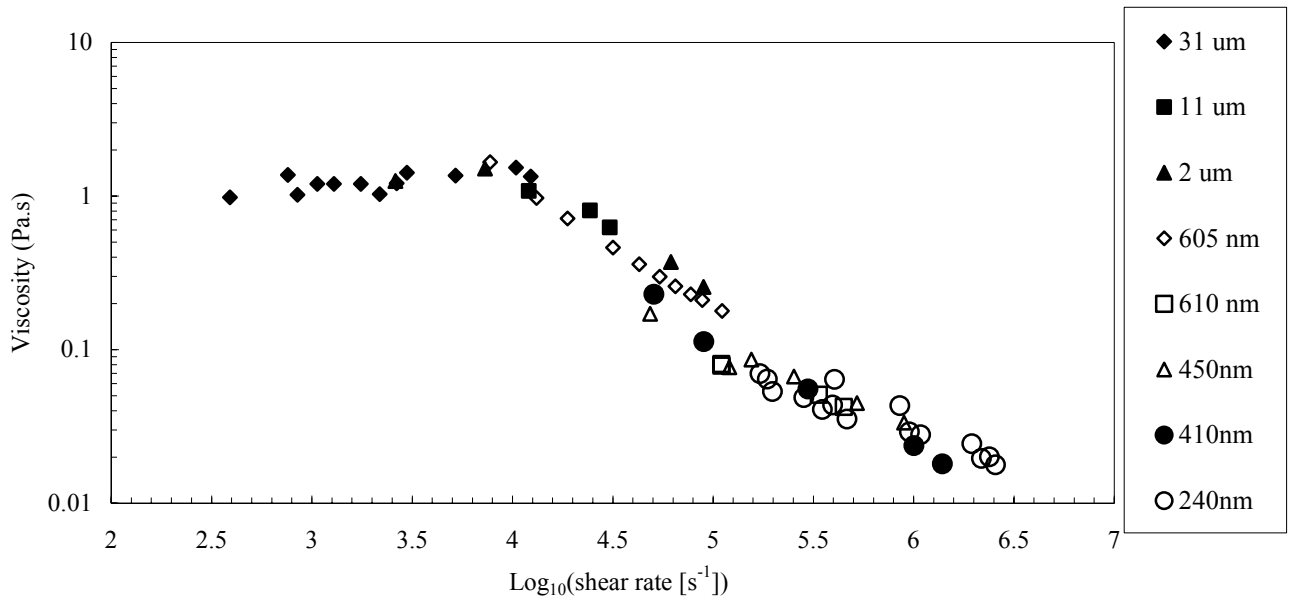


Figure 5.18 Shear viscosity for different Fomblin YR films

the experimental results at high shear rates can provide a test for predictive theory of flow for lubricants and other polymers measurements. The experiments were carried out at a temperature of 25ºC, and there was no temperature change during the experiment. Their results show a transition to shear thinning at shear rate higher than 1×10^4 s^{-1}, and the zero shear viscosity was 1.70 Pa.s.

Bhushan [24] measured the viscosity for Fomblin YR using a similar design to the present apparatus. Their experiment was carried out with a velocity ramp from 3.4 mm/s to 297 mm/s. They reported apparent shear-rate dependence in the calculated viscosity. The onset of this shear-rate dependence was at the apparent shear rate of about 10^5 s^{-1}. They reported negligible temperature rise. In a subsequent work, Bhushan etal.[67] reported that viscosity could be measured to about 10^6 s^{-1} except for samples with viscosity less than about 0.5 Pa.s for which measurements were made to about 6×10^6 s^{-1}. Measurements were limited by pitching of the slider at friction force about 900 mN, corresponding to shear stress about 0.6 MPa. Cantow's results [21] and Bhushan's earlier results [24] are in figure 5.19 [68]. In the figure, the predicted data were modeled based on the Carreau shear-thinning equation and the modified Roelands thermal thinning equation [69]. The difference between the experimental and predicted results was attributed to a temperature rise, as opposed to the claim reported by Cantow [21].

The present experiments were carried on different thicknesses to rule out the viscous heat effect. The apparent viscosity has been measured for different thicknesses ranging from 31 μm down to 240 nm. The calculated viscosities for the different films show apparent shear rate dependence with onset starting at shear rate ~ 10^4 s^{-1} (figure 5.17).

The results agree with the reported results by Cantow [21], as well as with similar results using different approaches reported by Streator [23].

5.3 Birefringence of Fomblin YR

The stresses generated in the flow of polymer fluids are caused by the displacement of polymer chains from their equilibrium random configurations toward elongated configurations. These elongations are not isotropic, and the result is anisotropic optical

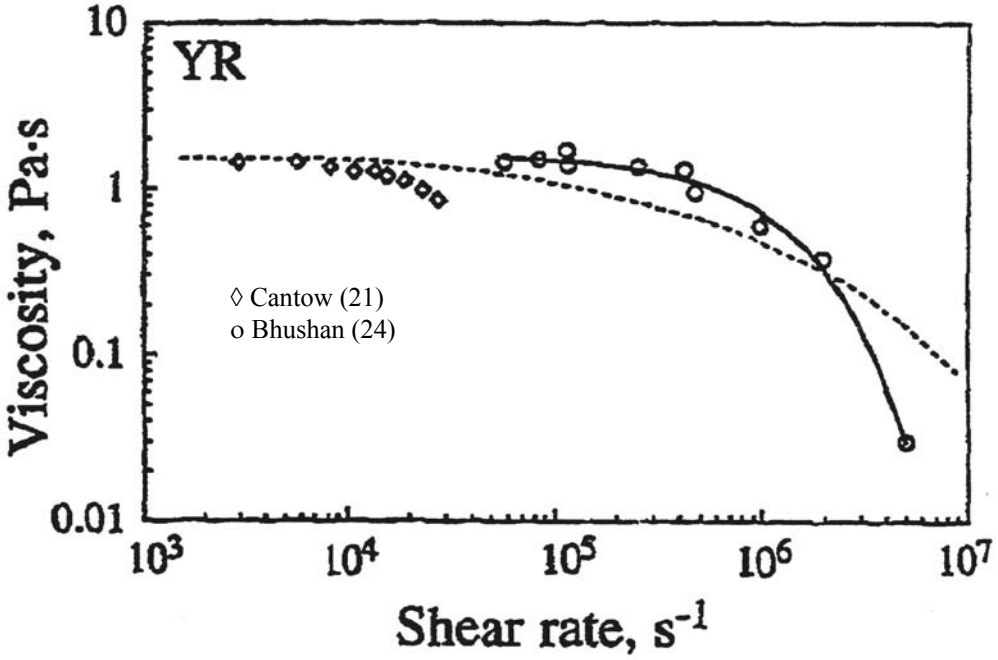


Figure 5.19 Shear rate dependence of the viscosity and the predicted shear thinning behavior of Fomblin YR (Data of references 21 and 24 as analyzed in reference 68)

properties or birefringence that can be detected by means of interaction of light with the anisotropic medium.

The birefringence in Fomblin YR films during shear flow was studied in order to explore the capability of the instrument to measure birefringence. Three different film thicknesses were used to study the influence of shear on the birefringence and to observe any evidence of viscous heat developed in the film.

Figure 5.20 shows the birefringence of three different films with the shear rate. The graph contains the birefringence magnitude multiplied by the orientation angle (I_X). The data show opposite behavior from the expected, especially at low shear rate. This indicates a background birefringence developed within the experiment in the slider and disk. The birefringence of the sample becomes larger than the background at high shear rates, and the flow birefringence becomes dominant. Statistical analysis [70] shows that the background at low shear rate can be subtracted, and a typical flow birefringence curve can be obtained. Appendix B discusses the analysis of this data.

Figure 5.21 shows the birefringence data after background correction vs. the shear rate. The accuracy of the birefringence was plot with 95% confidence in figure 5.21-b. The highest shear rate achieved was 1.30×10^{6} s^{-1}. At low shear rate, the birefringence shows small deviation from zero indicating very small level of chain alignment. The results reveal a transition in the properties of the samples beyond a certain shear rate. The transition occurs in the upper 10^{4} s^{-1} range. At higher shear rate, the birefringence indicates chain alignment and anisotropy due to shear stress. The films of different thickness show similar shear-rate effects at low as well as high shear rate. The agreement of shear flow birefringence developed in the different thicknesses shows that there is no viscous heating effect on the results.

Figure 5.22 shows the shear-rate dependence of the birefringence magnitude and the viscosity measured simultaneously at high shear rate on three films of different thickness. The above results demonstrate the ability of the instrument to measure flow-induced birefringence based on the polarization modulation technique. The instrument is capable of measuring small birefringence as low as $2.5X10^{-5}$.

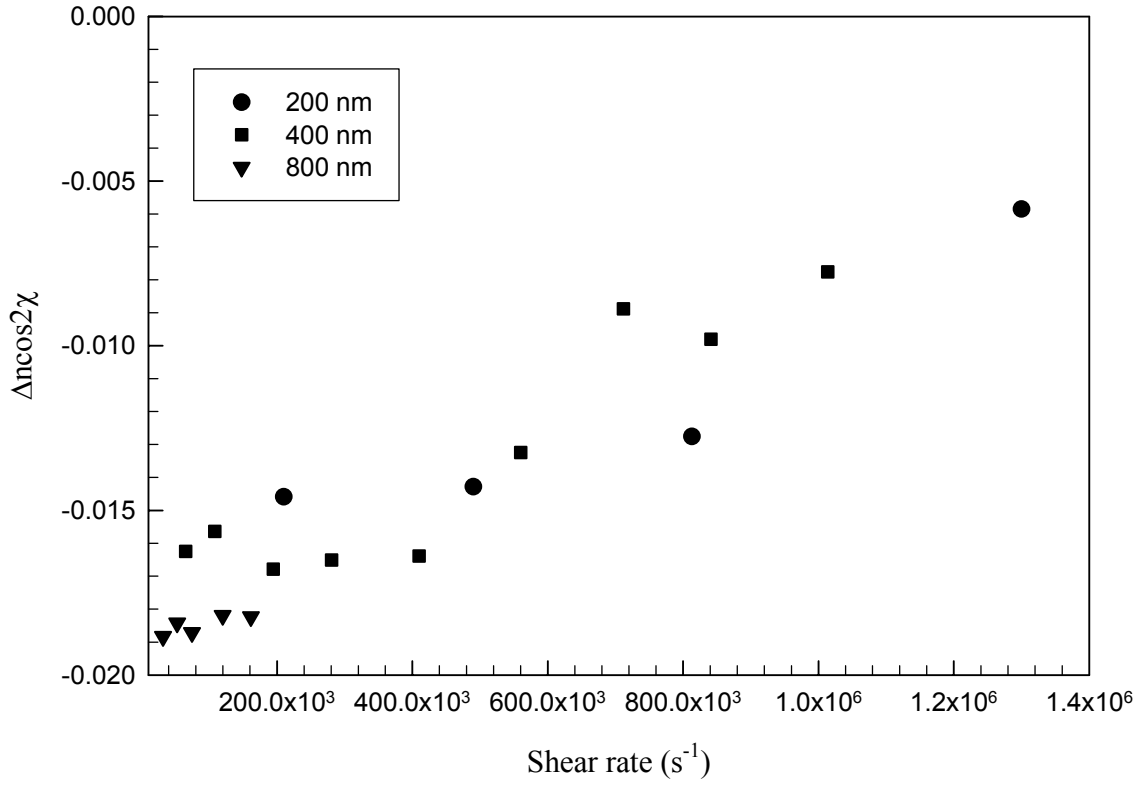
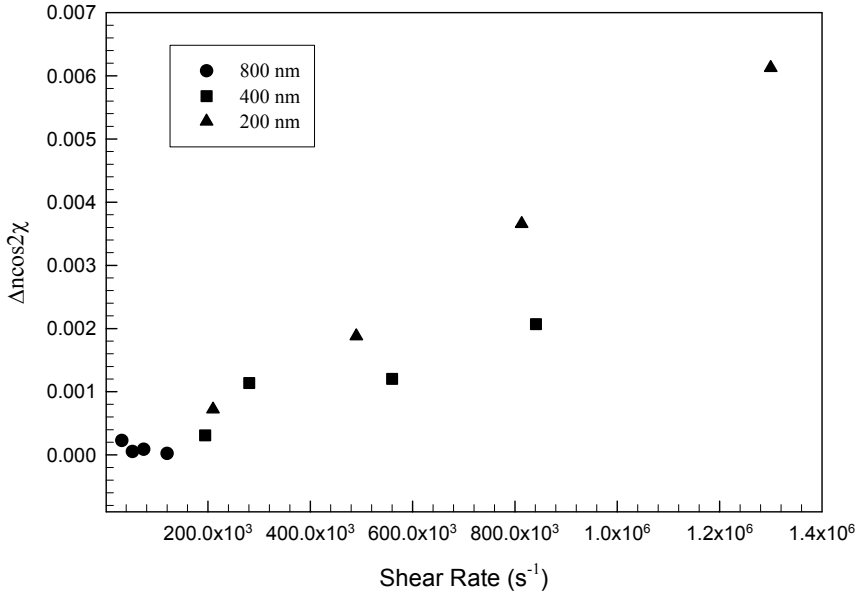
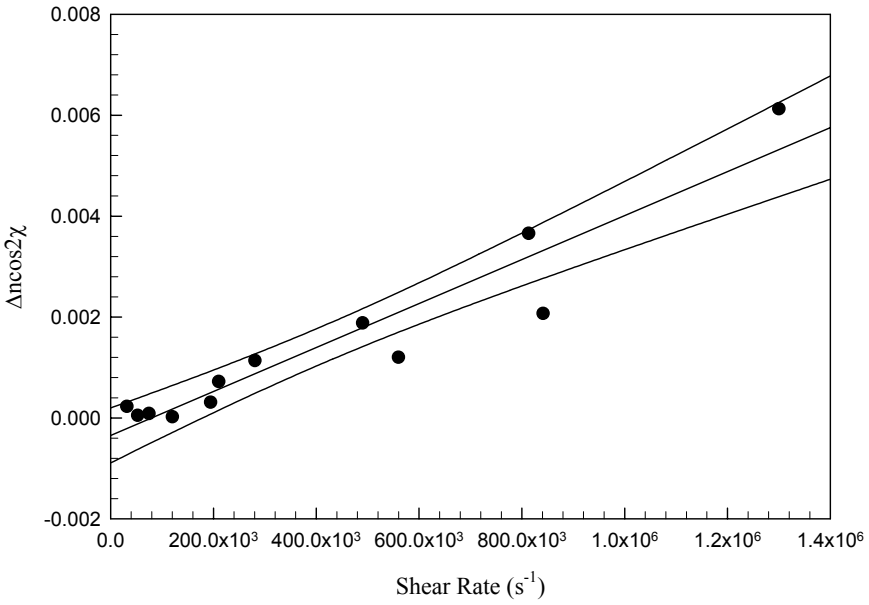


Figure 5.20 Birefringence data with background for different Fomblin YR films



a) Birefringence with different thicknesses



b) Birefringence within 95% confidence

Figure 5.21 Birefringence data for Fomblin YR with background subtracted

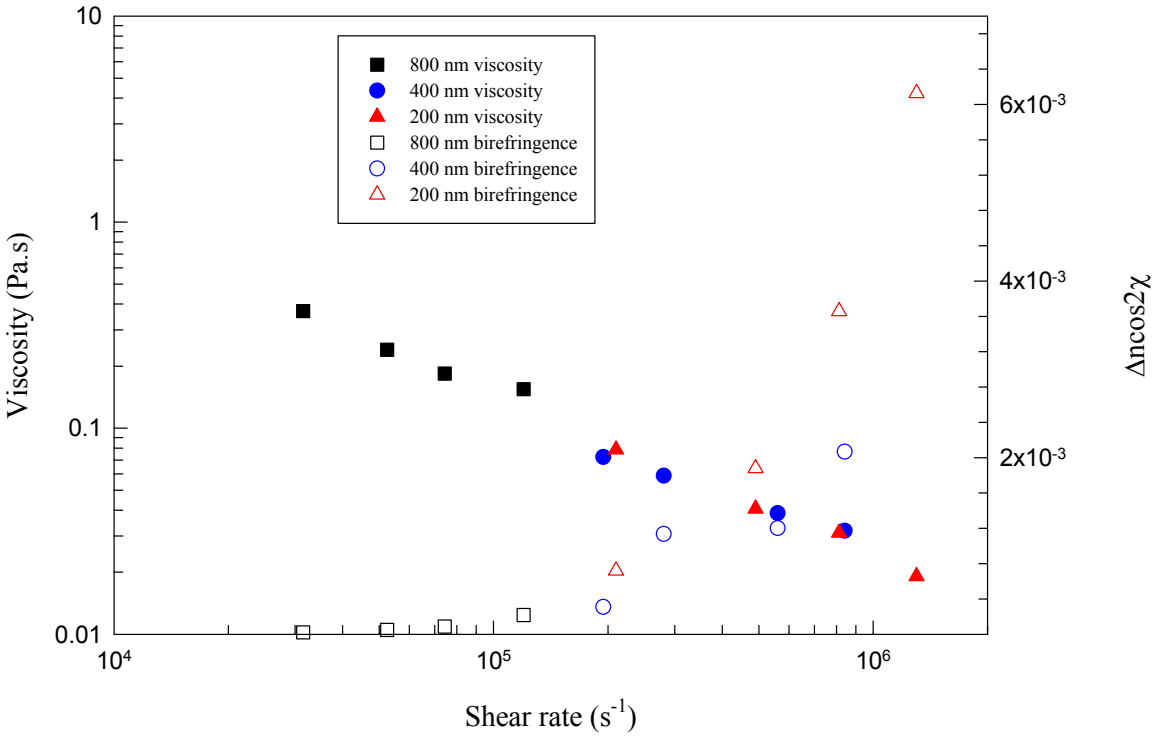


Figure 5.22 Shear viscosity and flow induced birefringence at high shear rate

CHAPTER 6
CONCLUSIONS AND FUTURE WORK

6.1 Conclusions

Measurements of rheological properties at high shear rate represent a challenge because of the difficulties in making measurements under well-controlled conditions. Under high shear rate, it is difficult to discern the true rheological response of the liquid from its apparent behavior because of various disturbances that influence the flow at high shear rates. The most difficult problem is the dissipation of viscous heat.

An optical rheometer capable of measuring high and extremely high shear rates within well-controlled conditions has been designed and constructed based on different concepts. The two parallel-plates rheometer design was based on the magnetic hard disk drive system. The rheometer was designed to achieve thin films with thickness < 100 nm and relatively high rotational speed, which allow achieving high shear rates without temperature rise in the film. The film thickness was measured and monitored *in situ* using a capacitance technique, which was integrated within the system.

A birefringence technique was integrated into the rheometer to investigate the structural changes in complex liquids and the relationships between the rheological properties and the structural changes. The birefringence measurements were based on measuring the polarization properties of light emerging from the sample. The polarization state of light was modulated using a photoelastic modulator. The technique allows measuring the retardation and orientation simultaneously using the Fourier analysis of the waveform.

The calibration for the optical rheometer showed high accuracy in the measurements. The rheometer was tested using the perfluoropolyether compound Fomblin YR. The rheological results showed agreement with previously published data. The viscosity of different films at different shear rates has been studied, and there were no signs of viscous heating. The birefringence was calibrated and tested using a quarter wave plate. The birefringence of the plate behavior was in good agreement with the theoretical expected behavior, indicating good alignment and collimation. The small

deviations are within the accuracy of the different elements. The instrument was successful in measuring a small birefringence of magnitude $2.5X10^{-5}$.

The rheological properties were studied at high and extremely high shear rates for Fomblin YR. Both the viscosity and shear stress were measured against the shear rate. The flow curves exhibited a Newtonian behavior at shear rates up to the lower range of 10^4 s^{-1}. A transition onset appeared at higher shear rate with a shear-thinning flow at higher shear rates. Different films with different thicknesses showed similar rheological behavior. The highest shear rate achieved was $2.6X10^6 s^{-1}$ with a film of thickness 240 nm, the thinnest film was 200 nm. The estimated zero-shear viscosity was 1.21 Pa.s.

The instrument achieved, for the first time, high and extremely high shear-rate birefringence measurements. The birefringence results for different films indicate shear-induced structural changes within the samples. The onset of structural changes is within the upper range of $10^4 s^{-1}$shear rate. More pronounced shear-thinning transitions could be seen in the lower $10^5 s^{-1}$ range. The shear-induced structural changes observed in the birefringence were correlated to the shear thinning flow properties. Both showed close match in the transition onset and in the shear thinning effect exhibited by the different samples.

The results obtained from the optical rheometer were discussed in accordance with previously published results on similar systems and were in closed agreement. This confirmed the precision and accuracy of this instrument.

A high shear-rate optical rheometer for rheological and structural properties of complex fluids has been designed, built, calibrated, and tested. The instrument constitutes a valuable research tool aimed at narrowing the gap between the existing rheological techniques and the simulation tools available at higher strain rates. The results from the simulations and the experiment may be of value in testing a general flow theory for complex fluids.

6.2 Future work

An optical rheometer to study rheological and structural properties of complex fluids under high shear rates was designed and tested in this work. The instrument was

used to measure rheological and structural properties of polymer samples. The thinnest film achieved was 240 nm with the highest shear rate of $2.6X10^{6}s^{-1}$. The higher shear rates can be achieved through thinner films and higher rotational speed. A better surface quality is needed to achieve thin films below 50 nm thicknesses. Applying variable speed may help in achieving high shear range through a single experiment where a velocity ramp can be achieved within one cycle. This also will allow an investigation of the transient effects such as stress growth and stress relaxation. The birefringence data obtained under such transient conditions would be very valuable.

The birefringence can be improved to measure smaller responses using a photomultiplier tube and high-speed digitizer. Both the retardation and orientation can be measured simultaneously and separately by adapting four lock-in amplifier configurations (28). A Wollaston prism can be used as a beam splitter to replace the analyzer and the two polarized beams can be analyzed simultaneously to obtain the retardation and orientation without the need to physically rotate any of the elements in the experiment. Another optical structure probe could be achieved by installing a small angle light scattering technique. The scattered beam could be used to probe the structural factor, and the emanating light could be used to study the flow-induced anisotropy.

It is well known that the viscosity of molten linear polymers is a function of molecular weight, shear conditions, temperature, and pressure. Studies [50, 55, 71] showed that the molecular weight dependence of viscosity shows a linear increase of the viscosity with molecular weight below a critical molecular weight. Above such critical molecular weight, the viscosity shows much more rapid increase with molecular weight. To study such dependence of viscosity on molecular weight, several highly fractionated samples of the perfluoropolyether compound Fomblin Z-15 have been prepared (in collaboration with Val Krukons at Phasex Corporation). The Fomblin Z-15 is linear random copolymer with nonreactive end groups CH_3. The samples were characterized by GPC measurements (American Polymer Standard corporation). The parent sample has a molecular weight of 7,750 gm with polydispersity 1.66. The cuts were characterized using the GPC measurements (carried out at different time than the parent sample) and their polydispersity factors are < 1.08, which indicates a polydispersity close to

monodisperse fractions. (One sample shows deviation in its GPC measurements of molecular weight; the GPC measurements should be repeated). The set up is an ideal system to study the flow behavior of the different cuts and investigate the viscosity dependence on molecular weight under high shear rate flow. Results of such research can be very beneficial to the processes in which complex fluids, such as lubricants, are used and to understand their rheological effect on their tribological behavior. These results may be very helpful in order to test the simulation results and to establish tools allowing the design of such complex fluids with particular properties.

BIBLIOGRAPHY

BIBLIOGRAPHY

1) R. B. Bird, R. C. Armstrong and O. Hassager. Dynamics of polymeric liquids: Vol. I, Fluid mechanics, John Wiley and Sons, New York (1977).
2) R. B. Bird and C. F. Curtiss, Physics Today. 84, 36 (1984).
3) F. A. Morrison, Understanding rheology, Oxford University Press, New York (2001).
4) C. W. Macosko, Rheology, Principles, Measurements, and Applications, Wiley-VCH, New York (1994).
5) K. Walters, Rheometry, Chapman and Hall, London (1975).
6) J. R. Van Wazer, J. W. Lyons, K. Y. Kim and R. E. Colwell, Viscosity and Flow Measurements, Wiley-Interscience, New York, (1963).
7) R. B. Bird, W. E. Stewart and E. N. Lightfoot, Transport phenomena, John Wiley and Sons, New York (2002).
8) G. G. Fuller, Optical rheometry of complex fluids, Oxford University Press, New York (1995).
9) R. M. A. Azzam and N. M. Bashara, Ellipsometry and polarized light, North Holland, Amsterdam (1977).
10) M. Born and E. Wolf, Principles of optics, Pergamon (1980).
11) H. Janeschitz-Kriegl, Polymer melt rheology and flow birefringence, Springer-Verlag, Heidelberg (1983).
12) J. L. S. Wales, The application of flow birefringence to rheological studies of polymer melts, Delft University Press, Rotterdam (1976).
13) F. D. Baxter and J. C. Miller, Trans. Soc. Rheol., V, 193 (1961).
14) J. A. Kornfield, G. G. Fuller and D. S. Pearson, Macromolecules, 22, 1334 (1989).
15) T. Takahashi and G. G. Fuller, Rheol. Acta, 35, 297 (1996).
16) M. C. Friedenberg, G. G. Fuller, C. W. Frank and C. R. Robertson, Macromolecules, 29, 705 (1996).
17) G. G. Fuler, Annu. Rev. Fluid Mech., 22, 387 (1990).
18) K. Osaki, N. Bessho, T. Kojimoto and M. Kurata, J. Rheol., 23, 457 (1979).
19) A. W. Chow and G. G. Fuller, J. Rheol., 28, 23 (1984).

20) A. S. Lodge, SAE 872043, (1987).
21) M. J. R. Cantow, T. Y. Ting T. M. Barrall, H. R. S. Porter and E. R. George, Rheol. Acta, 25, 69 (1986).
22) R. W. Connelly and J.Greener, J. Rheol., 29, 209 (1985).
23) J. L. Streator, J. P. Gerhardstien and C. B. McCollum, J. Tribo., 116, 119 (1994).
24) U. Jonsson and B. Bhushan, J. Appl. Phys., 78, 3107 (1995).
25) M. Mooney, J. Appl. Phys., 35, 23 (1934).
26) G.V. Vinogradov and A. Ya. Malkin, Rheology of Polymers: Viscoelasticity and flow of polymers. Springer-Verlag, Berlin (1980).
27) J. C. Kemp, J. Opt. Soc. Am., 59. 950 (1969).
28) G. E. Jellison, Jr. and F. A. Modine, Handbook of Spectroscopic Ellipsometry (H. G. Tompkins and E. Irene, eds.) Noyes (2003). In press.
29) D. M. Binding and K. Walters, J. Non-Newt. Mech., 1, 277 (1976).
30) A. S. Lodge, Nature, 176, 838 (1955).
31) W. Philippoff, Nature, 178, 811 (1956).
32) B. Koeman and H. Janeschitz-Kreigl, J. Phys. E: Sci. Instrum., 12, 625 (1979).
33) T. Oakberg, SPIE 2773, 17 (1996).
34) B. Wang, SPIE 3424, 120 (1998).
35) B. Wang and T. Oakberg, Rev. Sci. Instrum., 70, 3747 (1999).
36) K. Hingladarom, W. R. Burghardt, S. G. Baek, S. Cementwala and J. J. Magda, Macromolecules, 26, 772 (1993).
37) G. E. Jellison, Jr. and F. A. Modine, Appl. Opt., 29, 959 (1990).
38) G. E. Jellison, Jr., C. O. Griffiths, D. E. Holcomb and C. M. Rouleau, Appl. Opt., 41, 6555 (2002).
39) J. I. Kroschwitz and M. Howe-Grant, Encyclopedia of Chemical Technology, Fourth ed., Vol. 11, Wiley, New York (1991).
40) G. May, Chemistry in Britain, August**,** 34 (1997).
41) B. Bhushan, Tribology and Mechanics of Magnetic Storage Devices, second ed., Springer, New York (1996).
42) B. Ameduri, B. Boutevin and G. Kostov, Prog. Polym. Sci., 26, 105 (2001).

43) M. J. R. Cantow, R. B. Larrabee, E. M. Barrall II, R. S. Butner, P. Cotts, F. Levy and T. Y. Ting, MAKROMOL CHEM: Macromolecular Chemistry and Physics, 187, 2475 (1986).
44) G. Gianotti, M. Levi and S. Turri, J. App. Poly. Sci., 51, 973 (1994).
45) S. Turri, E. Barchiesi and M. Levi, Macromolecules, 28, 7271 (1995).
46) A. Sanguineti, P. A. Guarda, G. Marchionni and G. Ajroldi, Polymer, 36, 3697 (1995).
47) M. Levi and S. Turri, J. App. Poly. Sci., 55, 989 (1995).
48) B. A. Wolf, M. Klimiuk and M. J. R. Cantow, J. Phys. Chem., 93, 2672 (1989).
49) C. Gao and B. Bhushan, Wear, 190, 60 (1995).
50) R-N, Kono, S. Izumisawa, M. Jhon, C. A. Kim and H. J. Choi, IEEE Trans. Magn., 37, 1827 (2001).
51) T. E. Karis and M. S. Jhon, Tribo Lett., 5, 283 (1998).
52) D. Saperstien, Appl. Spect., 43, 481 (1989).
53) V. N. Koinkar and B. Bhushan, J. Vac. Sci. Techonl. A, 14, 2378 (1996).
54) L. Xu, F. Ogletree, M. Salmeron, H. Tang, J. Gui and B. Marchon, J. Chem. Phys., 112, 2952 (2000).
55) G. Ajroldi, G. Marchionni and G. Pezzin, Polymer, 40, 4163 (1999).
56) Y-K. Cho and S. Granick, Wear, 2000, 346 (1996).
57) M. Ruths and S. Granick, 7, 161 (1999).
58) C. Ham and B. Bhushan, Rev. Sci. Instum., 69, 3339 (1998).
59) G. E. Jellison, Jr. and F. A. Modine, Appl. Opt., 36, 8184 (1997).
60) F. A. Modine and G. E. Jellison, Jr., Appl. Phys. Commun., 12, 121 (1993).
61) G. E. Jellison, Jr. and F. A. Modine, SPIE Proceedings, 1166, 231 (1989).
62) J. R. Mackey, K. K. Das, S. L. Anna, and G. H. McKinley, Meas. Sci. Technol., 10, 946 (1999).
63) B. Drevillon, J. Perrin, R. Marbot, A. Violet and J. L. Dalby, Rev. Sci. Instrum., 53, 969 (1982).
64) Fomblin® PFPE: Lubricants, Product Data Sheet, Ausimont, Italy, 2002.

65) J. D. Moore, S. T. Cui, H. D. Cochran and P. T. Cummings, J. Chem. Phys., 113, 8833 (2000).
66) J. D. Moore, S. T. Cui, H. D. Cochran and P. T. Cummings, J. Non-Newt. Fluid Mech., 93, 83 (2000).
67) C. Ham and B. Bhushan, J. Appl. Phys., 81, 5384 (1997).
68) H-S. S. Hsiao, B. Bhushan and B. J. Hamrock, Trans. ASME, 118, 396 (1996).
69) H-S. S. Hsiao, B. Bhushan and B. J. Hamrock, Trans. ASME, 118, 388 (1996).
70) W. R. Dillon and M. Goldstein, Multivariate Analysis: Methods and Applications, John Wiley & Sons, New York, (1984).
71) A. M. Homola and H. V. Nguyen, J. Chem. Phys., 94, 2346 (1991).

APPENDICES

APPENDIX A

JONES AND MUELLER CALCULUS

A.1 Jones Vectors

For a monochromatic plane wave of polarized light propagating along the z-axis, the electric field can be represented as

$$\mathbf{E}(z,t) = \left[E_x \cos(\omega t - \frac{2\pi}{\lambda} z + \delta_x \right] \hat{\mathbf{x}} + \left[E_y \cos(\omega t - \frac{2\pi}{\lambda} z + \delta_y \right] \hat{\mathbf{y}} \qquad \text{A-1}$$

E_x and E_y represent the amplitudes of the linear, simple harmonic oscillations of the electric field components along the x and y axes.

Once the unit vectors $\hat{\mathbf{x}}$ and $\hat{\mathbf{y}}$ have been chosen, there is no need to retain the unit vectors in the mathematical expressions of the wave. Also, the field components in space are known to be oscillating sinusoidally with time at the same frequency, such information can be suppressed. The expression of the wave A.1 in an anisotropic material with refractive index n can be written in the form of 2×1-column vector.

$$\mathbf{A} = \begin{bmatrix} E_x e^{i\delta_x} \\ E_y e^{i\delta_y} \end{bmatrix} e^{i\frac{2\pi}{\lambda} nz} \qquad \text{A-2}$$

The mathematical description of the wave can be written by dropping the spatial information about the wave by considering the field over a fixed plane such as z = 0.

$$\mathbf{A} = \begin{bmatrix} E_x e^{i\delta_x} \\ E_y e^{i\delta_y} \end{bmatrix} \qquad \text{A-3}$$

The vector **A** is a representation of the wave which is known to be monochromatic, uniform and transverse-electric. This vector is called the Jones vector. This vector contains complete information about the amplitude and phase, and it is a complex vector. It can be used to represent different polarization states. The Jones vector is not directly measured. Square law detectors measure the intensity I.

$$I = \mathbf{A}.\mathbf{A}^{*} = E_x^2 + E_y^2 \qquad \text{A-4}$$

A.2 Stokes vector

Using the Jones vector, unpolarized or partially polarized light cannot be represented since, by definition, light is described by two orthogonal, completely polarized components. It is desirable to describe the wave in observable quantities that characterize both the amplitude and phase of the wave, and can describe different polarization. This is accomplished using the Stokes vector, **S**, with four components each has the unit of intensity.

$$\mathbf{S} = \begin{bmatrix} S_0 \\ S_1 \\ S_2 \\ S_3 \end{bmatrix} = \begin{bmatrix} |E_x|^2 + |E_y|^2 \\ |E_x|^2 - |E_y|^2 \\ 2\,\mathrm{Re}(E_x.E_y) \\ 2\,\mathrm{Im}(E_x.E_y) \end{bmatrix} \qquad \text{A-5}$$

It is possible to represents unpolarized or partially polarized light with a Stokes vector. It is convenient to use the Stokes vector since its parameters are observable quantities. Jones and Stokes vectors of different forms of polarized light are described in table 2.1.

A.3 Jones and Mueller Matrices

The polarization properties of light can be represented by the Jones vector (**A**) or the Stokes vector (**S**). When light is transmitted through a polarizing element, then the

transmitted light with polarization A_1 or S_1 is related to the incident light A_0 or S_0 through a linear relation

$$\mathbf{A}_1 = \mathbf{J} \cdot \mathbf{A}_0 \qquad \text{A-6}$$

and

$$\mathbf{S}_1 = \mathbf{M} \cdot \mathbf{S}_0 \qquad \text{A-7}$$

where **J** and **M** are the Jones and Mueller matrices, respectively.

The connection between the Stokes and Jones vectors can be used to relate the sixteen-component Mueller matrix to the Four-component Jones matrix.

$$\mathbf{M} = \begin{bmatrix} \frac{(m_1 + m_2 + m_3 + m_4)}{2} & \frac{(m_1 - m_2 - m_3 + m_4)}{2} & (S_{13} + S_{42}) & -(d_{13} + d_{42}) \\ \frac{(m_1 - m_2 + m_3 - m_4)}{2} & \frac{(m_1 + m_2 - m_3 - m_4)}{2} & (S_{13} - S_{42}) & (d_{42} - d_{13}) \\ (S_{14} - S_{32}) & (S_{14} - S_{32}) & (S_{12} + S_{34}) & (d_{34} - d_{12}) \\ (d_{14} + d_{32}) & (d_{14} - d_{32}) & (d_{12} - d_{34}) & (S_{12} - S_{34}) \end{bmatrix} \qquad \text{A-8}$$

where

$$m_i = j_i j_i^*$$
$$s_{ik} = \mathrm{Re}(j_i j_k^*)$$
$$d_{ik} = \mathrm{Im}((j_k^* . j_k)$$

(i,k) = 1, 2, 3, 4 and (j_1, j_2, j_3 j_4) = (J_{11}, J_{22}, J_{12}, J_{21}). The Jones matrix and Mueller matrix for optical elements are essential to analyze the polarization transformation by an optical element. The following is a list of Jones and Mueller matrices for some optical elements. The following notation is used:

$\delta = 2\pi\Delta nd/\lambda$: the retardance,

Δn = the birefringence.

θ = the orientation angle of the element

$s_\theta = \sin(\theta)$; $c_\theta = \cos(\theta)$; $S_\theta = \sinh(\theta)$; $C_\theta = \cosh(\theta)$

1. Birefringent element at 0^o orientation.

$$\mathbf{J} = \begin{bmatrix} e^{i\frac{\delta}{2}} & 0 \\ 0 & e^{-i\frac{\delta}{2}} \end{bmatrix}, \qquad \mathbf{M} = \begin{bmatrix} 1 & 0 & 0 & 0 \\ 0 & 1 & 0 & 0 \\ 0 & 0 & \cos\delta & \sin\delta \\ 0 & 0 & -\sin\delta & \cos\delta \end{bmatrix} \qquad \text{A-9}$$

2. Quarter wave plate at 0^o orientation

$$\mathbf{J} = \begin{bmatrix} e^{i\frac{\pi}{4}} & 0 \\ 0 & e^{-i\frac{\pi}{4}} \end{bmatrix}, \qquad \mathbf{M} = \begin{bmatrix} 1 & 0 & 0 & 0 \\ 0 & 1 & 0 & 0 \\ 0 & 0 & 0 & 1 \\ 0 & 0 & -1 & 0 \end{bmatrix} \qquad \text{A-10}$$

3. Birefringent element at θ^o

$$\mathbf{J} = \begin{bmatrix} c_{\delta/2} + ic_{2\theta}s_{\delta/2} & is_{2\theta}s_{\delta/2} \\ is_{2\theta}s_{\delta/2} & c_{\delta/2} - ic_{2\theta}s_{\delta/2} \end{bmatrix}, \quad \mathbf{M} = \begin{bmatrix} 1 & 0 & 0 & 0 \\ 0 & c_{2\theta}^2 + s_{2\theta}^2 c_\delta & s_{2\theta}c_{2\vartheta}(1-c_\delta) & -s_{2\theta}s_\delta \\ 0 & s_{2\theta}c_{2\vartheta}(1-c_\delta) & s_{2\theta}^2 + c_{2\theta}^2 c_\delta & c_{2\theta}s_\delta \\ 0 & s_{2\theta}s_\delta & -c_{2\theta}s_\delta & c_\delta \end{bmatrix}$$

A-11

APPENDIX B

STATISTICAL ANALYSIS OF THE BIREFRINGENCE DATA

The heart of the use of birefringence in rheology is the stress-optical rule. When a polymer liquid undergoes flow, both the stress tensor τ and the refractive index tensor **n** can be defined and may be related in a linear relation called the stress-optical rule (SOR). That linear relation may not be valid for all polymer liquids under some conditions.

When the flow field is zero, the polymer liquid chains are in their equilibrium random configuration. In such configuration, the net anisotropy is zero; no birefringence is expected (see figure 2.7).

When the polymer is subject to flow, stresses generated in polymer liquids are caused by displacement of polymer chains from their equilibrium random configuration toward elongated configuration. The chains are not randomly oriented, and this nonrandom configuration produces anisotropy that change the polarization properties of light passing through them. The measured birefringence shows deviation from its zero value when there is flow.

Figure B.1 is the birefringence results of different Fomblin YR samples. The initial results show the magnitude of birefringence decreases with increasing shear stress. This behavior of the birefringence data indicates a decrease from a large background birefringence as shear rate increases.

Different statistical models have been applied on the birefringence data at moderate shear rates and high shear rates. Figure B.2 shows the modeling of the data at moderate shear rate. The correlation is weak. The high shear rate data shows strong correlation as in figure B.3.

To explain these results, one needs to take this system into consideration: a shear cell of an optical disk and slider both coated with thin layer of ITO with thickness about 500 nm. When there is no shear (both slider and disk are at a distance), there is some background birefringence due to the structure of the optical parts and the coating,

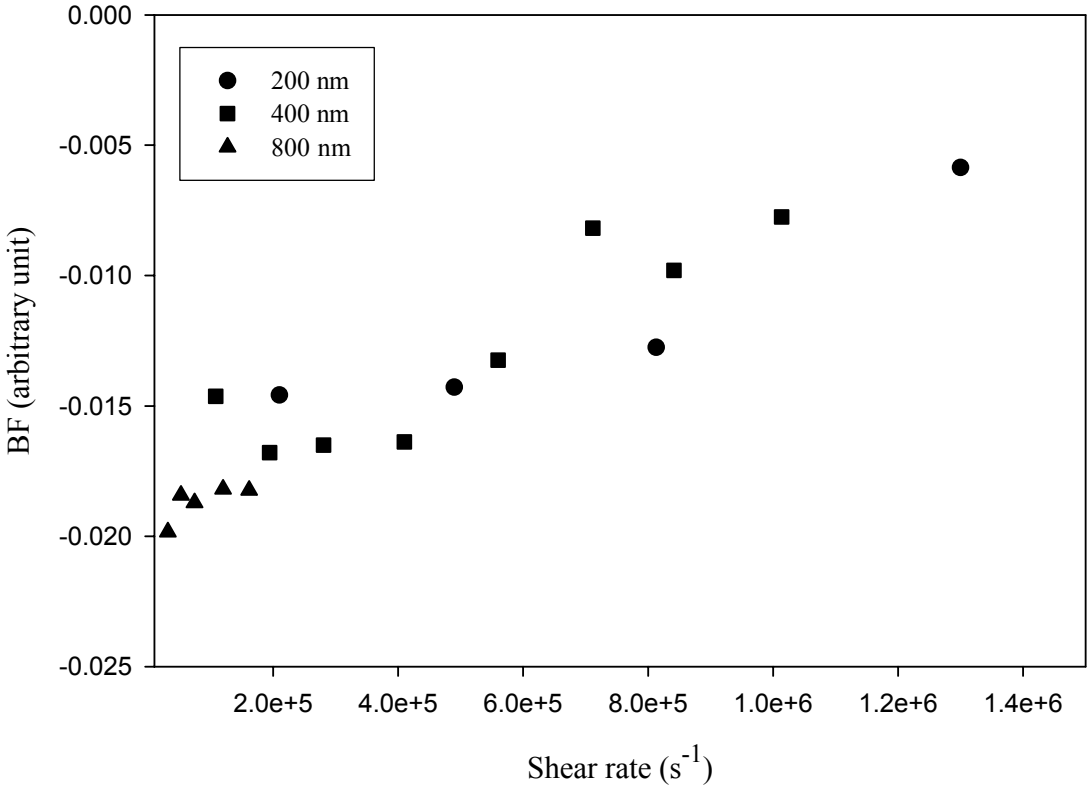


Figure B.1 Birefringence data for different Fomblin YR with shear rate

which mainly appear in the slider since it has smaller surface area. A compensator was used to eliminate such parasitic effects and has been shown to be effective as shown in chapter 5.

When both the slider and disk are brought closer to shear the film between them, a pressure is applied on both to keep the plates close while shearing the film. This pressure may generate birefringence in both optical parts. This background birefringence was constant in all the experiments with different films as long as the same pressure was applied on the plates. The shear effect appears when shear is applied in the non-Newtonian regime to the liquid films as in figure B.1. The agreement of the statistical analysis and the physical argument justify the explanation of the background birefringence, which, therefore, can be subtracted as in the results appearing in figure B.4.

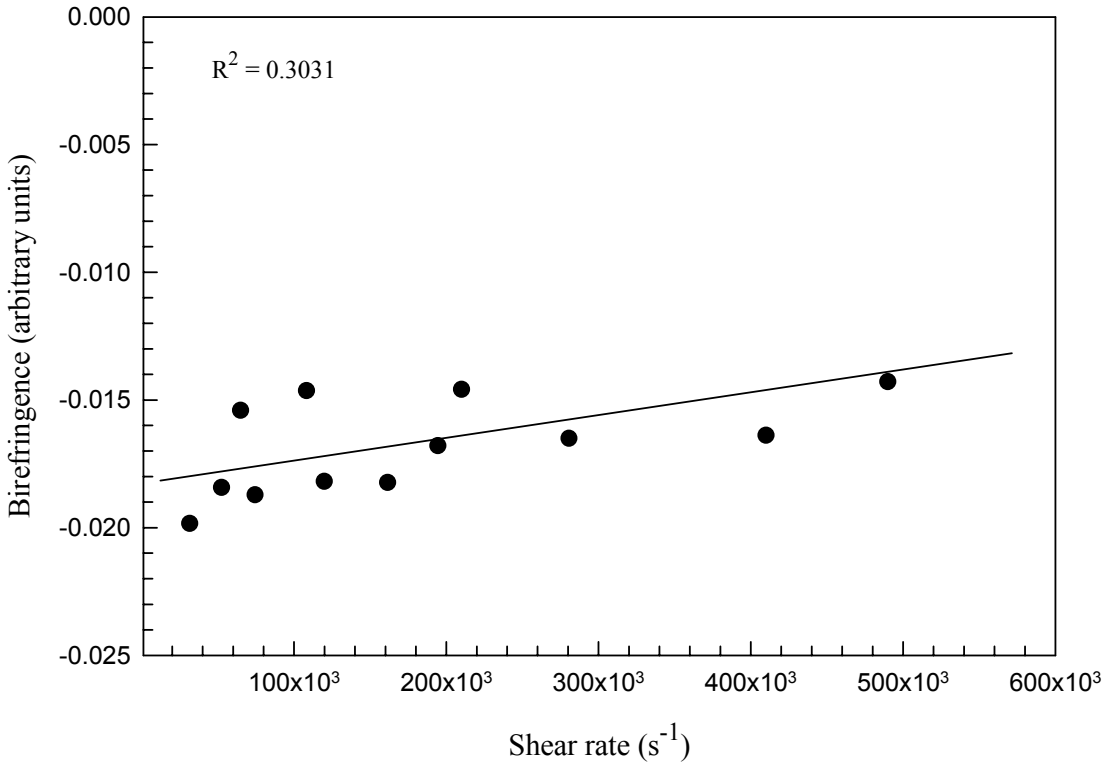


Figure B.2 Best fit line for birefringence data at moderate shear rates

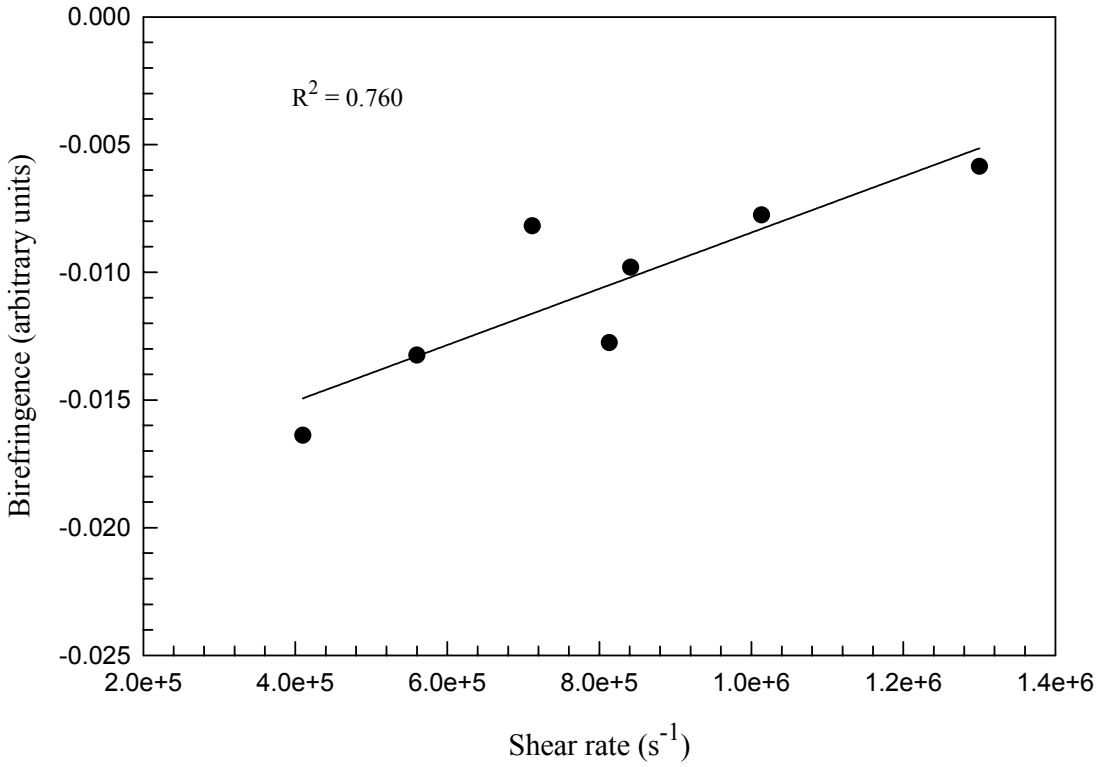


Figure B.3 best fit line for birefringence data at high shear rates

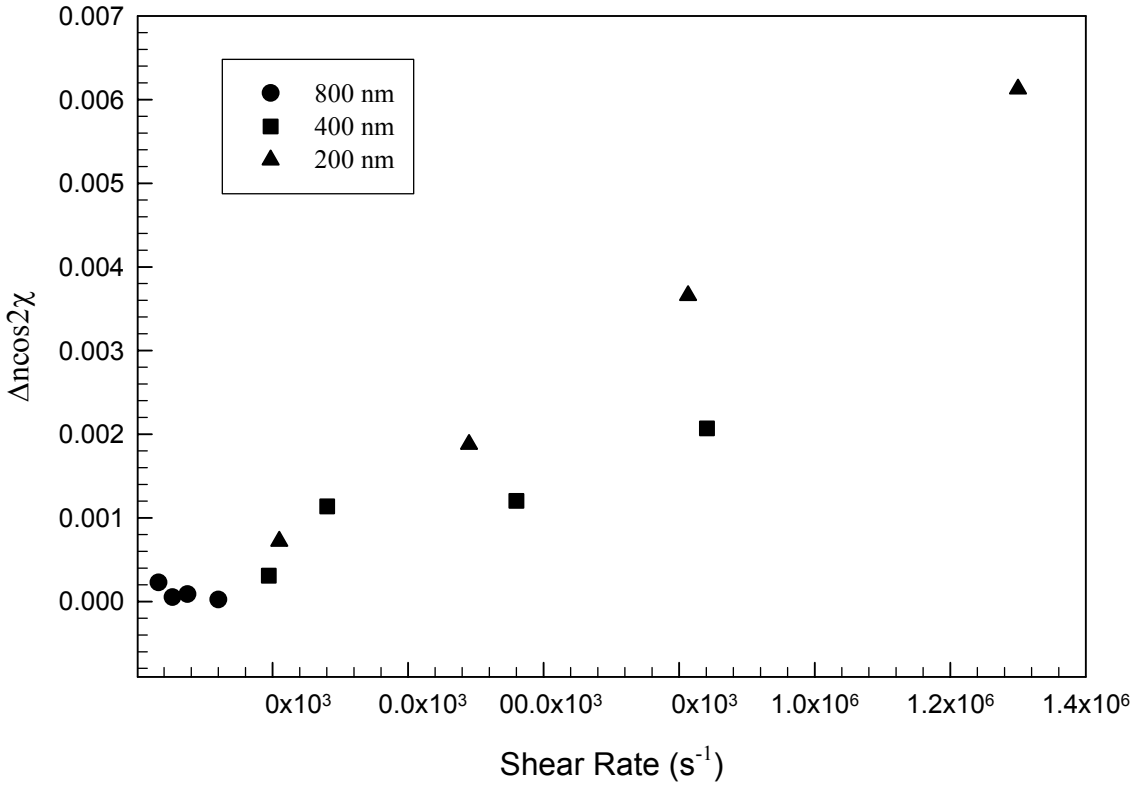


Figure B.4 Birefringence data after background reduction

VITA

Khaled S. Mriziq was born in Zarqa, Jordan for a Palestinian family. He graduated with a bachelor and Master degrees from the University of Jordan. After that, he worked for Jordan University of Science and Technology (JUST) as a teaching and research associate. He then went to Japan where he was on a scholarship from the Japanese government where he worked from 1996 to 1998 at the Institute for Material Research (IMR) of Tohoku University in Sendai. He joined University of Tennessee in Fall of 1998 and received his doctoral degree in Physics in Fall 2003.